Search for the Standard Model Higgs Boson in Missing Transverse Energy and *b*-quark Final States Using Proton-Antiproton Collisions at 1.96 TeV

Tyler McMillan Dorland

A dissertation submitted in partial fulfillment of
the requirements for the degree of

Doctor of Philosophy

University of Washington

2011

Program Authorized to Offer Degree: Physics

University of Washington
Graduate School

This is to certify that I have examined this copy of a doctoral dissertation by

Tyler McMillan Dorland

and have found that it is complete and satisfactory in all respects,
and that any and all revisions required by the final
examining committee have been made.

Chair of the Supervisory Committee:

_____

Anna Goussiou

Reading Committee:

_____

Anna Goussiou

_____

Gordon Watts

_____

Andreas Karch

Date: _____

University of Washington

Abstract

Search for the Standard Model Higgs Boson in
Missing Transverse Energy and b-quark Final States
Using Proton-Antiproton Collisions at 1.96 TeV

Tyler McMillan Dorland

Chair of the Supervisory Committee:
Professor Anna Goussiou
Physics

A search for the standard model Higgs boson is performed in 6.4 fb^{-1} of $p\bar{p}$ collisions at $\sqrt{s} = 1.96$ TeV, collected with the DØ detector during Run II of the Fermilab Tevatron. The final state considered is a pair of jets originating from b quarks and missing transverse energy, as expected from $p\bar{p} \to ZH \to \nu\bar{\nu}b\bar{b}$ production. The search is also sensitive to the $WH \to \ell\nu b\bar{b}$ channel, where the charged lepton is not identified. Boosted decision trees are used to discriminate signal from background. Good agreement is observed between data and expected backgrounds, and a limit is set at 95% C.L. on the section multiplied by branching fraction of $(p\bar{p} \to (Z/W)H) \times (H \to b\bar{b})$. For a Higgs boson mass of 115 GeV, the observed limit is a factor of 3.5 larger than the value expected from the standard model.

TABLE OF CONTENTS

LIST OF FIGURES

Chapter 1

INTRODUCTION

Divide each difficulty into as many parts as is feasible and necessary to resolve it.

Descartes

The expeditions in thought that lead Einstein to unite space and time and Schrodinger to reveal the quantum nature of our universe in the early 20th century gave birth to the field of particle physics. As the safari swelled with numbers it charged the vast undiscovered plains of knowledge in search of new discovery. With each new prize captured, the stores of creation seemed to present a never ending collage of color, flavor, and charge. Then, with cages filled to the brim with discoveries and explorers equally teeming with delight, the cartographers of knowledge set the lay of the the land. Each new discovery was no longer a new phylum or class, but a species, or genus at best. The zoo that existed at the beginning of the 20th century had been reduced just as all colors are made up of one, two, or three. Yet, not to completely disavow their expeditious spirit, the hint of one remaining particle brought back the hunt.

The map of knowledge created in the the latter half of the 20th century came to be known as the Standard Model of particle physics. In the spirit of Mendeleev, and all reductionists, it postulates that all the different particles discovered are made of combinations of fundamental particles. All interactions between these particles are described by fundamental forces, each associated with a particle or particles that act as force carriers. The standard model has prevailed as possibly the most accurate and successful model in all of science. One lone fundamental particle predicted by the standard model still eludes capture, the Higgs boson.

In what follows, a search for the Higgs boson will be detailed, justified, and concluded. In Chapter 2, an in-depth discussion of the constituent ideas of the standard model and the Higgs boson is presented. In Chapters 3 4, the experimental apparatus used in the search is explained. Chapters 6 - 8 presents the search for the Higgs boson including thorough

discussions of control samples used to describe background and techniques of discerning this background from a possible Higgs signal. Finally, chapter 9 presents the results and conclusions from the Higgs search.

Chapter 2

THEORY

The formulation of the scientific method has advanced knowledge in many ways, perhaps most importantly by formalizing the feedback loop between observation and hypothesis, and experiment and theory. Today, entire fields of research are split between one or the other. The theoretical revolution charged forth by Einstein in the early 20th century provided the basis for the experiments that would confirm his place in history decades later. Then new particles were discovered, some with exotic properties, providing the fodder for a new generation of models to describe them. As the number of particles grew, the models adapted and then attempted to predict the next discovery. Through time, though, only Quantum Chromodynamics and the electroweak theory of Glashow, Weinberg and Salam remained robust against experiment and gave a ground work for increasingly accurate predictions. These theories are combined today in the Standard Model which serves as the theoretical framework to describe the interactions of particles through forces.

The Standard Model has made remarkably precise predictions. It is perhaps the most accurate theory created in science, bounded more by analytical tools than axioms. Accuracy, however, does not assure completeness. Take as an example the three known generations of leptons. The familiar electron and its neutrino are accompanied by two similar generations; the muon and its neutrino, and the tau and its neutrino. Fundamentally, the charged leptons only differ in mass. The constituents of protons, the up and down quark, also exist in a similar familial structure with the charm/strange and bottom/top quarks. Further if the cross-section for the process $e^+e^- \rightarrow$ hadrons is measured around the mass of the Z^0 boson, the data agree with the Standard Model prediction for three generations of matter as shown in Figure 2.1. The agreement is incredibly accurate, but there is nothing in the Standard Model that requires or predicts three generations of matter.

The Standard Model allows for a mechanism of electroweak symmetry breaking. In

4
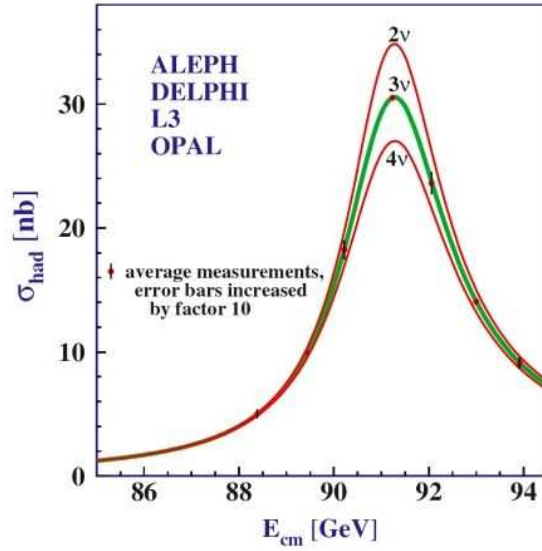
Figure 2.1: The experimental results of the process of $e^+e^- \to$ hadronic final states plotted with the theoretical predictions for 2, 3, and 4 generations of neutrinos [1].

this breaking, through a process called the *Higgs mechanism*, most of the particles are able to attain mass through interactions with the *Higgs boson*. Precise predictions of various quantities of the Higgs boson can be calculated, but they can only be given in terms of a free parameter, the mass of the Higgs boson, for which the Standard model gives no prediction. What follows is a description of the Standard Model and Higgs Mechanism.

2.1   Particles and Forces

The description of the universe at its most fundamental level contains three parts. The particles that make up the describable universe, the forces that act on these particles, and the effect of these forces on the particles.

2.1.1   Fermions

All particles exhibit an intrinsic angular momentum known as *spin*. Spin can not be directly measured, but it's magnitude and one angular component, usually taken as the z component,

can be measured. The spin takes on integer and half-integer values (in dimensions of $\hbar$). Particles that have half-integer values of spin are known as *fermions*. The fundamental fermions make up all matter in the universe, and are so named because they obey the Pauli exclusion principle and Fermi-Dirac statistics. Here fundamental is meant as a particle with no substructure[1].

2.1.2 Bosons

The integer spin states are occupied by *bosons*. They represent the quanta of the force fields and are responsible for mediation of the forces between particles. The Standard Model takes into account three fundamental forces; the strong, weak, and electromagnetic[2] Considering coupling constants to represent the strength of the interaction between fields and particles, general statements can be made about these forces.

The coupling constant associated with electromagnetism, α_{QED} as taken from the theory of Quantum Electrodynamics (QED), is given as

$$\alpha_{QED}(|q^2|) = \alpha_0 \left(1 + \frac{\alpha_0 \ln |q^2|}{3\pi m c^2} \right), \tag{2.1}$$

where q is the momentum transfer (larger $|q^2|$ corresponds to particles closer together), and α_0 is the fine structure constant. With the logarithmic dependence on $|q^2|$, α_{QED} grows as the distance between particles decreases. This gives the familiar effect of the force becoming stronger at closer distances[3]. The electromagnetic force has an infinite range and is propagated by the massless photon.

The coupling constant for the strong force, α_S, is given as:

$$\alpha_S(|q^2|) = \frac{\alpha_s(\mu^2)}{1 + (\alpha_s(\mu^2)/12\pi)(11n - 2f) \ln |q^2|}, \tag{2.2}$$

---

[1] A μ will decay to its first generation counter part, the electron, but is still considered fundamental because there is no known internal structure making this happen.

[2] Gravity is not described by the standard model, which is based on quantum field theory, because there is no complete quantum theory of gravity. It is mediated by the spin 2 graviton.

[3] This effect is known as screening and as the particles near each other they are seeing the "true" charge.

where n is the number of different color charges and f is the number of flavors. The quantity $\alpha_S(|\mu^2|)$ is a reference state that is not the ground state. Qualitatively, there is very little difference in the choice of this state. In the Standard Model, with three color charges and six flavors, $11n > 2f$, leading to two very important effects. First, as $|q^2|$ increases, α_S decreases. This effect, known as asymptotic freedom, allows quarks to behave as free particles as short distances. Conversely, as $|q^2|$ decreases, α_S increases. This effect, known as confinement, results in stronger attractive forces at larger distance, and leads to hadronization.

The last force, the Weak force, is exchanged between leptons and quarks, and is mediated by the charged W bosons and the neutral Z boson. It is the only force mediated by a massive boson and due to the uncertainty principle, is confined to the range of $10^{-18}m$. It is similar to the electromagnetic force in that it weakens with further separation of the particles. Further, it only effects electric and weak charges of particles, and carries no color charge. The charged leptons are expressed in terms of their weak eigenstates. The weak eigenstates of the quarks are a superposition of their strong mass eigenstates, with the mixing given by the Cabbibo-Kobayashi-Maskawa matrix.

Describing three distinct forces is correct phenomenologically, however, it hides a deeper symmetry within the theory. In the 19th century, electrostatic equations existed that entirely described two fields, the electric and magnetic. Maxwell's modification of Ampere's law to include a term generating magnetic fields from moving electric charges betrayed a deeper symmetry. There was an interesting conundrum, namely that these fields should remain the same and charge had to be conserved no matter what velocity an observer was at. Yet the magnetic field should disappear in the rest frame of the particle. With the advent of relativity it was possible to show that in the particle's rest frame the charge density of the surrounding medium actually changed and the magnetic field could be treated as an electric field. Thus the magnetic field is a relativistic transformation of the electric field [2]. This gave rise to the coherent treatment of the two and justified the term electromagnetism.

The electromagnetic field is described by a $U(1)$ field with a photon, γ, as a propagator. The weak force is an $SU(2)$ field and the strong force an $SU(3)$. Thus the group structure of the Standard Model is $SU(3) \times SU(2) \times (U1)$. While no direct analogy to relationship

between electricity and magnetism exists for the other Standard Model fields, there are other unified forces. Take into consideration the weak isospin, I, which is related to electric charge by:

$$Q = I^3 + \frac{1}{2}Y,$$ (2.3)

where Y is the hypercharge. Already, the interdependence of weak isospin hints that there is a connection between the two forces. Indeed, in the Standard model there is a weak isotriplet vector boson, $\mathbf{W}$ and a weak isosinglet, B. These bosons are the combined photon and weak bosons, and expressed in an $SU(2) \times U(1)$ group. However, the $\mathbf{W}$ and B bosons are *massless*. An additional $SU(2) \times U(1)$ field is desired such that as the electroweak breaks to the electromagnetic and weak fields, and their representative bosons attain the desired mass. In the following sections, this field, known as a *Higgs* field is explored.

2.1.3   Gauge Invariance

In describing electroweak symmetry breaking, stating the relativistic lagrangians and some properties of gauge fields is useful. The arguments presented in the remaining portion of this chapter follow those presented in Refs. [3]- [7]. The Euler-Lagrange equation in relativistic field theory reads:

$$\partial_\mu \left(\frac{\partial \mathcal{L}}{\partial(\partial_\mu \phi_i)} \right) = \frac{\partial \mathcal{L}}{\partial \phi_i}.$$ (2.4)

Taking the relativistic energy momentum relation as a guide, some of the important Lagrangians for the different spin fields describing the fermions and bosons can be derived. Using direct replacement of the momentum operators we would suppose a Lagragian of the form

$$\mathcal{L} = \left(\frac{1}{2} \right) (\partial_\mu \phi)(\partial^\mu \phi) - \frac{1}{2} \left(\frac{mc}{\hbar} \right)^2 \phi^2.$$ (2.5)

Applying the Euler-Lagrange equations, gives the Klein-Gordon equation for a spin 0 particle with mass m

$$\partial_\mu \partial^\mu + \left(\frac{mc}{\hbar}\right)^2 = 0. \tag{2.6}$$

If we consider a spinor field ψ and an equivalent lagrangian:

$$\mathcal{L} = i(\hbar c)\bar{\psi}\gamma^\mu \partial_\mu \psi - (mc^2)\bar{\psi}\psi. \tag{2.7}$$

Applying the Euler-Lagrange equations to ψ gives the Dirac equation

$$i\gamma^\mu \partial_\mu \psi - \left(\frac{mc}{\hbar}\right)\psi = 0, \tag{2.8}$$

and applying to $\bar{\psi}$ gives the dirac adjoint.

Lastly, beginning with the lagrangian inspired by electrodynamics,

$$\mathcal{L} = -\frac{1}{16\pi}F^{\mu\nu}F_{\mu\nu} + A^\nu A_\nu, \tag{2.9}$$

yields

$$\partial_\mu + \left(\frac{mc}{\hbar}\right)^2 A^\nu = 0, \tag{2.10}$$

which is equivalent to Maxwell's equations when $m = 0$, and can be treated as a spin 1 or a vector field.

It is easy to show that the Dirac equation is invariant under global phase transformations, that is

$$\psi \rightarrow e^{i\theta}\psi. \tag{2.11}$$

This is known as *global gauge invariance*. However, considering a phase that varies in space-time:

$$\psi \rightarrow e^{i\theta(x)}\psi, \tag{2.12}$$

extra terms arise from the derivative of θ, and *local gauge invariance* is lost. Similarly the vector potential will lose local gauge invariance if:

$$A_\mu(x) \to A_\mu(x) - \partial_\mu\eta(x), \tag{2.13}$$

where local gauge invariance had previously been attained by requiring the mass term to be zero. Additional terms, as described below, must then be added to regain local gauge invariance.

2.1.4 Symmetry Breaking

In perturbative quantum theory, a spectrum is found by finding a minimum and then taking an expansion about the minimum. In the case of field theory, the spectrum about the minimum of the field are the particles belonging to the field, and the minimum is called the *vacuum*. When expressed as a lagrangian, squared terms of the field represent the mass of the particles and quartic terms represent interactions. Motivated by this, consider a Lagrangian of the form:

$$\mathcal{L} = \frac{1}{2}\partial_\mu\phi\partial^\mu\phi - \left(\frac{1}{2}\mu^2\phi^2 + \frac{1}{4}\lambda\phi^4\right), \tag{2.14}$$

where μ and λ are constants to be measured. While not specifically prohibited, ϕ^3 terms can reasonably be excluded taking into account the desire for rotational symmetry[4]. We can reasonably exclude the ϕ^3 term with rotational symmetry arguments.

For $\mu^2 > 0$, the vacuum is trivially minimized at zero (or at least can be transformed to a minimum at zero), and μ^2 is equivalent to (mass)^2. Much more interesting is the case of $\mu^2 < 0$, where the minimum is

$$\phi(\mu^2 + \lambda\phi^2) = 0, \tag{2.15}$$

corresponding to a vacuum at $v = \pm\sqrt{\frac{-\mu^2}{\lambda}}$. The spectrum, given by expanding about the vacuum, is then,

$$\phi(x) = v + \eta(x), \tag{2.16}$$

---

[4]Terms higher than ϕ^4 result in a Lagrangian that is not renormalizable.

ending with

$$\mathcal{L} = \frac{1}{2}\partial_\mu\eta\partial^\mu\eta - \left(\lambda v^2\eta^2 + \lambda v\eta^3 + \frac{1}{4}\lambda\eta^4\right) + c, \qquad (2.17)$$

which gives mass terms $m_\eta^2 = -2\mu^2$. The initial conjecture that $\phi \to -\phi$ is no longer valid due to the η^3 term. Descriptions of the theory were desired to be equivalent whether being described by η or ϕ. Due to the choice of the vacuum ($+\phi$ instead of $-\phi$) the symmetry of the original lagrangian is not maintained, and the solutions do not have the same symmetry. This choice of vacuum ($+\phi$) created *spontaneous symmetry breaking*.

Extending the argument to include complex scalar fields $\phi = (\phi_1 + i\phi_2)$ and modifying the lagrangian accordingly gives

$$\mathcal{L} = \frac{1}{2}(\partial_\mu\phi) * (\partial^\mu\phi) - \mu^2\phi^*\phi - \lambda(\phi^*\phi)^2 \qquad (2.18)$$

and a minimum of the potential is found at

$$\phi_1^2 + \phi_2^2 = \frac{-\mu^2}{\lambda} = v^2. \qquad (2.19)$$

To expand about the potential, a choice must be made on the ϕ-circle, necessarily breaking the symmetry. Choosing $\phi_1 = v$ and $\phi_2 = 0$, and expanding about the imaginary field

$$\phi = \frac{v + \eta(x) + i\rho(x)}{\sqrt{2}}, \qquad (2.20)$$

gives the lagrangian

$$\mathcal{L} = \frac{1}{2}(\partial_\mu\rho)^2\frac{1}{2}(\partial^\mu\eta)^2 + \mu^2\eta^2 - \lambda v(\eta\rho^2 + \eta^3) - \frac{\lambda}{2}\eta^2\rho^2 - \frac{\lambda}{4}\eta^4 - \frac{\lambda}{4}\rho^4. \qquad (2.21)$$

Again, a term μ^2 describes the mass of the η field. However, no like term arises for the ρ field, and it is assumed to be massless. A general theorem exists that whenever a continuous global symmetry is spontaneously broken, the spectrum will contain a massless spin-zero boson. The choice of the vacuum broke the U(1) symmetry, and we thus expect one massless boson. This ρ particle, representing this massless particle, is known as a goldstone boson.

2.1.5 Abelian Higgs Mechanism

In order to maintain local gauge invariance a massless vector field A_μ is introduced, and the Lagrangian is written in terms of the covariant derivative

$$\mathcal{D} = \partial_\mu - igA_\mu, \tag{2.22}$$

giving

$$\mathcal{L} = (\mathcal{D}_\mu \phi)^* (\mathcal{D}^\mu \phi) - \frac{1}{4} F_{\mu\nu} F^{\mu\nu} - \mu^2 \phi^* \phi - \lambda (\phi^* \phi)^2. \tag{2.23}$$

Proceeding as before but now calling the introduced field the Higgs field and writing the expansion about the minima as

$$\phi(x) = \frac{(v + h(x))}{\sqrt{2}}, \tag{2.24}$$

yields

$$\mathcal{L} = \frac{1}{2}\partial_\mu h \partial^\mu h + \frac{1}{2} g^2 v^2 A_\mu A^\mu - \lambda v^2 h^2 - \lambda v h^3 - \frac{\lambda}{4} h^4 + g^2 v h A^\mu A_\mu + \frac{1}{2} g^2 h^2 A_\mu A^\mu. \tag{2.25}$$

Here, the gauge boson, the so-called Higgs boson, has acquired a mass term, which was not expected due to the previous theorem. There are now three massive gauge fields and a single massive Higgs boson. Previously, the ρ expansion led to terms such as $\partial_\mu \rho A_\mu$. If read as an interaction, it is a direct transformation of the ρ particle into A_μ. However, local gauge invariance allows for the choice of a gauge such that this term disappears. In doing so, the gauge field acquires an extra degree of freedom, and mass. When the gauge "eats" the Goldstone boson it is known as the *Higgs mechanism.*

2.1.6 Higgs Mechanism in the Standard Model

For the Standard Model, a further degree of complexity is required to satisfy the previous desire to have a field complementary to the electroweak field. Thus an $SU(2) \times U(1)$ doublet is used

$$\phi = \begin{pmatrix} \phi^+ \\ \phi^0 \end{pmatrix}, \tag{2.26}$$

with

$$\phi^+ = \frac{\phi_1 + i\phi_2}{\sqrt{2}} \tag{2.27}$$

$$\phi^0 = \frac{\phi_3 + i\phi_4}{\sqrt{2}}. \tag{2.28}$$

Now the lagrangian is

$$\mathcal{L} = (\partial_\mu \phi)^\dagger (\partial^\mu \phi) - \mu^2 \phi^\dagger \phi - \lambda (\phi^\dagger \phi)^2, \tag{2.29}$$

and studying the potential $V(\phi) = \mu^2 \phi^\dagger \phi + \lambda (\phi^\dagger \phi)^2$ with a minimum at $v^2/2 = -\mu^2/2\lambda$, the vacuum is at

$$\phi_0 = \frac{1}{\sqrt{2}} \begin{pmatrix} 0 \\ v \end{pmatrix}, \tag{2.30}$$

and the expansion is about

$$\phi(x) = \frac{1}{\sqrt{2}} \begin{pmatrix} 0 \\ v + H(x) \end{pmatrix}, \tag{2.31}$$

where the real part of $\phi^\dagger \phi$ is

$$\phi_1^2 + \phi_2^2 + \phi_3^2 + \phi_4^2 = \text{constant.} \tag{2.32}$$

As before, the choice of minimum is at $\phi_3 = v, \phi_1 = \phi_2 = \phi_4 = 0$. Doing so breaks three gauge symmetries by choosing the direction in ϕ. The contribution of the SU(2) scalar doublet to the lagrangian is

$$\mathcal{L}_s = (D^\mu \Phi)^\dagger (D_\mu \Phi) - V(\Phi). \tag{2.33}$$

Using an isospin argument to rewrite the covariant derivative as

$$\mathcal{D} = \partial_\mu - ig_1\frac{Y}{2}B_\mu - ig_2\frac{\vec{\tau}}{2}\vec{W}_\mu, \tag{2.34}$$

the choice of field makes Y equal to unity and the following transformations can be written:

$$W^+ = (-W^1 + iW^2)/\sqrt{2}$$
$$W^- = (-W^1 - iW^2)/\sqrt{2}$$
$$W^0 = W^3, \tag{2.35}$$

which allows for terms such as

$$\left(\frac{1}{2}vg_2\right)^2 W_\mu^+ W^{-\mu} + \frac{1}{8}v^2(g_1 B_\mu - g_2 W_\mu^3)^2. \tag{2.36}$$

The first term is exactly what is expected for the charged weak bosons, and thus the W bosons have gained a mass term $M_W = vg_2/2$!

Further, defining orthogonal terms

$$A_\mu \propto g_2 B_\mu - g_1 W_\mu^0, \tag{2.37}$$

and

$$Z_\mu \propto g_1 B_\mu - g_2 W_\mu^0, \tag{2.38}$$

and collecting terms allows for $(\frac{1}{8}v(g_1^2 + g_2^2)Z_\mu Z^\mu$ which is expected term for $Z_\mu Z^\mu$, and there is no term for $A^\mu A_\mu$. Thus the Z term with the neutral current and the A term, as expected. Specifically:

$$M_Z = \frac{1}{2}v\sqrt{g_1^2 + g_2^2}, \tag{2.39}$$

and

$$M_\gamma = 0. \tag{2.40}$$

Through this process, the weak bosons have attained mass and the photon remained massless. The goal of finding an appropriate field that gives rise to boson mass terms as electroweak symmetry breaks has been accomplished. To include Fermions, first consider the electron and neutrino with right and left handed projections given by

$$\psi_{L,R} = \frac{1}{2}(1 \mp \gamma_5)\psi. \tag{2.41}$$

Taking as a fact that weak interactions only couple to the left-handed fermions, the doublet can be written as

$$L_L = \begin{pmatrix} \nu_L \\ e_L \end{pmatrix}, \tag{2.42}$$

and expect mass terms such as

$$\mathcal{L} = -m\bar{\psi}\psi = -m(\bar{\psi}_L\psi_R + \bar{\psi}_R\psi_L). \tag{2.43}$$

Taking the gauge invariant Yukawa coupling of the Higgs to the up and down quark gives

$$\mathcal{L}_d = -\lambda_d \bar{Q}_L \Phi d_R + h.c., \tag{2.44}$$

and using the Higgs mechanism as before gives

$$-\lambda_d \frac{1}{\sqrt{2}} (\bar{u}_L, \bar{d}_L) \begin{pmatrix} 0 \\ v + h \end{pmatrix} + h.c. \tag{2.45}$$

$$-\lambda_d \sqrt{2}(v + h)(\bar{d}_L d_R + \bar{d}_R d_L). \tag{2.46}$$

Making the identity $\lambda_d \sqrt{2} v = m + d$, and using the fact that $\psi_c = -i\tau_2 \psi^* \rightarrow \phi_c = (-\phi^{0*}\phi^-)$ creates an SU(2) doublet, there is an analogous term for the up quark

$$\mathcal{L}_{int} = m_d d\bar{d} + m_u u\bar{u} + m_d/v\bar{d}dH + m_u/vu\bar{u}H, \tag{2.47}$$

and thus the quarks have been given mass in the first two term. The last are interaction terms with the Higgs.

2.1.7 Cross-section and Branching ratios

One distinguishing feature of the Higgs mechanism is that all couplings are in terms of constants and the mass. The initial potential had two free parameters which can be stated:

$$v^2 = -\frac{\mu^2}{2\lambda}$$
$$m_H^2 = 2v^2\lambda, \tag{2.48}$$

giving the Higgs mass in terms of the vacuum, which can be measured, and an unknown coupling. This can be used to show that the Higgs production and decay processes can be calculated unambiguously in terms of the Higgs mass. Figures 2.2 and 2.3 show the cross-sections predicted at the Tevatron. The relevance of these plots will be further discussed when motivating the methodology for the search of the Higgs boson in Chapter 6.
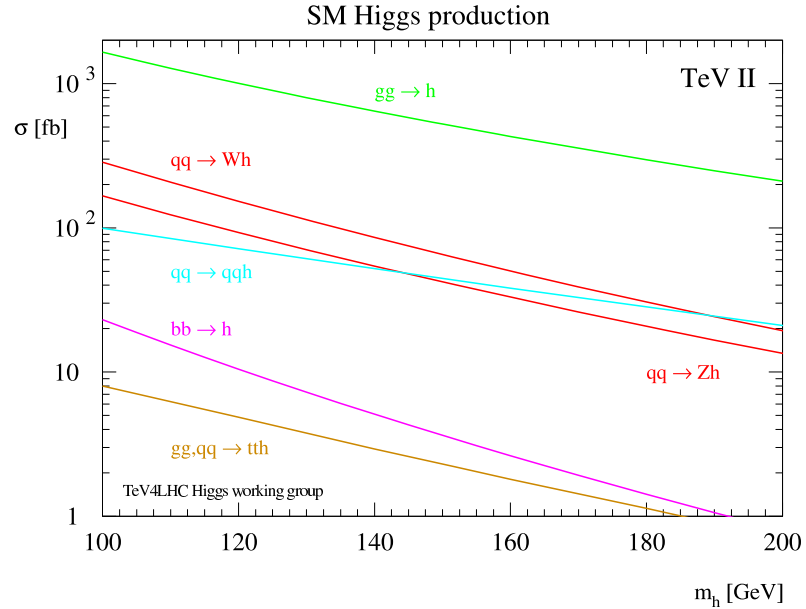
Figure 2.2: Production Cross-sections at the Tevatron for the Higgs boson
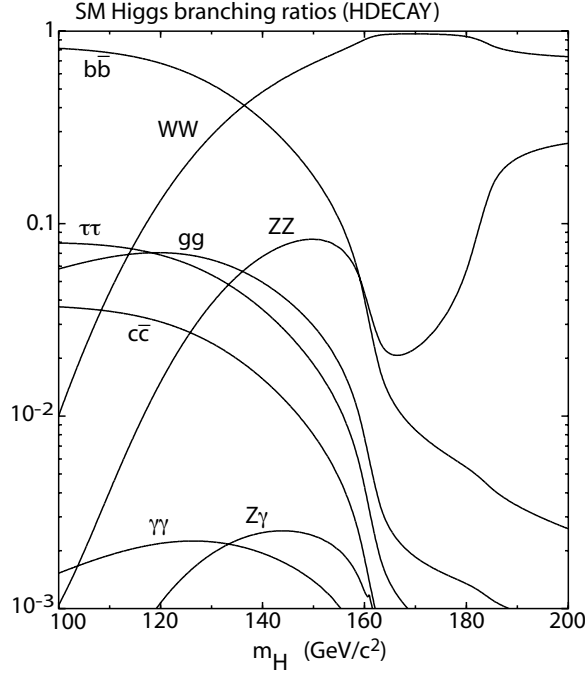
Figure 2.3: Higgs Branching Ratios [8]

2.2 Limits on the Higgs mass

2.2.1 Triviality

The Higgs mass is not directly given, but limits can be placed on the Higgs boson mass both directly and indirectly. The direct method will be discussed in the results of this search, but one indirect limit can be deduced by considering the quartic coupling, λ, which changes with the effective scale Q (usually taken as v in the standard model) due to self-interactions of the scalar field as

$$\frac{d\lambda}{dt} = \frac{3\lambda^2}{4\pi^2},\tag{2.49}$$

where $t = log(Q^2/Q_0^2)$. Solving yields:

$$\lambda(Q) = \frac{\lambda Q_0}{\left[1 - \frac{3\lambda(Q_0)}{4\pi^2 log(\frac{Q^2}{Q_0^2})}\right]}. \tag{2.50}$$

As $Q \to \infty$ then $\lambda(Q_0)$ goes to zero. Thus, all self-interacting terms vanish and the theory involves no interactions at low energy. This is known as a *trivial* theory. Rewriting in terms of v and taking the coupling to be finite and positive, as is expected of interactions in the theory, and stating $1/\lambda(\Lambda) > 0$, a limit can be derived. Here, Λ is the scale at which new physics enters, giving the approximate upper limit

$$M_h^2 < \frac{8\pi^2 v^2}{3log(\Lambda^2/v^2)}. \tag{2.51}$$

2.2.2   Radiative corrections

The relationship between the electromagnetic and weak couplings is given by

$$G_F = \frac{\pi\alpha}{\sqrt{2}\; m_W^2 \sin^2\theta_W}. \tag{2.52}$$

In the Standard Model,

$$\cos^2 = \frac{m_W^2}{m_Z^2}. \tag{2.53}$$

At the Z-pole, the presence of radiative corrections is given by

$$\cos^2\theta_W \sin^2\theta_W = \frac{\pi\alpha}{\sqrt{2}m_Z^2 G_F}\frac{1}{1-\delta R}. \tag{2.54}$$

The ΔR term is usually divided into two parts:

$$\Delta R = \Delta\alpha + \Delta R_W, \tag{2.55}$$

where $\Delta\alpha$ arises in effects from fermion loops in the EM propagator. The term ΔR_W contains corrections due to the propagator self-energies. These terms are dependent on m_t^2 and $\ln(m_h)$. This relationship between the Higgs, t, and W masses allows for a calculation of the Higgs mass that is only constrained by the accuracy with which the W and t quark masses are known as shown in Figure 2.4.
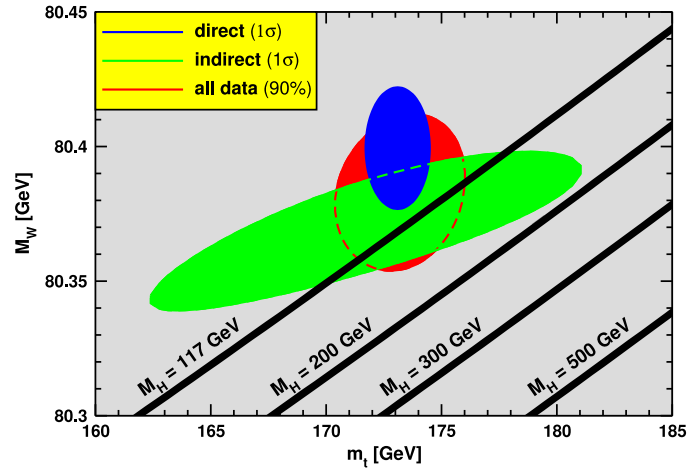
Figure 2.4: One standard deviation region in M_W as a function of M_t for the direct and indirect limitations on the Higgs mass. Also included is the 90% CL region for all data. The SM prediction as a function of M_H is also indicated [9].

Chapter 3

THE FERMILAB ACCELERATOR CHAIN

3.1 Acceleration

The indirect limits set by the standard model have sshown that the Higgs boson will lie approximately between 100 to 200 times the mass of the heaviest stable baryon, the proton. Therefore, the relativistic mass-momentum relation $E^2 - p^2 = m^2$ must be exploited to create an interaction between two particles with sufficient center-of-mass energy to create environment a Higgs boson. Even in such an environment with requisite energy, it will be created very rarely. An experiment must be designed that is both capable of creating the high energy environment, and producing it rapidly.

The desired high-energy interaction will be created using particle-antiparticle annihilation (or boson fusion, if appropriate). Considering only particles stable in a low-energy environment, only two candidate particles are available, the electron and proton. The electron has the advantage of being a single particle allowing an unambiguous initial state. This means it is best used for precision studies, where measurements can be made that are sensitive to higher order effects. The proton, with a mass of 2000 m_e, is suited for exploring new energy regimes, even though the proton momentum is distributed within it's constituent quarks and gluons. Further, the energy lost due to synchrotron radiation goes as $\Delta E \propto \left(\frac{E}{m} \right)^4$. The choice of a proton also makes a circular accelerator the preferential design.

In an ideal scenario, a relativistic particle that collides with a particle at rest will create an energy in the center-of-mass frame $(\sqrt{s})$ proportional to the square root of energy of the relativistic particle. However, when two relativistic particles of equal and opposite momentum collide they will create an energy directly proportional to the energy of each particle. It is then advantageous to collide beams of particles as opposed to scatter off a fixed target. Finally, the gluon fraction of the energy in the proton's parton distribution

changes as the proton becomes more energetic. At energies of approximately 1 TeV, the quarks will constitute the majority of the momentum fraction, with gluons being a less significant portion of the proton. Accordingly, the quark-antiquark cross-section is larger than the gluon fusion cross-section, and the choice is made for the antiproton as the second particle.

From the Lorentz Force:

$$\vec{F} = q\vec{E} + q(\vec{v} \times \vec{B}) \tag{3.1}$$

only an Electric field will provide acceleration in the direction of velocity. Creating an electric field, as in between the plates of a capacitor, will accelerate a charged particle. Or as in section 3.1.1 an alternating current can be used to successively charge capacitors through diodes with and create a linear acceleration. For initial stages of acceleration this method will be appropriate, but a more sophisticated approach will be able to not only accelerate particles, but allow manipulation of many particles grouped together. First, consider a rectangular waveguide that is a perfect conductor at the boundaries. From Maxwell's equation we have the wave equations:

$$\nabla^2 E = \frac{1}{c^2}\frac{\partial^2 E}{\partial t^2} \quad \text{and} \quad \nabla^2 B = \frac{1}{c^2}\frac{\partial^2 B}{\partial t^2} \tag{3.2}$$

We take the waveguide to be open-ended in the longitudinal z-direction with lengths a and b in the $x-$ and $y-$ directions, respectively. We then write the general form of the longitudinal solution to the wave equations considering the boundary equations:

$$E_z = E_0 \sin\frac{l\pi x}{a} \sin\frac{m\pi y}{b} e^{i(k_g z - \omega t)} \tag{3.3}$$

where l and m are integers defining the modes of the x and y planes. This satisfies the boundary conditions if

$$\frac{l^2}{a^2} + \frac{m^2}{b^2} = \frac{k_0^2 - k_g^2}{\pi^2} \tag{3.4}$$

with $\lambda_g = \frac{2\pi}{k_g}$ and $\lambda_0 = \frac{2\pi}{k_0}$. These solutions can be used to accelerate particles in the z direction. Further, if

$$\left(\frac{l}{2a}\right)^2 + \left(\frac{m}{2b}\right)^2 = \frac{1}{\lambda_0^2} \tag{3.5}$$

the wavelength, λ_g, becomes infinite, allowing a choice of a and b such that only one mode propagates in z. This effect is extraordinarily useful when considering groups of particles that are approximately in phase with the electric field. Particles slightly ahead of the field will receive less acceleration, while particles slightly behind the field will receive more, creating a grouping of particles in phase with the acceleration of the beam.

With these mechanisms, a group of particles can be uniformly accelerated to a desired energy. This accomplishes the first task of creating an environment such that a Higgs particle can be created. Still, we know that even in optimal circumstances, Higgs production is exceedingly rare. Thus we need to create the environment as frequently as possible. To collide a single proton with a single antiproton with any appreciable frequency is effectively impossible. Instead, groups of protons and anti-protons, called bunches, are directed into each other to significantly increase the odds a collision will occur. Further manipulation of these bunches will significantly increase the frequency of these collisions. If the cross-sectional area of the bunches is decreased more collisions will occur. Also, simply increasing the number of times the bunches are sent into each other will increase the likliehood of a collision. A measure of the number of collisions obtained can be taken as the luminosity, and a primative definition is given here, and discuss in depth later:

$$L = \frac{f N_p N_{\bar{p}}}{A} \tag{3.6}$$

Here, L stands for luminosity. It is maximized by increasing the frequency of the bunch crossings, f, the number of particles, N, in each bunch, and by minimizing the bunch cross-section, A. Optimization of the first two criteria is straightforward, however, minimizing beam a deserves a more thorough treatment.

From the Lorentz force, if the direction of acceleration is in the z-direction, then the magnetic field will effect motion in the lateral plane, which is also the plane of the cross-sectional area to be minimized. Thus we can make use of the magnets to increase luminosity by showing that the magnets can be used as lenses that focus charged particles. To begin,

we assume that motion in the x and y planes are decoupled. We can describe the motion of a particle by using the transfer matrix, $\mathbf{M}$, given in a drift region of length z in free space by:

$$\begin{pmatrix} x \\ x' \end{pmatrix}_z = \mathbf{M} \begin{pmatrix} x \\ x' \end{pmatrix}_0 = \begin{pmatrix} 1 & z \\ 0 & 1 \end{pmatrix} \begin{pmatrix} x \\ x' \end{pmatrix}_0 \tag{3.7}$$

For a lens, an off-axis ray parallel to the lens is focused at point f if:

$$\begin{pmatrix} x \\ x' \end{pmatrix} = \begin{pmatrix} 1 \\ 0 \end{pmatrix} \rightarrow \begin{pmatrix} 1 \\ -1/f \end{pmatrix} \tag{3.8}$$

Combining these we can construct the convergent transfer matrix, and by inverting the derivative of motion, we can create the divergent counterpart:

$$\mathbf{M}_{convergent} = \begin{pmatrix} 1 & 0 \\ -1/f & 1 \end{pmatrix} \quad \text{and} \quad \mathbf{M}_{divergent} = \begin{pmatrix} 1 & 0 \\ 1/f & 1 \end{pmatrix} \tag{3.9}$$

Consider a particle with some initial velocity in the x and z directions and beginning at the origin. if the particle goes through a drift region a and then a convergent focusing region f followed by another drift region, the transfer matrix will be:

$$\begin{pmatrix} 1 - \frac{a}{f} & 2a - \frac{a^2}{f} \\ \frac{-1}{f} & 1 - \frac{a}{f} \end{pmatrix} \tag{3.10}$$

the x -component of the Lorentz force is:

$$m\frac{d^2x}{dt^2} = q(\vec{v} \times \vec{B})_x = -\frac{ep}{mbx}$$

which is a simple harmonic oscillator:

$$\frac{d^2x}{dt^2} = -k^2x$$

with a general solution:

$$x = A\cos kz + B\sin kz$$

Now consider a quadrapole field of length l, the motion in the x plane of a charged particle:

$$\mathbf{M}_x = \begin{pmatrix} \cos kl & 1/k \sin kl \\ -k \sin kl & \cos kl \end{pmatrix} \tag{3.11}$$

Which can be shown to be a focusing lens with

$$f = \frac{1}{k \sin kl} \quad \text{and} \quad a = \frac{1}{k} \tan \frac{kl}{2}$$

Similarly in the y direction, it is shown to be a divergent lens with

$$f = \frac{1}{k \sinh kl} \quad \text{and} \quad a = \frac{1}{k} \tanh \frac{kl}{2}$$

So a single quadrapole magnet will focus in one plane while defocusing in the other. However, if we consider the limit $kl \ll 1$ and $p \gg ebl^2$ then f and a are the same in the previous equations. If we then put two quadrapole in series but with alternating poles we have:

$$\begin{pmatrix} 1 & 0 \\ \frac{1}{f} & 1 \end{pmatrix} \begin{pmatrix} 1 & a \\ 0 & 1 \end{pmatrix} \begin{pmatrix} 1 & 0 \\ -\frac{1}{f} & 1 \end{pmatrix} \tag{3.12}$$

Which is equivalent to:

$$\begin{pmatrix} 1 & f \\ 0 & 1 \end{pmatrix} \begin{pmatrix} 1 & 0 \\ -\frac{a}{f^2} & 1 \end{pmatrix} \begin{pmatrix} 1 & -f \\ 0 & 1 \end{pmatrix} \tag{3.13}$$

Which is a convergent lens with focal length $\frac{a}{f^2}$ followed by two drift distances of length f. Thus we can use magnets to focus our beam and maximize luminosity [10].

3.1.1 Preacceleration

The acceleration journey begins quite inconspicuously as the output from a simple pressurized hydrogen gas tank mounted on a wall. These initial neutral H_2 molecules are introduced into a direct-extraction magnetron, shown in Figure 3.1, that is only a few inches long. A 1kG field is introduced via an external magnet and a 40A arc is made between the electrodes. This ionizes the gas, forming a dense plasma of H^+ ions and electrons from the arc. Some of the H^+ ions will pick up two electrons and quickly be repelled from the cathode.
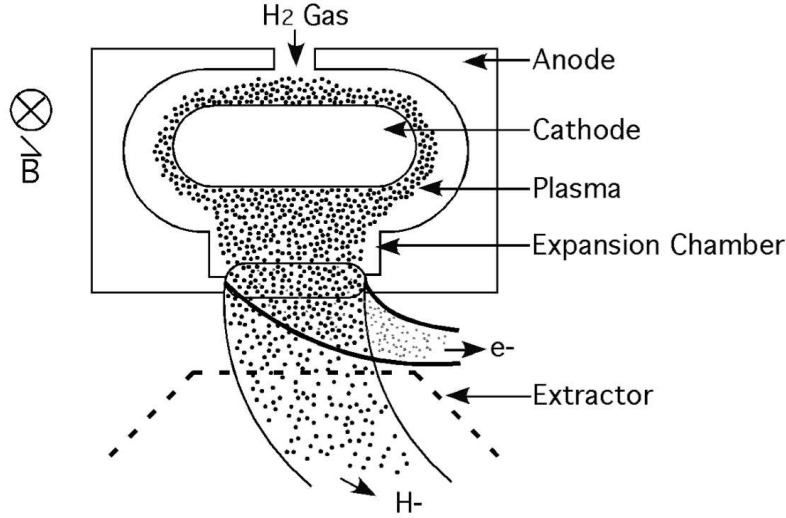
Figure 3.1: Diagram of the H^- Source

An electrostatic extractor is pulsed to 18kV, allowing pulses of the negative ion beam to escape. The external magnetic field separates H^- ions from the electrons, and these pulses form an H^- beam [11].

From the H^- source the beam enters the first accelerator in the chain. It is a 5-stage voltage multiplier based on the Cockroft Walton design. A simple schematic of the electrical multiplication is shown in Figure 3.2. The actual accelerator, named the Haefley, uses a 75 kV AC transformer that drives the multiplier. With two multipliers with five stages each adding $-2V_0$ a piece, there is a total of -750 kV. Thus the ions gain an energy of 750keV in the initial stage of acceleration.

3.1.2 Linear Acceleration

After preacceleration the ions enter two stages of linear accelerators (linacs). This is the first accelerator to use the ideas presented in the introduction to this chapter. The beam will first increase in energy from 750 KeV to 116 MeV then to 400 MeV. The first accelerator stage is a series of 5 cylindrical radio frequency accelerating cavities making up the Drift Tube Linac (DTL). The second stage is a seven-section device named of the Side Coupled

to
load

F -4V$_0$

E
-3V$_0$ + V$_0$ sin wt

-2V$_0$
DC Capacitor

-2V$_0$
Coupling
Capacitor

D -2V$_0$

C
-V$_0$ + V$_0$ sin wt

-2V$_0$
DC Capacitor

-V$_0$
Coupling
Capacitor

B

A

V$_0$ sin wt
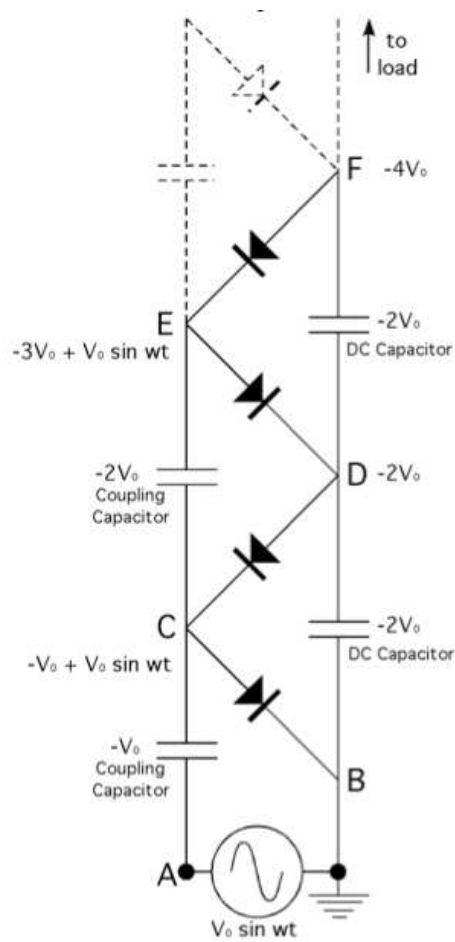
Figure 2.1
Diode Voltage Multiplier

Figure 3.2: Electronic layout for the diode multiplier

Linac (SCL).

To avoid the technical difficulties arising from the fact that, as particles approach the speed of light, any type of alternating field used to generate acceleration as in the previous section will quickly reach microwave frequencies and beyond, waveguide tubes are designed such that the length of the tube allows the particles to be shielded inside the cavity during the deceleration phase of an electrical field oscillating at radio frequency. This design leads to the name drift tube accelerator. In the accelerating phase of the field the particles are

between cavities and will feel the accelerating force. As seen in Figure 3.3, this requires longer and longer drift tubes. The entire length of the DTL is 73 meters. (7.5 MeV/m)
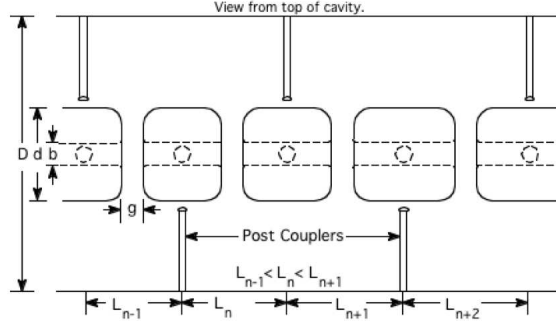
Figure 3.3: The Drift Tube Linac (DTL)

The second stage of the linac, the SCL, eliminates the need for drift tubes by having a series of resonant cavities coupled to the energy of each cavity. This is accomplished by designing each cavity to be $\frac{\pi}{2}$ ahead in phase of the electric field of the previous cavity. This phase separation eliminates the need to shield a particle from a decelerating field allowing for at least twice the acceleration of the DTL. However, each cavity must still be made to be longer and longer as particles are still gaining significant velocity and not just gaining energy from relativistic effects. The SCL is only 63m but provides nearly three times the acceleration of the DTL.

3.1.3 Booster

The particles leave the linear accelerators at an energy of 400 MeV. They now enter the third type of accelerator and first circular accelerator, or synchrotron. The Booster accelerator is a 74.47 meter radius synchrotron that will accelerate the particles to 8 GeV. While a linear accelerator relies on high gradient cavities to provide a one time acceleration for particles, the circular design of a synchrotron allows for a single field to accelerate a particle many times. The curvature of the beam is accomplished by passing ions through a dipole magnet that arcs the trajectory, so the accelerator is better described by a cyclic polygon than

a true circle. The Booster and subsequent synchrotrons will all have the basic design of a series of dipole magnets for bending between quadrapole pairs separated by a focusing length. The Booster relies on 96 magnets to bend the path of the particles. As the particles gain more and more energy, the field inside the bending magnets must also increase to keep a constant radius. The particles then leave this accelerator with an energy of 8 GeV. After acceleration, the speed of the protons has increased so that there are 84 cycles per proton orbital period, resulting in 84 naturally formed bunches. At this point the particles are within 1% of the speed of light and thus increases in velocity are essntially neglected in accelerator design, as further energy gains will be from relativistic effects.

3.1.4   Main Injector

The Main Injector is another synchrotron, but unlike the preceding accelerators has many more functions than the acceleration of H^- ions. The ions enter the main injector with an energy of 8 GeV, and can be used for many purposes.

As we saw in equation 3.6, we must maximize the bunch collision frequency and the number of particles in a bunch, and these are largely limited by machine considerations. Properly forming the bunches is done in this stage of acceleration, as well as the creation of the anti-protons. In order to create anti-protons, the main injector will send H^- ions to an anti-proton source, a dense material target. After their creation, they will be accelerated to the same energy as the ions and then may be sent to storage, or directly to the next stage of acceleration. At all times after creation, the anti-protons go through "cooling", processes that reduce longitudinal and lateral deviations.

Once sufficiently spaced and populated beams of protons and anti-protons have been produced, the beams are accelerated to 150 GeV. At this point, they are transfered in groups of bunches to the Tevatron. The beams inside the Tevatron consist of 36 bunches arranged in 3 superbunches of 12 with approximately 3×10^{11} protons, and 7×10^{10} anti-protons per bunch.

Recycler

The Recycler is housed in the same ring as the Main Injector. However, it's purpose is not acceleration. Instead the Recycler is used to store the anti-protons that are being made while the Tevatron is colliding beams. For this storage role, the Recycler does not need to have powered magnets and instead has permanent magnets that play the same role as the main injector bending magnets with no acceleration. Inside the recycler the beam can be stored for many hours. During this time the beam is cooled to reduce longitudinal and transverse spread in the beam.

Anti-Proton Source

The method of producing anti-protons is to send a beam of protons into a dense target and recover to anti-protons created. The anti-protons will obviously come out with a significantly less amount of kinetic energy. When the main injector readies for anti-proton production it extracts all 84 bunches from the Booster, and does this twice for a more intense beam to send directly to the anti-proton source. Taking into consideration that other experiments need this beam from the Main Injector, bunches are fired at the proton source approximately every two seconds.

In order to create large numbers of anti-protons, an even larger number of protons must be slammed into a sufficiently dense target such that pair creation can occur at a sufficiently high rate. Approximately 1 anti-proton is created for every 1,000,000 protons on target. After the bunch hits the target the resulting spray of anti-protons is sent through a lithium lens. The lens is a lithium cylinder with a hole bored through the center. It has a current passed through it creating an intense magnetic field that serves to reduce the longitudinal spray of the anti-protons.

Debuncher

The spray of anti-protons from the anti-proton source are understandably of very low quality, with a spread approximately equal to that of the aperature of the lithium lens. The primary purpose of the debuncher is to cool the beam and reduce its transverse spread. In doing

so, any residual bunch nature of the beam from the Main Injector is destroyed. To reduce the spread, the beam is monitored and when there is any exceptional deviation, a signal is sent to a dipole magnet that is placed out of phase with the beam, named a kicker. The kicker is activated by the signal and as the errant grouping passes and is knocked back into phase with the beam in a process known as stochastic cooling. This is done several times, but the integrity of the beam is restored within the time frame of delivery of bunches to the anti-proton source, or two seconds.

Accumulator

After the beam is cooled in the debuncher and prior to the next shot to the p-bar source from the main injector, the 8 GeV p-bar beam is sent to the Accumulator. As its name implies accumulates the anti-protons. Inside the accumulator the p-bars are returned to an 84 bunch structure as in the Booster and can be stored either in the accumulator or can be sent to the main injector or recycler.

3.1.5   Tevatron

The Tevatron is the final stage of acceleration, and will take the bunches of protons and anti protons from 150 GeV, to their final energy of 980 GeV. The Tevatron is enclosed in 2 km diameter loop and housed roughly 30 feet below ground level. The Tevatron makes use of superconducting magnets in order to keep the nearly 1 TeV beams in line and in focus. The magnets are cooled with liquid helium to a temperature of 4.6K and produce dipole fields as high as 4.4 T. With approximately 1000 magnets, over 350 MJ are stored in the magnetic fields during operation. Again, the two beams share the same beampipe orbiting one another in a double helix roughly five millimeters wide. As the beams near one of two interaction points a specialized quadrapole magnet brings them into sharp focus. The 36 bunches are separated into three superbunches of 12, spaced 2.6 μs apart, with collisions every 392 ns.

Chapter 4

THE DØ DETECTOR
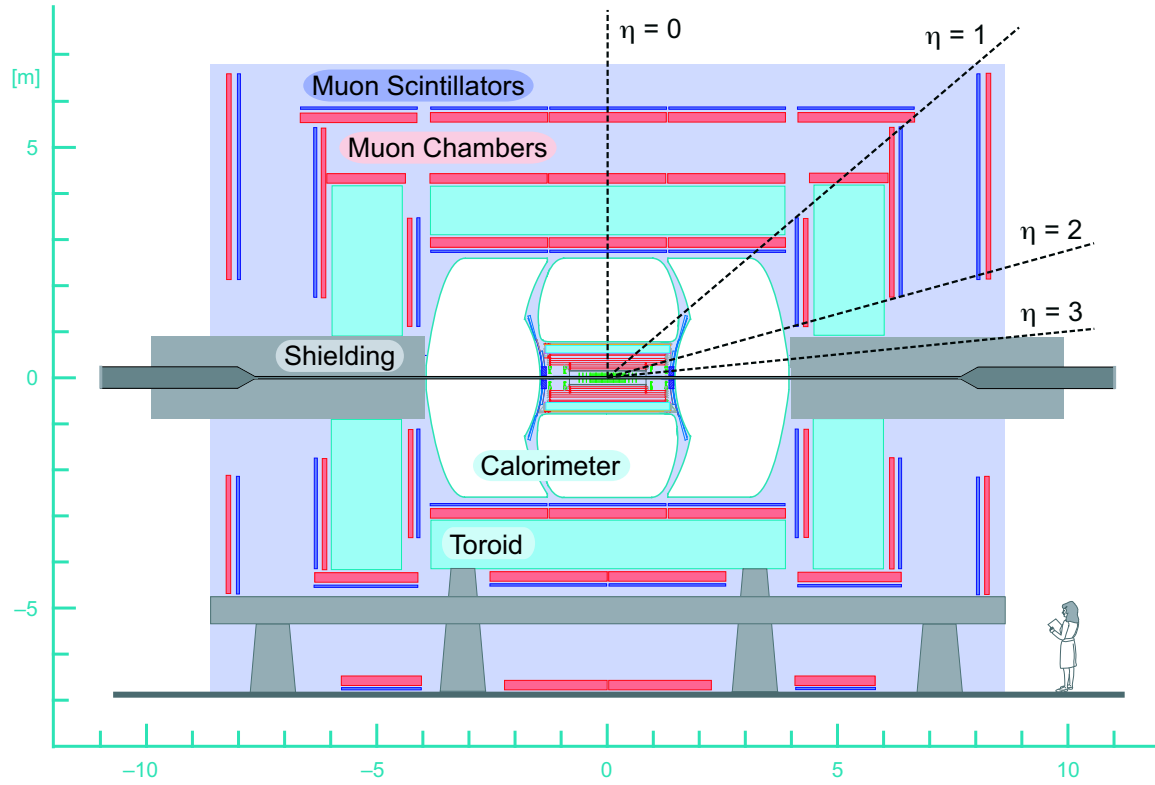
Figure 4.1: The upgraded Run II DØ Detector [12]

The Run II DØ detector [12], shown in Figure 4.1, is a multipurpose detector placed on one of the interaction points of the Tevatron. It is uses successive cylindrical detectors, and separable endcaps outside of the inner subdetectors that allow access, with the longitudinal axis of the detector along the beamline. There are three main sections to the detector, each roughly delineated by large magnets. The detector employs different technologies

for particle identification and measurement in each layer according to the kinematics of the events expected. The innermost region consists of tracking detectors surrounded by a solenoid magnet that allows for the bending of charged particles and thus a measurement of measurements of particle momenta. The middle layer consists of a sampling calorimeter used to capture and estimate the energy of particles escaping the tracker. This is surrounded by a toroid magnet used to provide further bending of any charged particle escaping the calorimeter, which are almost exclusively muons. The outermost layer is used to measure the curvature of the muons in the magnetic fields.

In describing the detector a modified cylindrical coordinate system is useful. The longitudinal coordinate, along the beamline, remains the z coordinate, and the azimuthal is the familiar ϕ. The non-Lorentz invariant polar angle, θ, is replaced with the quantity rapidity. It is defined as

$$y = \frac{1}{2} \ln \left(\frac{E + p_z}{E - p_z} \right) = \frac{1}{2} \ln \left(\frac{1 + \beta \cos \theta}{1 - \beta \cos \theta} \right) \tag{4.1}$$

In the limit $\beta \to 1$ or $p \gg m$ we can take $\cos \theta = \tanh y$. From this we define *pseudorapidity* as

$$\eta = - \ln \left[\tan \frac{\theta}{2} \right] \tag{4.2}$$

When measured from the center of the detector, values of η are shown in Figure 4.2. As described in the figure, the values are refereed to as η_{det} as they describe the detector coordinates. Generally, η is defined from the point of collision, and thus a distinction is made between the two.

4.1 The Tracking System

The Run II upgrade included the insertion of a 2T solenoid magnet. With the addition of this magnet, a precision tracking system was needed. DØ employs two tracking detectors inside of the solenoid. The innermost detector is a Silicon Microstrip Tracking (SMT) detector. Outside of this is the Central Fiber Tracking (CFT) detector.
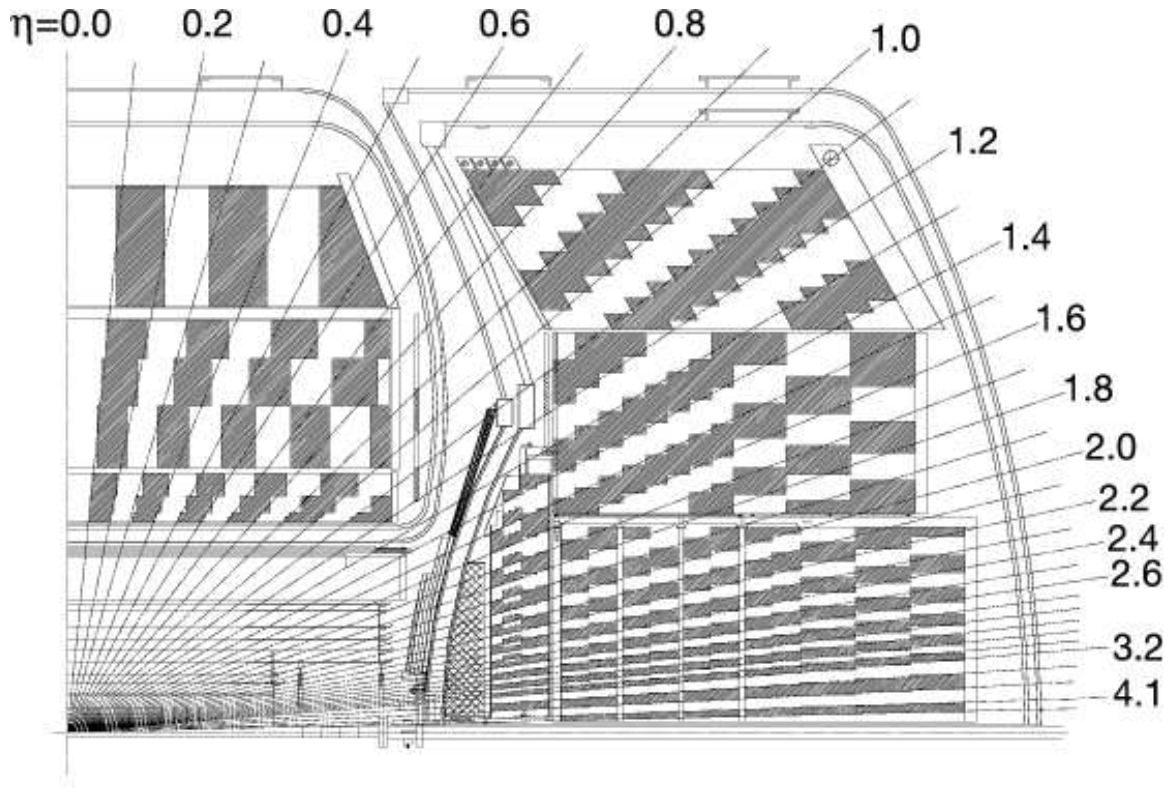
Figure 4.2: Segmentation of the DØ Calorimeter in Pseudorapidity. When defined from the detector center, as shown here, this is η_{det}

4.1.1 Silicon Microstrip Tracker

Modern particle physics experiments have increasingly used solid state diodes as a means of highly accurate charged particle detection. When put under reverse bias, the depletion region, the inslating region within a semiconductor, widens and virtually no current will flow. For Silicon the band gap is roughly 1.1 eV, and a charged particle of roughly GeV magnitude, when acting as a minimum ionizing particle (MIP), will succeed in breaking down the down the diode and allow current to flow, creating a signal indicating the presence of the particle. The diodes at DØ are constructed using long thin strips of p-doped silicon
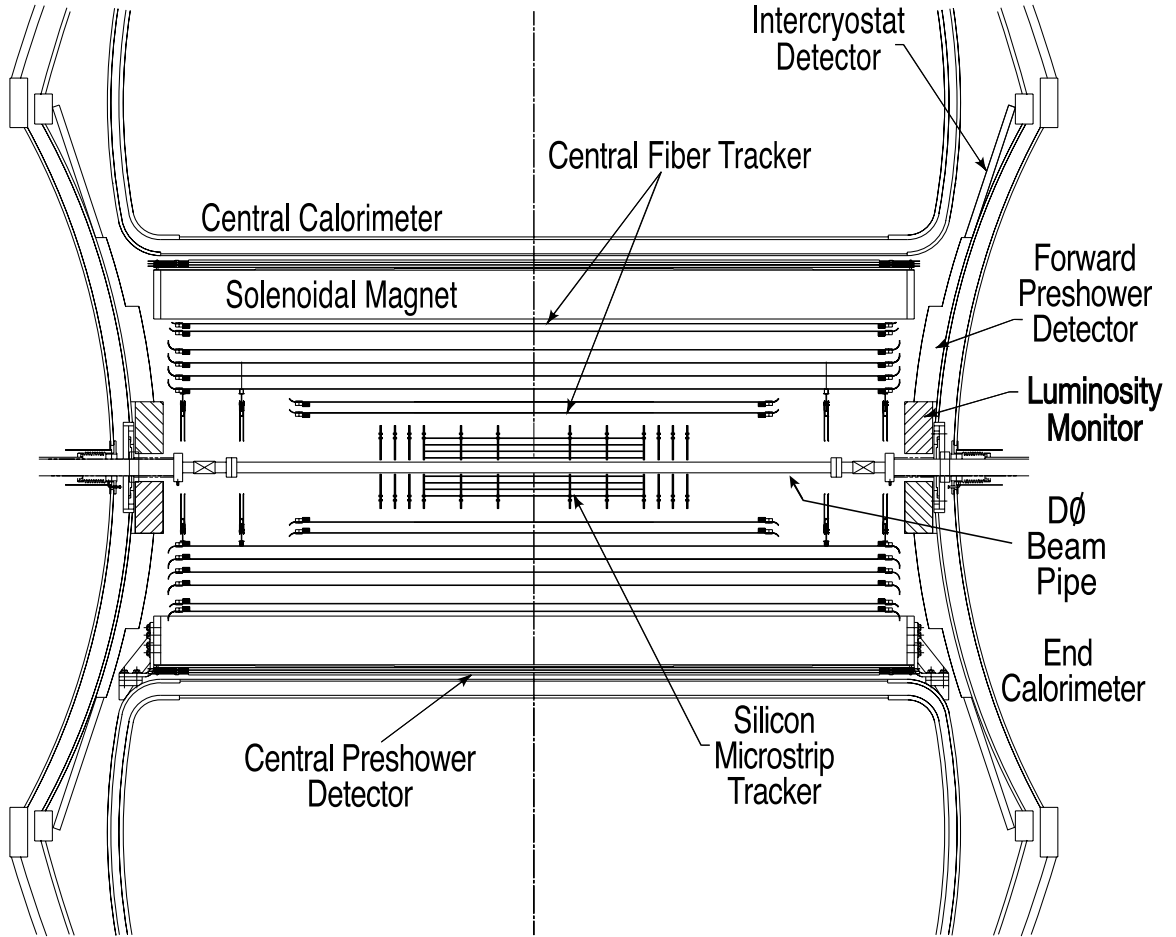
Figure 4.3: The Tracking system

on n-doped wafers, called microstrips. The microstrips have a typical spacing of 50 μm. To increase sensitivity a heavily n-doped microstrip may be put on the opposite side of the wafer at an angle, called a stereo angle, to the p-doped strips to allow spacial resolution in all three dimensions. This configuration is called a double sided sensor.

The Silicon Microstrip Tracker (SMT) is situated directly around the beam pipe and is the first point of active detection particles coming from collisions. It's primary purpose is to determine where in the interaction region of the detector, the approximately 25 cm in

either z-direction from the geometric center of the detector, the hard scatter from the bunch crossing occurred. This is known as vertexing and is described in section 5.2. The length of the interaction region was a determining factor in the hybrid design of the SMT [13]. The hybrid design, shown in Figure 4.6 consists of barrels centered around the beamline for measurement in the $\rho - \phi$ plane. Interspersed among the barrels are disks perpendicular to the beam line, as well as sets of disks at each end providing measurement in the $\rho - z$ plane as well. This design allows for complete η coverage for vertexing in three dimensions, with high η coverage in the disks and low eta coverage primarily in the barrels.

Each of the six barrels measure 120 mm and consist of 4 layers. Each of the layers each contain a sub layer as shown in Figure 4.5. In 2006, for Run IIb, a single layer, i.e. with no sublayer architecture, named layer 0 was inserted about the beampipe. The innermost sensor surface is at 16mm from the beam and outer and outermost at 94mm. There are a total of nearly 400,000 channels in the barrels of the SMT.

The 12 inner disks, known as F-disks are situated about the interaction point such that one disk exists between each barrel, save the two electrically insulated around the interaction point, and a grouping of three on each end. The disks consist of twelve trapezoidal wedges rotated by 7.5 degrees with respect to its neighbor. The F-disks extend from a radius of 26mm to 105mm. The H-disks consist of 24 wedges, spanning a radius of 96mm to 236mm. For Run IIb, the outermost H disks were removed.

4.1.2   Central Fiber Tracker

As a charged particle passes through a scintillating material, it causes an atomic excitation and the subsequent release of a photon of a known wavelength. Long thin strips of scintillating material can be made to transmit photons via total internal reflection and thus indicate the presence of a charged particle along the length of the fiber. A visual light photon counter (VLPC) is attached to the end of the fiber and is used to convert the photons to an electric signal. The central fiber tracker (CFT) employs this concept by using concentric rings of scintillating fibers to indicate the path of a charged particle. Because the particles are made to run the length of the interaction region and beyond, they are poor indicators

of the z-position. They do provide excellent and complete ϕ coverage, assuming sufficient layering. For this reason the CFT is used only for tracking. [1]

The CFT is made up of eight concentric rings along the beam line. The innermost ring begins at a radius of 20cm and the last at 52 cm. Each ring consists of two layers of scintillating wire, each with a 835 μm diameter. One layer of of each ring lays along the axial direction, while the other is at a stereo angle of $\pm 3^o$, alternating sign by ring. In the inner two layers, the fibers are 1.66m long to accommodate the H-disks of the SMT. All other layers contain fibers with a length of 2.52m.

4.1.3   Magnets

The inclusion of a 2T solenoidal magnet inside the calorimeter has made possible momentum measurements by the tracking system. When used in concert with the 1.9T toroid outside the calorimeter, this also provides more precise measurements of muon momenta. In addition to bending, the polarity of the magnets can be put into four different configurations allowing for measurements of charge asymmetry and elimination of any bias due to particle identification of a certain charge.

4.2   Calorimetry

As the particle passes through the magnetic field and the trackers, we can measurement its momentum. For complete reconstruction of charged particles, and for the neutral particles that escape the tracking system, we must measure the energy. To measure this we use the next section of our detector, the calorimeters. In the tracking detectors we took care to design detectors that would minimally interfere with the particle so as the momentum could be kept constant and measured by the curvature due to its charge. Because no analog to this curvature measurement exists for neutral particles we are chiefly concerned only in capturing the particle to measure its energy, and thus create maximal interference.

---

[1] With the recent upgrade in readout electronics for the CFT, timing of incoming photon pulses from an event can give a rough estimation of the z-coordinate. This is due to one pulse directly from the scintillation and another from the reflection at the end of wire opposite the PMT. Δt for this gives a rough estimate that has yet to be incorporated in any DØ analysis

4.2.1   Lquid Argon-Urnanium Calorimeter

An ideal calorimeter accomplishes two tasks. First, it captures all of the incident particles energy, and, second, it transmits that information in a useful manner. A calorimeter that accomplishes both of those tasks with one material is called an homogeneous calorimeter. A calorimeter made of the scintillator, polystyrene, which has a decay length of roughly 40 cm, would require a 20m thick surface to absorb the energy of a high energy photon, for example. Instead, we use a heterogeneous, or sampling, calorimeter. This uses very dense material, with a very short radiation length, to induce particles to decay or radiate. These dense inactive regions are immersed in an active material that can transmit the ionized radiation. By taking these samples we can reconstruct the energy of the incident particle.

There are three calorimeters at DØ . Each is similar in design, but covers a different fiducial region. As shown in Figure 4.7 there is a central calorimeter (CC) and two identical End Calorimeters (EC). The central calorimeter has full coverage up to $|\eta| < 0.4$, and partial coverage to $|\eta| < 1.0$. The EC has coverage up to $|\eta| < 4.0$, although for this analysis, only $|\eta| < 2.5$ will be considered.

One useful property of particles is that they exhibit different energy deposition patterns as a function of energy. Electromagnetic objects (EM), photons and electrons, tend to deposit a much larger fraction of energy after a few radiation lengths, due to their susceptibility to pair produce in a dense material. Hadrons, on the other hand, tend to penetrate further into a detector. Keeping this in mind, each calorimeter is sectioned accordingly. In the CC, there are three main sections. An EM section, a fine hadronic (FH), and a coarse hadronic (CH). In the EC, there is and EM section as well, but then a mixture of fine and coarse in the z direction. In the EM sections the absorber plates are thin, 3mm for the CC and 4mm for the EC, and made from pure depleted uranium. The FH sections are made from 6mm uranium-niobium(2%). The CH contain 46.5mm thick copper plates in the CC and stainless steel in the EC.

4.2.2 Muon Tracking

The only particle we expect to detect outside of the calorimeter are muons. With a mass nearly 200 times that of an electron, the muon will not lose a significant amount of energy through bremsstrahlung, and the muons are treated as minimum ionizing particles inside of the detector. As it is a charged particle, the muon will create a track inside the central tracking system, but lacking any more information, it is difficult to identify the muon. To improve on identifying the muon, a tracking system with an independent magnet is used outside the detector. As the corresponding surface area to cover is much larger, the resolution of the muon tracking system is not comparable to the inner tracking system, but it enables matching muons to the tracks in the inner tracking system. The toroid magnet creates a field roughly in ϕ, so there are naturally two components of the tracking system, the central and the forward systems, each consisting of separate detecting technologies, as shown in Figure 4.8.

Central Muon Tracking

The Central muon tracking system is made of three layers, appropriately named A, B, and C. Layer A is placed within the toroidal magnet and B and C are outside. The layers are made up of Proportional Drift Tubes (PDTs). A drift tube consists of a very thin wire suspended inside of a metal tube filled with gas. The wire is held at a positive potential to the surround tube so that when a charged particle passes through the gas and ionizes it the electrons will travel towards the wire. As the electrons drift towards the anode they will continually ionize the gas, yielding a much greater signal. Further, copper cathodes are placed around the wire to determine hits, the difference in time between the cathode pad hits and anode will provide information about the path of the muon inside of the tile. For this reason the tiles can be much larger for PDTs, and at DØ they are 10cm × 5.5cm. Muon coverage in the central region is $|\eta_{det}| < 1.0$

Forward Muon Tracking

The forward tracking in the muon system provides coverage for $2.0 > |\eta_{det}| > 1.0$. The particle density in the forward regions is expected to be higher, and therefore a finer granularity is sought. The detecting technology is called the Mini Drift Tubes (MDT). The MDTs are similar in structure to the PDTs, but have a cross-section of about 1 cm $\times$ 1 cm. The gas inside the drift tube also has a much shorter drift time. The forward muon tracking system keeps the same A,B,C layering as the central system.

In addition to the PDTs and MDTs, scintillation counters are placed throughout the detector to provide timing information that accomplishes two tasks. First, the mean drift time of muons in the tracking system can be larger than the bunch crossing time, so to properly assign muons to a $p\bar{p}$ event this information is needed. Second, cosmic ray muons can penetrate to the detector. Providing timing information on these can both detect an implausible direction from a $p\bar{p}$ collision and a muon that is out-of-time with the bunch crossing.
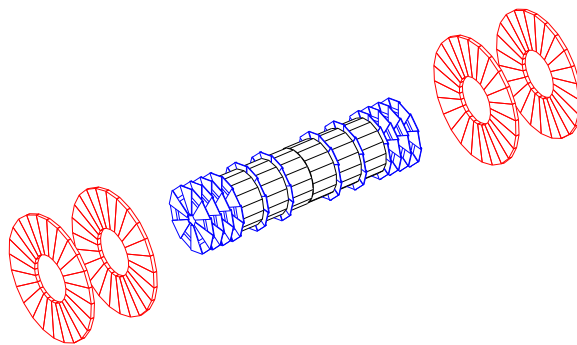
Figure 4.4: The Silicon Microstrip Tracker (SMT)
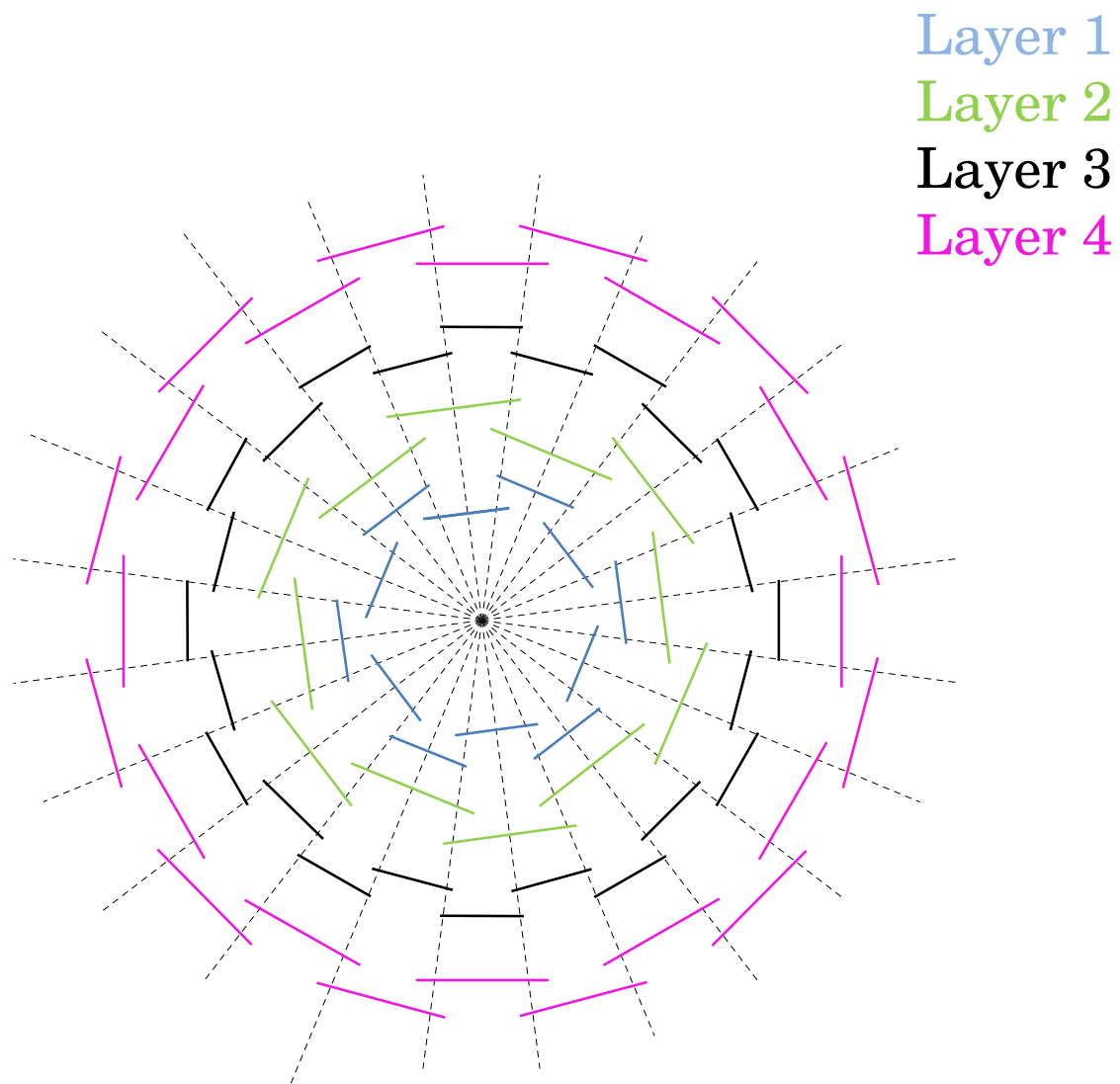
Figure 4.5: The Silicon Microstrip Tracker Barrel Layers
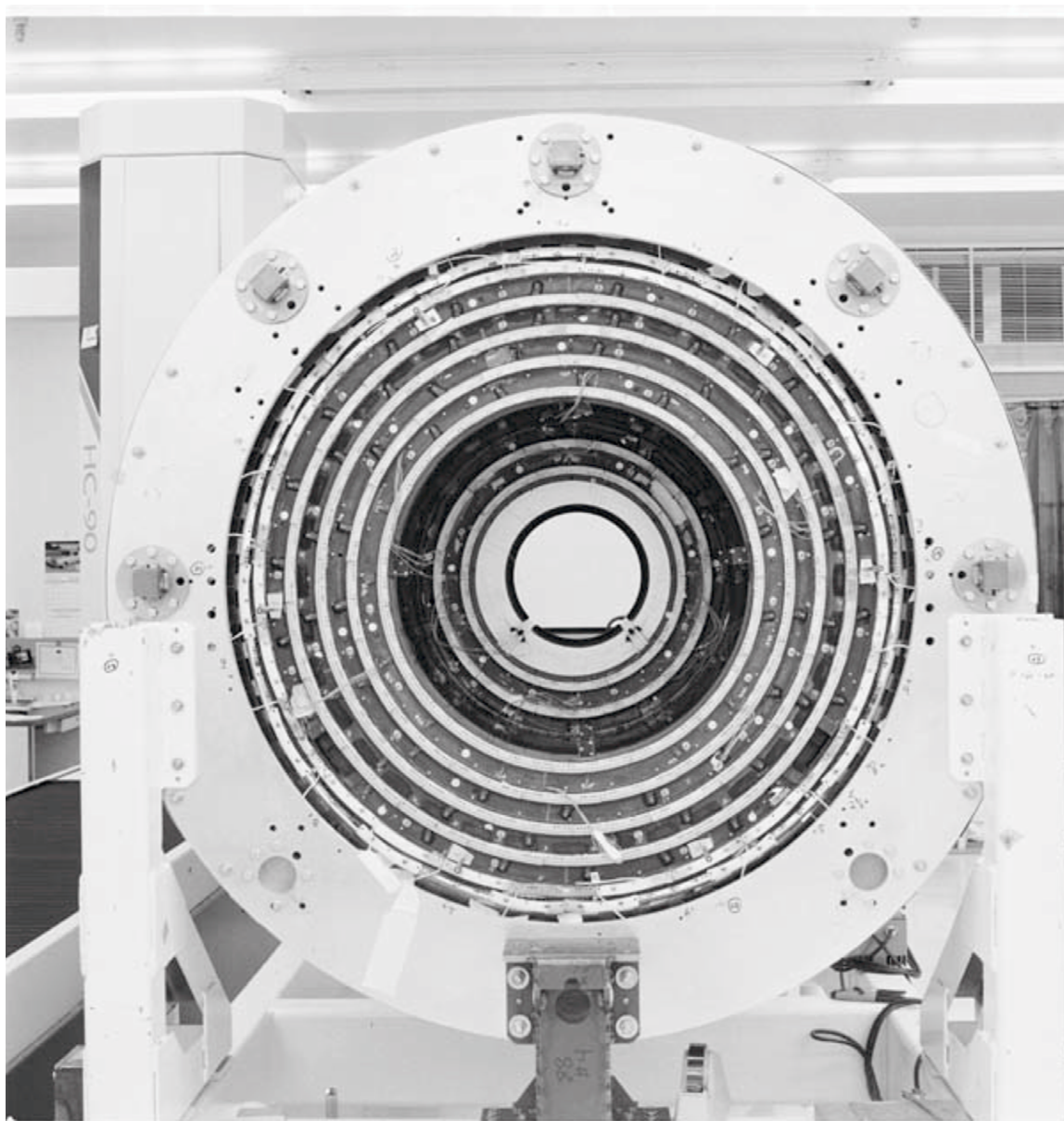
Figure 4.6: The Central Fiber Tracker (CFT))

END CALORIMETER

Outer Hadronic
(Coarse)

Middle Hadronic
(Fine & Coarse)

Inner Hadronic
(Fine & Coarse)

Electromagnetic

**CENTRAL
CALORIMETER**

Electromagnetic

Fine Hadronic

Coarse Hadronic

1m
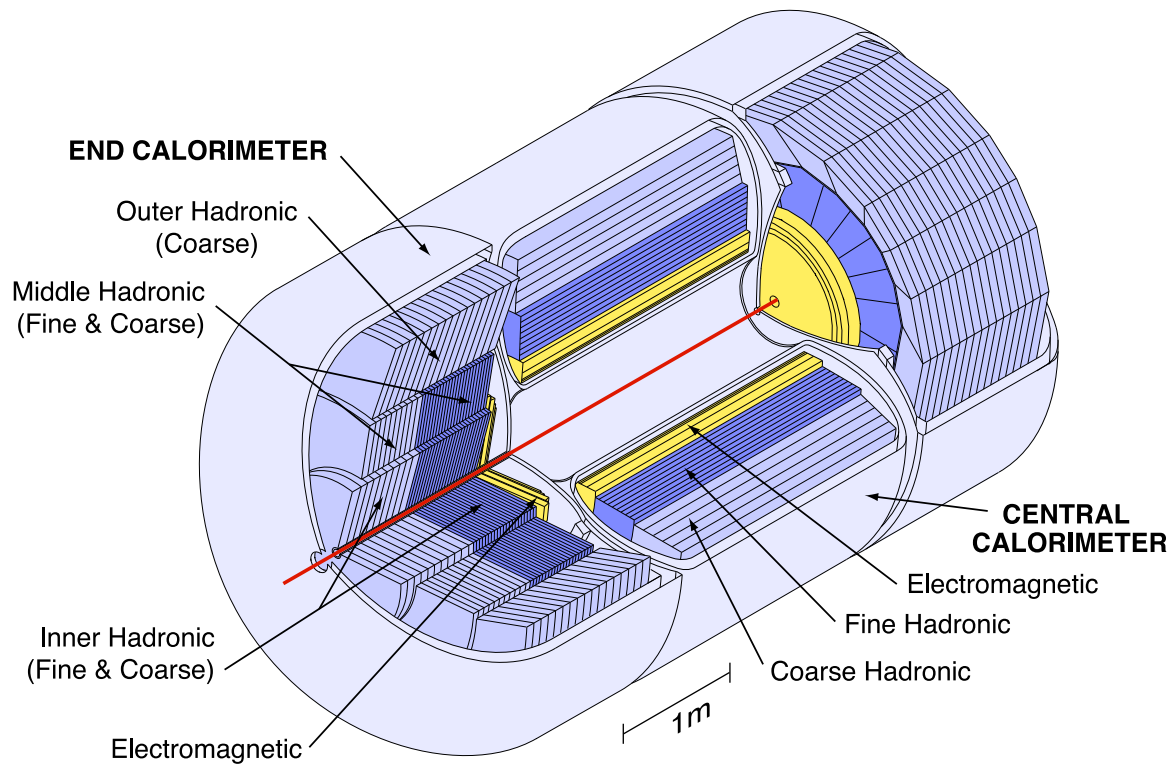
Figure 4.7: The DØ Liquid Argon-Uranium Calorimeter
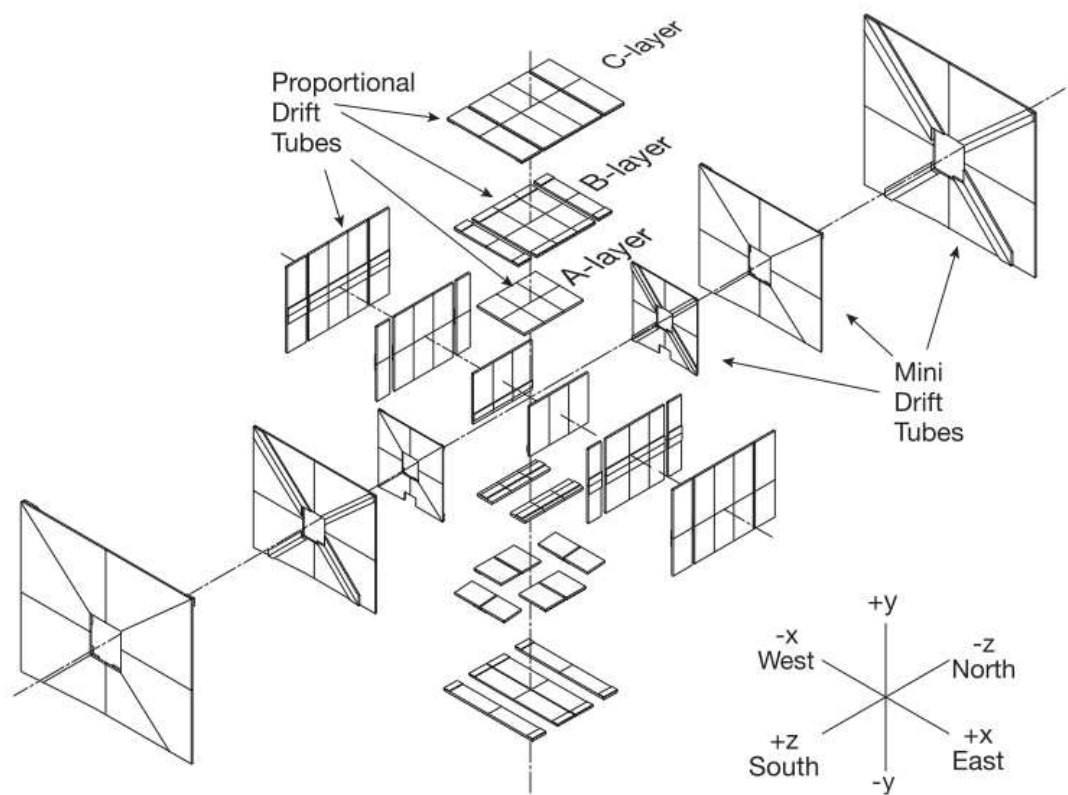
Figure 4.8: The DØ Muon Tracking System

Chapter 5

OBJECT RECONSTRUCTION

The chaotic environment accompanying a bunch crossing yields complexitywhich can seem simply overwhelming. With thousands of particles being created, decaying, leaving tracks, depositing energy, or simply ignoring the detector, it is hopeless to attempt to identify all but the most unique signatures. We reconstruct common large scale objects that can be pieced together to create the signature of a unique particle. An electron from a Z decay in associated production, for example, will come from the hard scatter event. We expect at least two electrons from the Z so we look for many tracks that can be traced back to the same area in the interaction region. Some of these tracks can be matched to calorimeter deposits. We expect that the bulk of the electron's energy will be deposited in the first few layers of the calorimeter. None of these alone can identify the electron, but putting them together can identify the electron (the specific criteria for lepton identification are given in section 5.3). From this we can create a four-vector for the electron, and, presumably its partner positron. Then we can use these four-vectors to determine the Z^0 mass, or we can calibrate the detector so the four vectors yield the Z mass.

The work presented in the following chapters is the result of years of work by hundreds of physicists who have been members of the DØ collaboration. The bulk of object reconstruction presented below has was done before the author was a member of the collaboration. The notable exception being the work with trackcaljets. The work in Section 5.6 was done by Anna Goussiou, Aurelio Juste and Prolay Mal among others. The author, along with Prolay Mal, derived and applied the corrections in Section 5.6.4.

5.1 Tracks

The two tracking subdetectors were designed to provide points of interaction for charged particles being bent in magnetic fields. We would like there to be minimal interaction

between the particle and the active detecting agent. However, there are a number of support structures, and readout devices that a particle may traverse inside the detector. In fact, a particle may travel through multiple radiation lengths of material inside the tracking subsystems. Further, in the high luminosity environment of Run II, multiple tracks or charged particles may make hits, or scattered particles may make hits in close proximity to the original particle of interest, and this all on top of energy loss from the particle traversing dense matter. All of these effects must be compensated for by our track-making algorithm.

A hit is the result of a signal from deposited energy in any of the detector elements in the tracking subsystem that is used to determine the position of the particles. A track is the ordered list of hits associated with the charged particle. Before describing the process of forming tracks from hits, it is useful to study the interactions that will cause a deviation from the pure form of the motion of a charged particle in a magnetic field as governed by the Lorentz force. The two primary effects are multiple scattering and energy loss due to interaction with material. We assume these are independent effects.

In the central tracking region of the detector, the thin multiple scattering approximation is used exclusively. This approximation can be used in the limit that the material is thin enough that the error introduced in the track position is not significant compared to the error in the measurement of the track position. The formula given for the deflection angle in a plane due to multiple scattering is [9]:

$$\theta_0 = \frac{13.6 MeV}{\beta c p} |q| \sqrt{\frac{L}{L_R}} [1 + 0.038 \log(L/L_R)] \tag{5.1}$$

where L is the thickness and L_R is the radiation length of the traversed material.

Energy loss in a material is given by the Bethe-Bloch equation [9]:

$$\frac{dE}{dx} = -\rho K z^2 \frac{Z}{A} \frac{1}{\beta^2} B(\beta) \tag{5.2}$$

where ρ is the density of the material, z is the charge number of the incident particle, Z and A are the atomic number and atomic mass, respectively, of the material, and K is a constant.

If we combine these two effects we can fully describe the trajectory of a particle as it

travels through our detector. We require that one of the main features of our tracking-finding algorithm is that it is iterative. That is once a track can be described it will search for a hit that can be added to the track, and once a hit is found, a new track is formed. Then the process repeats. This is also vital for a second condition of our tracking algorithm, that it be tunable. We need to be able to adjust parameters to optimize the trade off between track finding performance and computing usage. These two characteristics of the track finding algorithm lay the foundation for the very complicated track finding algorithm used at DØ .

A path is the ordered list of surfaces traversed by the track. A path may be extended by adding a surface. The list of complete paths serves as the map for track finding, and paths which produce low numbers of good tracks may be excluded. Once a track is propagated to a new surface, a cluster may be added to the track if the the newly formed track passes a χ^2 criterion. After several additions and iterations, a full set of tracks is formed. Then an additional fit to the track is made and if the passes another χ^2 criterion, the track is used.

5.2 *Vertices*

Once again, due to the high luminosity environment of Run II, several interactions take place with each bunch crossing. More importantly, there may be multiple hard scattering interactions in the same bunch crossing. We search for the origin of the hard scattter events along the beam line. An origin of a hard scatter event is known as the primary vertex.

Vertexing in the z-direction is done via a histogramming method [14]. All tracks with greater than eight stereo CFT hits are binned in the z range of 100cm from the geometric center of the detector, according to the z-coordinate of the beginning of the charged particle's trajectory that leaves the track. The number of tracks in each bin is multiplied by the summed p_T of the tracks. The maximum adjacent 2 bins are selected and the z position is calculated as the mean of the z coordinate of the helices, this is done as the tracks from the hard scatter can be spread over 1-2 cm. The p_T weighting is used to negate the effect of vertices arising from collisions other than the interesting hard scatter, or "minimum bias" vertices. To exclude the effect of fake tracks, a maximum cut is put on the p_T.

In $x - y$, vertexing is done with an impact parameter minimization algorithm which is

fully discussed in [15]. However, once vertices are fully described, an iterative process is used to determine the set of tracks forming the best vertex. First, the following are applied to the tracks:

- Total number of stereo hits ≥ 7

- Number of SMT hits ≥ 2

- $|Z_0 - PV_z| < 1$cm

- $|d_0/\sigma_{d_0}| < 3$

The limit on stereo CFT hits reduces the number of fake tracks, and the number of SMT hits assures adequate resolution in the x-y plane. The third criterion reduces the effect of minimum bias vertices. To reduce contamination from secondary vertices the track must be consistent with the beam position, d_0 within errors.

If two or more tracks pass this criteria the vertex and χ^2 are calculated with all tracks. Each track is removed and these quantities are recalculated. The track that causes the maximum change is χ^2, $\Delta\chi^2_{max}$ is removed if the value of $\Delta\chi^2_{max}$ is greater than Δ_{max}. This is repeated until $\Delta\chi^2_{max} < \Delta_{max}$, or if there is only one track remaining the beam spot is returned.

5.3 Lepton Identification

While this search is optimized for the invisible decay of vector bosons, we readily accept events that satisfy our selection criteria and are rejected from other analyses. Those analyses, such as the associated production of a W and Higgs boson where the W boson decays semi-leptonically, are optimized for leptons. It is the desire of the collaboration to be able to combine all searches in order to maximize sensitivity so events can not be analysed in two different searches. To account for this a common lepton identification requirement has been created, and we analyze events that fail these criteria.

For electron reconstruction, many variables are used to determine the quality of the electron [16]. The *isolation* is defined as $\frac{E_{tot}(\Delta R < 0.4) - E_{EM}(\Delta R < 0.2)}{E_{EM}(\Delta R < 0.2)}$. The *EMF* is the energy

fraction in the EM calorimeter, HMx8 is the output of the inverse of a covariant 8x8 matrix of correlated observables. *isoHC4* looks for an isolated track in a cone from 0.05-0.4 about the center of the EM object.

There are two sets of criteria for the CC and EC. For electrons in the CC:

- isolation < 0.07

- EMf > 0.97

- HMx7 < 25

- IsoHC4 < 2.5

- Hits on the road ef < 0.5

- NNout7 > 0.6

- $p_T > 15$ GeV

For electrons in the EC:

- isolation < 0.07

- EMf > 0.97

- HMx7 < 25

- IsoHC4 < 2.5

- Hits on the road ef < 0.5

- NNout7 > 0.6

- $p_T > 15$ GeV

A similar set of criteria are placed on muons, with special attention payed to criteria that help match signatures in the muon and central tracking systems:

- $|\eta_{det}| < 2.0$

- $p_T > 15$ GeV

- A track matched in the central tracking to a track in the muon system

- Hits in the A layer and BC layer of the muon system

- A track eith $dca < 0.04$ cm

- $\chi^2/d.o.f. < 4$ for the track fit

We veto an MC event with a lepton only if a random number, uniformly generated between 0 and 1, is lower than the ratio of data/MC identification efficiencies.

5.4   Jets

Until this point, we have spoke mainly of the colliding of two protons. However, the actual interactions that produces high-transverse energy events (hard-scattered) take place between two "partons", or pieces of the proton. For this discussion, the partons are the color fields of QCD, the quarks and gluons. Rapid hadronization due the locally decreasing strength of the strong force between quarks as their distance increases, color confinement, results in large numbers of neutral and charged particles. This process is known as fragmentation. The particles can have a significant relativistic boost allowing for the bulk of their energy deposit to be in a confined area of the detector. These, generally collimated, regions of energy deposition are refered to as jets. In an attempt to surmise the total energy of the original parton, we sum the energy deposited in the calorimeter believed to originate from

the parton and make reasonable corrections to estimate the partons energy. This is done by forming a cone[1] around areas of energy deposits in the calorimeter.

Throwing out the technically impossible infinitesimal granularity detector, we start with what would make the ideal cone algorithm [17]. First, the jet algorithm must be fully specified, meaning every step in the process of defining a jet needs to be fully defined as well as all kinematic variables as well as any internal algorithms used, such as an energy clustering algorithm. This needs to be done to insure the repeatability of the algorithm. The algorithm must be safe from theoretical deficiencies such as infrared singularities that can arise from soft radiation in events. The algorithm should give the same results regardless of what detector output is being used. The algorithm should behave the same whether being used on the output from a real experiment, a simulation of a hypothetical detector, or a simulation of a real experiment. While the first two requirements are vital to any algorithm, the last two may not be possible in any algorithm, so should be best approximated. The algorithm should be invariant under longitudinal boosts as the center of mass system of the parton-parton interaction does not coincide with the center of mass system of the particle-particle interaction. From a more practical perspective, the algorithm should provide the maximum efficiency in the least amount of CPU time. The jets should also have a minimal impact from experimental conditions, such as spectator particle contributions, noise , multiple iterations and the like. A reliable jet energy calibration must accompany the jet definition. Finally, as the jet algorithm has changed from the epochs in the experiment, the algorithms from Run I and Run II should agree within a few percent when run on the same events.

A large part of the effort in choosing the jet algorithm for Run II was spent finding the most reasonable procedure to find the stable cones of jets in the shortest amount of CPU time. A "seedless" algorithm would start from every possible point in an $\eta \times \phi$ grid and search for stable cones originating from that point. This is obviously too time intensive, however, if certain selection criteria were imposed to eliminate most of the seed-space, than this type of scan would become more feasible. The method is to find characteristics of good

---

[1]While the term cone will be used often in the formulation of jets, very rarely is the shape describing the perimeter of energy deposition a true cone. A true cone, in $\eta \times \phi$ space is the basis of the Snowmass cone algorithm.

seeds that enable them to become good seeds, also called proto-jets, for a jet algorithm. The first thought is that good seeds would most likely be surrounding the highest energy clusters, or close to the protojet axis. Unfortunately, this could be the result of collinearity or jets overlapping one another, and render unstable seeds. This was solved by midpoints, or adding together all stable seeds.

From here, it was decided to use all towers above a certain transverse energy threshold. However, when using a $\Delta\eta \times \Delta\phi$ space in 0.1 segments, this can have over 5000 calorimeter towers and a typical events can have hundreds of potential seeds. Thus, it was decided to use preclusters of towers, which also also the advantage of being less detector dependent because of the larger seeds. None of these processes can account for two overlapping jets, though. So it must be decided how the energy should be divided or whether it is more advantageous to simply merge the jets. This process is known as split-merge. In this case, the fraction of energy in the lower p_T proto-jet determines the split of energy unless it is above a certain fraction of the total energy, in which case it is merged to the other jet.

Similar algorithms are used to define electromagnetic objects and taus. Jets overlapping with an EM object or tau are removed. As described in Sec.6.3.6, JSSR is applied to MC jets. The uncorrected $\not{E}_T$ is computed from all calorimeter cells, except the cells in the coarse hadronic calorimeter which were not included in a good reconstructed jet. All corrections on the jets are propagated to $\not{E}_T$.

5.4.1 b-tagging

Because the primary final state for the Higgs boson with $m_H < 135$ GeV is a pair of b quarks, we require jets originating from these quarks in our analysis. The b-quarks exhibits a number of favorable characteristics useful in differentiating these jets from background. The b quark is much lighter than the W-boson, preventing any decay to the W boson, and also allows for hadronization of the b-quark. Hadrons including b quarks typically live 1-2 ps [18], allowing them to travel up to a millimeter, which forms a second vertex to be found with precision tracking. Also, the b hadron masses are sufficiently high that they often lead to high momentum leptons. All of these traits allow for methods of b-jet identification, or

b-tagging, to be optimized and used extensively and confidently in analyses.

In order for a jet to be considered for b-tagging it must pass a certain criteria, taggability. A taggable jet must be within $\Delta R < 0.5$ of an object called a *track jet*. Track jets are constructed from tracks with greater than one SMT hit, $dca_\perp < 2\ mm$ and $dca(z) < 4\ mm$, $p_T > 0.5$ and the Snowmass jet algorithm (a true cone in $\eta \times \phi$ space, is used to cluster tracks within $\Delta R < 0.5$.

To further refine the identification of these jets large numbers of them were simulated as well as large numbers of jets coming from light quarks. The characteristics of the secondary vertex expected to form with b jets and other discriminating factors were used in the training of a neural net (NN) to better discern when these were coming from a true b hadron or were being faked by light hadron. The variables fed into the NN are listed in order of importance here

- The decay length divided by its uncertainty (significance) in the transverse plane with respect to the primary vertex

- A variable considering the significance of all of the tracks in an event with respect to their dca

- A variable combining the impact parameter of the tracks in an event, considered a measure of the confidence the tracks are from a particular vertex

- The χ^2 of the secondary vertex fit

- The number of tracks used to construct the secondary vertex

- The mass of the secondary vertex

- The number of secondary vertices constructed

The output of the neural net for input b jets and light jets is shown in Figure 5.1

From Figure 5.1 we see that the b-tagging efficiency is very good, but there are still light jets passing b-id criteria for even very NN ouput. Thus a compromise must be made for
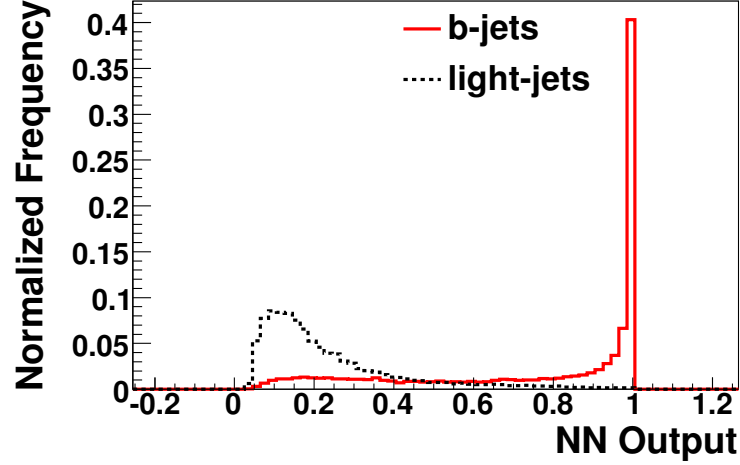
Figure 5.1: Output of the b identification Neural Net

a large number of bjets along with the minimal number of light jets. At DØ b jet *tagging points* are defined by the out put of the neural net. The choice of tagging point is described in Section 6.4.5.

5.5 Jet Energy Scale

The output of the jet finding algorithm yields a jet energy that suffers deficiencies arising from physics, instrumental and algorithm-dependent effects. The goal of the jet energy scale [19] is to correct the energy of these reconstructed objects back to their true particle level energy. The most general form of the jet energy scale correction is given by:

$$E_{jet}^{ptcl} = \frac{E_{jet}^{meas} - E_0}{F_\eta \times R \times S} \tag{5.3}$$

Where:

- E_{jet}^{meas}: The energy returned by the jet reconstruction algorithm

- R: The Response is an estimation of the amount of energy deposited into non-sensitive areas of the detector, including electronics dead material. This also accounts for

inefficiencies in the estimation of sensitive material

- F_η: The eta-intercalibration term is designed to correct the response of forward regions of the calorimeter to the more precisely measured central region

- S: The out-of-cone showering term is an estimation of the energy deposition of particles in a jet not accounted for in the reconstruction algorithm. It is also an estimation of the energy accounted for by the reconstruction algorithm, but not belonging to the original particle.

- E_O: The offset term accounts for energy deposition caused by calorimeter noise, multiple interactions in a beam crossing, and energy from previous collisions in the electronics.

In what follows, each correction is described and the form is given in more detail. Where available, an order of magnitude estimate is given. It is important to note, as described below, that the jet energy scale correction does not correct for the underlying event, such as multiple parton interactions and beam remnants, as this is already present at the particle level interaction.

5.5.1 Offset

The offset correction, as described above, primarily accounts for mechanical or electrical contributions originating from the detector, contributions originating from multiple proton-antiproton interactions in a single bunch crossing, and a constant correction due to the possibility of energy left in the electronics from previous bunch crossings. Therefore, there are two types of contributions to the offset correction which is given by:

$$\mathrm{E_O} = \mathrm{E_{NP}}(\eta, \mathcal{L}) + \mathrm{E_{MI}}(\mathrm{n_{PV}}, \mathcal{L}, \eta) - \mathrm{E_{MI}}(\mathrm{n_{PV}} = 1, \mathcal{L}, \eta) \qquad (5.4)$$

The first term, $E_{NP}(\eta, \mathcal{L})$ is a luminosity and pseudorapidity dependent correction that accounts for detector noise and electronic pile-up. This correction contains a full mapping of the detector to account for electronically active regions, radioactive sources, and other

areas that may contribute some form of radiation to the measurement. Also included is a correction estimating the probability pileup has occurred based on the magnitude of the Luminosity. This is measured in so-called "zero-bias" events. These are events which are triggered at every bunch crossing, but have no vertex in the event, and thus the energy density can be entirely assumed to be from detector noise.

The other contribution, $E_{MI}(n_{PV}, \mathcal{L}, \eta) - E_{MI}(n_{PV} = 1, \mathcal{L}, \eta)$, is from multiple proton-antiproton interactions. It is dependent on luminosity and the number of found primary vertices. As the number of primary vertices rises the more likely it is that there will be a contribution from a jet originating from another hard scatter in the same bunch crossing. This contribution is measured in "minimum bias" events, or events that are triggered in the luminosity monitors, and have at least one reconstructed primary vertices. Because this correction is for events with vertices in addition to the primary vertex for the interesting hard scatter, it is defined as the difference between the energy in events with two or more vertices and events with a single primary vertex.

Each correction is done as a per-tower energy density and thus contains a mapping of the entire detector, yielding the η_{det}-dependence in each form.

5.5.2   Response

The full response correction is comprised of two components; a finely tuned central calorimeter response R_{CC}, and a factor correcting forward regions of the calorimeter to the central region F_η. It is generally given as:

$$R = R_{CC} \times F_\eta \tag{5.5}$$

To accurately model this response, the missing E_T projection fraction method [20] is used. This method relies on the mechanism of the recoil of a jet against a photon in a $\gamma+$ jet event. In a perfect scenario, the photon and the jet would have matching transverse momenta.

$$p_{T,\gamma} + p_{T,jet} = 0 \tag{5.6}$$
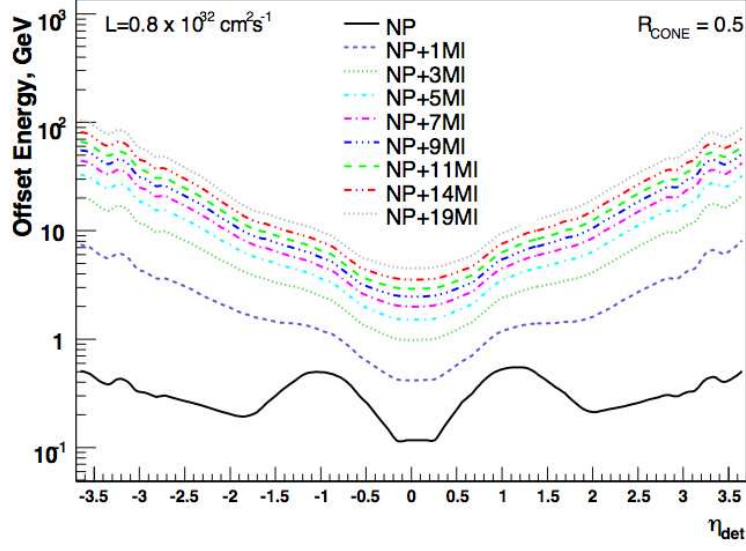
Figure 5.2: The Jet energy scale Offset correction. The solid black line represents the noise and pileup term, and the colored dotted lines account for the multiple interaction terms for different bins of primary vertices

In a real situation the response of the two objects would be different due to recoil from the jet and detector inefficiencies leading to a transverse momentum imbalance, such that:

$$R_\gamma p_{T,\gamma} + R_{jet} p_{T,jet} = -\overrightarrow{\not{E}}_T \tag{5.7}$$

The response of the electromagnetic calorimeter is necessarily one as it is determined from the $Z \rightarrow ee$ peak.

Setting the transverse momentum of the jet equal and opposite to the transverse momentum of the photon we can estimate the response as:

$$R_{MPF} = 1 + \frac{\overrightarrow{\not{E}}_T \cdot \overrightarrow{p}_{T,\gamma}}{p_{T,\gamma}^2} \tag{5.8}$$

The energy-dependence of the jet response is well described by a quadratic logarithmic function:

$$R(E) = p_0 + p_1 \log(E/E_0) + p_2 \log^2(E/E_0) \tag{5.9}$$

with $E_0 = 100$GeV and p_i are the fit parameters. Figure 5.3 shows the measurement of response in the central calorimeter ($|\eta| < 0.4$).
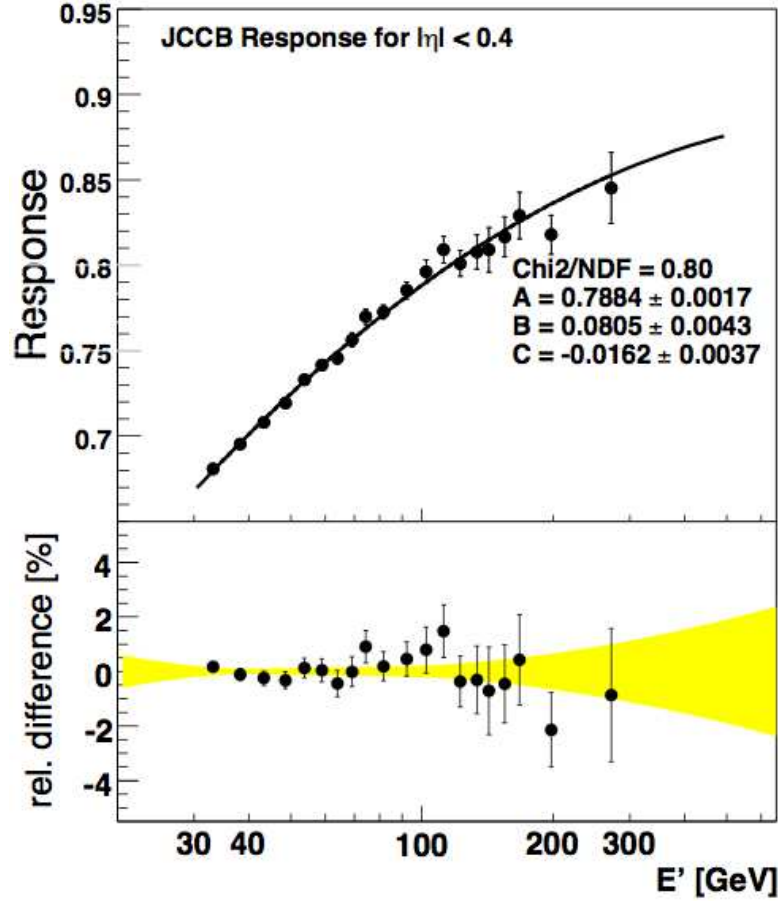
Figure 5.3: The jet energy scale central calorimeter response (the central calorimeter $|\eta| < 0.4$). The upper portion of the figure is the response calculated using the MPF method, with the data as points and the quadratic logarithmic fit as the solid line. The lower portion show the difference between the data points and the fit, with the 1-σ error in yellow.

Eta-intercorrelated Response

The central calorimeter region is fairly uniform, as is the end cap calorimeter when measured by themselves. However, the region in between these calorimeters, known as the intercryo-

stat (ICD) region is not well instrumented and has a non-uniform response. We therefore devise a correction to calibrate the forward jets to the central ones. This takes the form:

$$F_\eta = \frac{R(\eta)}{R_{CC}} \tag{5.10}$$

The response is calculated using a two dimensional fit of the above function in terms of E'. Figure 5.4 shows the relative response for certain values of E'.
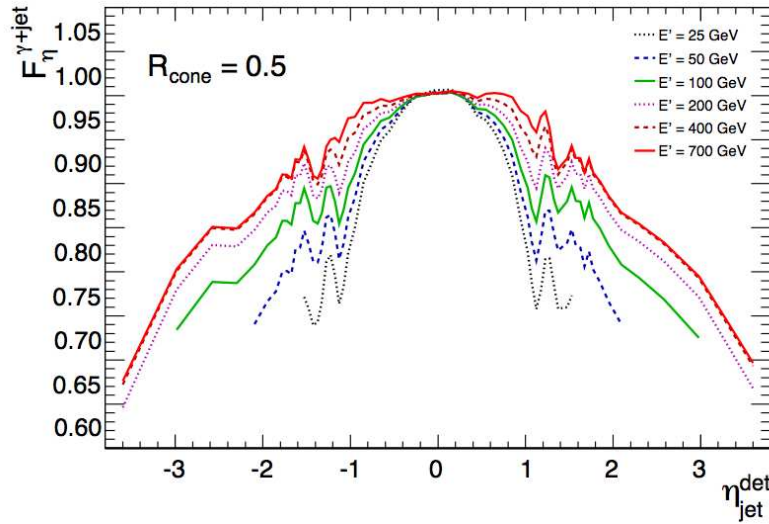
Figure 5.4: The Jet energy scale Eta-intercorrelated Response for different values of E'

5.5.3   Showering

The basic principle of the showering correction is to measure all true energy from a jet that is deposited in the calorimeter and compare this to the energy measured by the jet algorithm. As the true energy can only come from simulation, this is an entirely Monte Carlo derived correction that will be made on data. This correction accounts for energy from particles inside the jet cone depositing energy outside the jet cone, and particles outside the jet cone depositing energy inside the jet cone.

The showering correction is defined as

$$S = \frac{E_{jet}}{E_{act}} \tag{5.11}$$

Where

$$E_{act} = \sum_{allreco} E^{Reco} \tag{5.12}$$

and

$$E_{RECO} = E_{cell}\frac{E_{CAEP}}{\sum_i E_{CAEP,i}} \tag{5.13}$$

$$E_{CAEP} = \sum_{MCPart}^{j} \sum_{cells}^{i} (E_{CAEP_j})_i \tag{5.14}$$

A CAEP cell is a MC object that measures the energy deposition of individual particles in that cell. Therefore, $(E_{CAEP_j})_i$ is the measure of the individual energy deposit of a jth particle in a cell. E_{RECO} is used to calculate the fraction of reconstructed energy (what the would actually be read out) that the particle deposits in the cells. It does this by find the ratio of that particles CAEP energy to the total CAEP deposition and then using that ratio multiplied by the reconstructed energy. Lastly, to find the total energy deposit, we sum over all particles belonging to that jet. Figure 5.5 shows the showering correction for different $|\eta|$ regions.
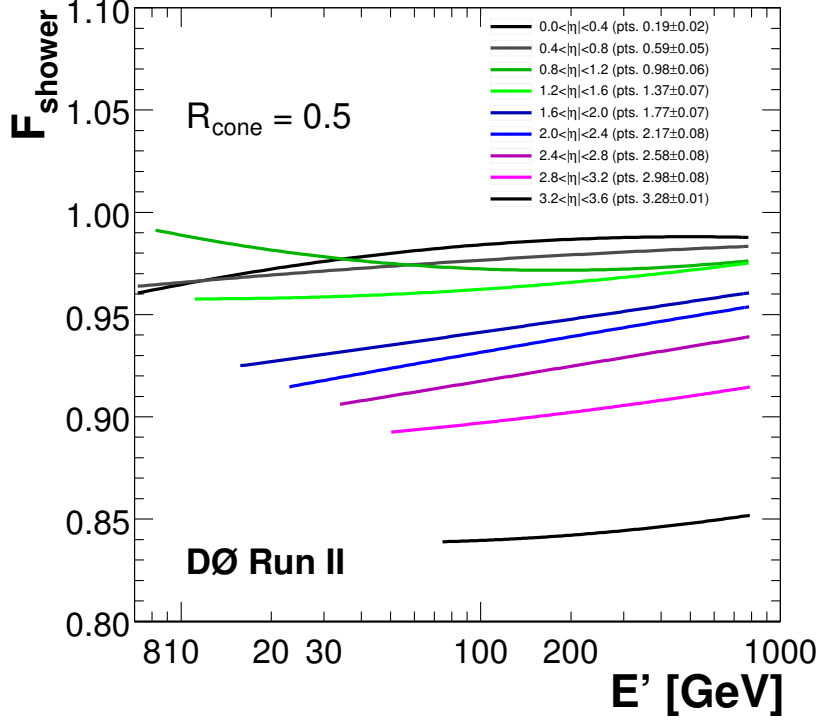
Figure 5.5: The Jet Energy Scale Showering Correction for different $|\eta|$ regions

5.6 Trackcaljets

We can use the momentum resolution of the tracker and its ability to reconstruct individual tracks within a jet to improve the jet energy resolution. At low momenta, where the tracker has greater precision, replacing the calorimeter energy measurements with track momentum measurements can significantly improve the raw jet energy resolution. Ideally, the energy deposited in calorimeter showers by charged particles inside of a jet would be replaced with the track momenta on an event-by-event basis. The DØ calorimeter does not have the granularity to accommodate such a measurement. Additionally, overlapping showers from neutral particles, which can not be isolated, may be present. Due to these limitations, we measure the *average* calorimeter response to a charged track inside a jet as simulated in
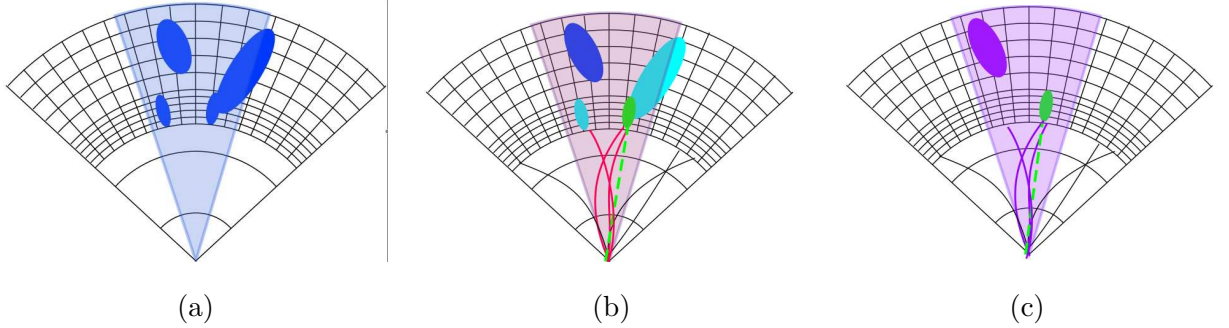
Figure 5.6: Diagram of the trackcaljet algorithm. (a) A normal calorimeter with a simplified cone outlined, the dark portions represent calorimeter energy deposits. Only energy in the cone is measured. (b) A hybrid of calorimeter and tracker, the charged particle tracks can be matched to the corresponding calorimeter deposits. (c) the final trackcaljet measurement has replaced some calorimeter deposits, however some neutral deposits need to be corrected for

Monte Carlo. We then use the average response to estimate shower energies from individual tracks.

The combination algorithm, known as the *trackcaljet* algorithm, begins with the raw jet energy as determined by the jet algorithm. For all tracks that are within a cone of $\Delta R = 0.5$ at primary vertex and within $\Delta R = 1.0$ at the calorimeter surface in the direction of the jet, average energies are subtracted from the calorimeter measurement and replaced with the corresponding tracker momentum measurement. The trackcaljet energy measurement can be written as,

$$\mathrm{E}^{\mathrm{raw}}_{\mathrm{Trackcal\ jet}} = \mathrm{E}^{\mathrm{raw}}_{\mathrm{cone}} + \sum_{\mathrm{track}} \mathrm{p}_{\mathrm{track}}[1 - \bar{\mathrm{R}}_{\pi^+}(\mathrm{p}_{\mathrm{track}}, \eta^{\mathrm{jet}}_{\mathrm{detector}}, \Delta \mathrm{R}(\mathrm{jet,\ track}))] \qquad (5.15)$$

In this formula, E^{raw}_{cone} is the uncorrected calorimeter jet energy derived from the JCCB ($R = 0.5$ cone) algorithm. P_{track} is the momentum of the track. $\bar{R}_{\pi^+}$ is the average charged pion response as determined by a charged pion in a jet environment in Monte Carlo. It is dependent on the track momentum, physics pseudorapidity and the angle between the track and axis of the jet cone. This average response allows for the replacement of the calorimeter measurement by the track momentum, as shown in Figure 5.6.

While the trackcaljet energy measurement is closer to the true particle level energy, it still suffers from the same deficiencies as normal jets. However, the precision of the jet energy scale correction can be enhanced by adding track dependence to previously inclusive measurements as well as using the replacement of calorimeter measurements by tracking information to lessen algorithm dependent effects. After this correction, the jet energy resolution of the two methods can be compared directly.

In the subsections that follow the derivation of the response function is further discussed. The track selection criteria and optimization are followed by the treatment of tracks matched to muons. This is followed by a discussion and derivation of the trackcaljet energy scale. Then results from resolution studies comparing calorimeter-only and trackcaljets.

5.6.1 Calorimeter response of a Charged Track

To measure the average calorimeter response of a charged track, careful attention must be paid to adequately model the complex environment inside a jet. It was decided to use a $\gamma + jet$ MC sample to model the jet environment as opposed to a single charged pion. In doing so, the radial dependence from jet axis of the charged track can also be modeled.

In an MC γ+jet event, the highest energy calorimeter jet is first matched to the corresponding particle jet within $\Delta R < 0.1$ and the jet is required to have $\Delta\phi > 2.8$ with respect to the photon direction [21]. After identifying the generated charged pions, CAEP cells are once again used to determine which part of the energy distribution in a cell originated from the charged pion. Thus, if a particle i has deposited an energy of E_i^{CAEP} into a calorimeter cell, the fractional energy is given by

$$f_i^{CAEP} = \frac{E_i^{CAEP}}{\sum_{j\epsilon\text{All particles}} E_j^{CAEP}},$$

(5.16)

which is summed over all particles making energy deposits in the same cell. The total energy deposition can then be written as:

$$E_i = \sum_{CAEP} f_i^{CAEP} \cdot E_{visible}^{CAEP}.$$

(5.17)

Where $E_{visible}^{CAEP}$ is the energy of the calorimeter cell corresponding to a CAEP hit and this is summed over CAEP cells with energy deposition.

As seen in the responses derived in the jet energy scale, the response of the calorimeter is not uniform throughout and therefore the calorimeter response has been derived as a function of η_{det} of the jets. We note also the charged pion response is also measured as a function of its distance from the jet axis. In order to perform statistically significant measurements in each of the $\Delta R(jet, track)$(at the calorimeter) bins, the charged pion tracks are binned in $\Delta R <$0.1, 0.1-0.2, 0.2-0.3, 0.3-0.4, 0.4-0.5 and 0.5-1.0. Figure 5.7 shows the binning. The position of the generated particles in the calorimeter is determined using the CAEP energy-weighted coordinates (η_{w}, ϕ_{w}) *i.e.*,

$$\eta_{w} = \frac{\sum_j \eta_j^{CAEP} \cdot E_j^{CAEP}}{\sum_j E_j^{CAEP}}, \quad \phi_{w} = \frac{\sum_j \phi_j^{CAEP} \cdot E_j^{CAEP}}{\sum_j E_j^{CAEP}} \tag{5.18}$$

where E_j^{CAEP} and $(\eta_j^{CAEP}, \phi_j^{CAEP})$ are the energy and coordinates of the j-th CAEP hit. Fig. 5.8 shows the charged pion responses in six different $|\eta|$ regions of the calorimeter. The calorimeter response ($\bar{R}$) of a charged pion is defined as the ratio of the energy, E_i in Eq. (5.17) to its true energy (E_{true}) *i.e.*,

$$\bar{R} = \frac{E_i}{E_{true}}. \tag{5.19}$$

5.6.2   Track Selection Criteria

To assure that only the highest quality tracks are used, an optimization of track criteria must be performed. As the primary function of the SMT is vertexing, the previous requirement of two hits will not be changed to assure the track is coming from the proper vertex. However, some care is taken to select the proper CFT and transverse momentum as we only wish to have tracks that improve the measurement. This primarily has to do with the upper end of the p_T spectrum, as the tracker momentum resolution becomes worse in this regime. For the low end, a particle must have at least 500 MeV to reach the surface of the calorimeter.

For the optimization of the track selection criteria, the γ+jet MC events are used. As a basic criterion, the event is required to have a reconstructed primary vertex and the jet under consideration must satisfy the cut of $\Delta\phi > 2.8$ with respect to the photon direction. In addition, the reconstructed jet is matched ($\Delta R(jet, $ Particle jet$) < 0.1$) to the corresponding
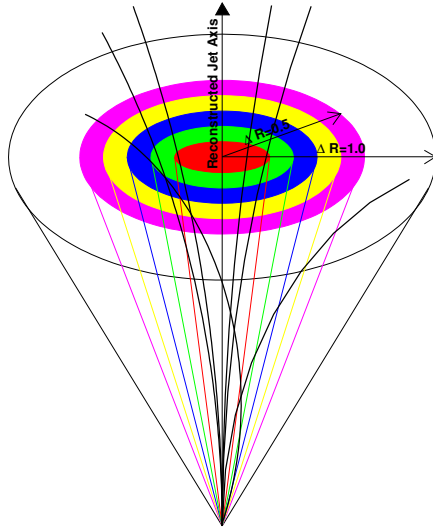
Figure 5.7: The cartoon diagram showing the classification of charged pion tracks for the measurement of charged pion responses inside the jet. The classification is based on the $\Delta R(\text{jet}, \text{track}) < 1.0$ at the calorimeter while the pion tracks are required to be within $\Delta R(\text{jet}, \text{track}) < 0.5$ at the primary vertex.
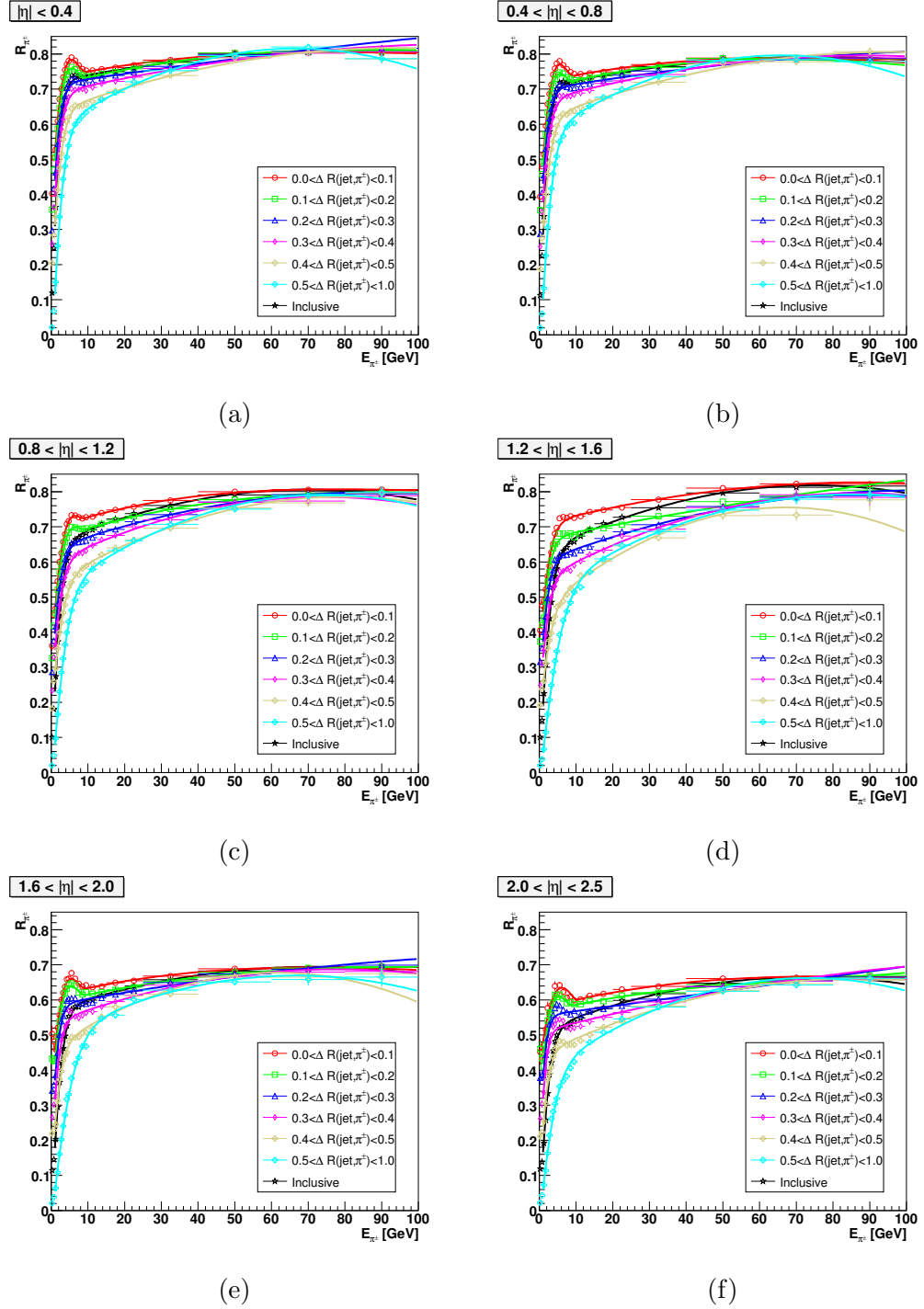
Figure 5.8: The calorimeter response ($\bar{\text{R}}$) of a charged pion inside a jet as a function of pion energy for six different regions: (a)$|\eta_{\text{jet}}| < 0.4$, (b) $0.4 < |\eta_{\text{jet}}| < 0.8$, (c) $0.8 < |\eta_{\text{jet}}| < 1.2$, (d) $1.2 < |\eta_{\text{jet}}| < 1.6$, (e) $1.6 < |\eta_{\text{jet}}| < 2.0$ and (f) $2.0 < |\eta_{\text{jet}}| < 2.5$. The dependence of the response on the distance of the pion from the jet axis is shown in different colors.

particle jet. As a first step of optimization, the tracks within $\Delta R^{PV}(\text{track, jet}) < 0.5$ and $\Delta R^{\text{calorimeter}}(\text{track, jet}) < 1.0$ are selected with the following criteria:

- Impact parameter $(x - y) < 0.5$ cm

- Impact parameter $(z) < 1.0$ cm

- Number of hits in SMT ≥ 2

- Number of hits in CFT ≥ 6 and

- $p_T \geq 0.5$ GeV.

A two-dimensional optimization is used to find the minimum number of CFT hits and maximum track momenta that can be used in the final track selection. The optimization criterion is the relative jet energy resolution, (σ_E/E). The ratio of the jet energy and energy of the corresponding matched particle jet $i.e.$, $\mathcal{R} = E_{\text{jet}}/E_{\text{particle jet}}$ are plotted first and the ratio of width (σ) and mean (μ) of such distribution $i.e.$, $\sigma_{\mathcal{R}}/\mu_{\mathcal{R}}$ determines the figure of merit for our consideration. It is to be noted that the optimization have been performed for the jets in different regions of the calorimeter as well as for different transverse momenta of the photon (p_T^γ). For a particular p_T^γ and η_{jet}, $p_{\text{T,track}}^{\text{max}}$ and $N_{\text{CFT hits}}$ are varied in the ranges of 2.5-50 GeV and 6-12 respectively to search for the FOM minima. Figs. 5.9-5.11 show the results of such optimization for different jet η as well as for p_T^γ =25, 50 and 100 GeV in $\gamma + \text{jet}$ events. Based on these optimization plots, the track selection criteria for $(N_{\text{CFT hits}}, p_{\text{T,track}}^{\text{max}})$ are fixed and the corresponding values are tabulated in Tab. 5.1.

5.6.3 Muon Track-matching

Muons are expected to be minimum ionizing particles in the detector, and are not subject to the average calorimeter energy expectation. However, we would still like to include the muon momenta measurement as part of the trackcaljet energy. Therefore, we need to subtract the minimum ionizing particle contribution from the muon and add the momenta. In the presence of muons inside a jet the trackcaljet algorithm becomes:

Figure 5.9: The optimization of track selection criteria (minimum number of CFT hits and maximum track p_T) in γ+jet events having $p_T^{\gamma} = 25$ GeV, for jets in six different regions of the calorimeter: (a)$|\eta_{jet}| < 0.4$, (b) $0.4 < |\eta_{jet}| < 0.8$, (c) $0.8 < |\eta_{jet}| < 1.2$, (d) $1.2 < |\eta_{jet}| < 1.6$, (e) $1.6 < |\eta_{jet}| < 2.0$ and (f) $2.0 < |\eta_{jet}| < 2.5$. The relative jet resolution $\sigma_{E_{jet}}/E_{jet}$ (see text), is considered to be the "Figure-of-Merit" for such optimization.
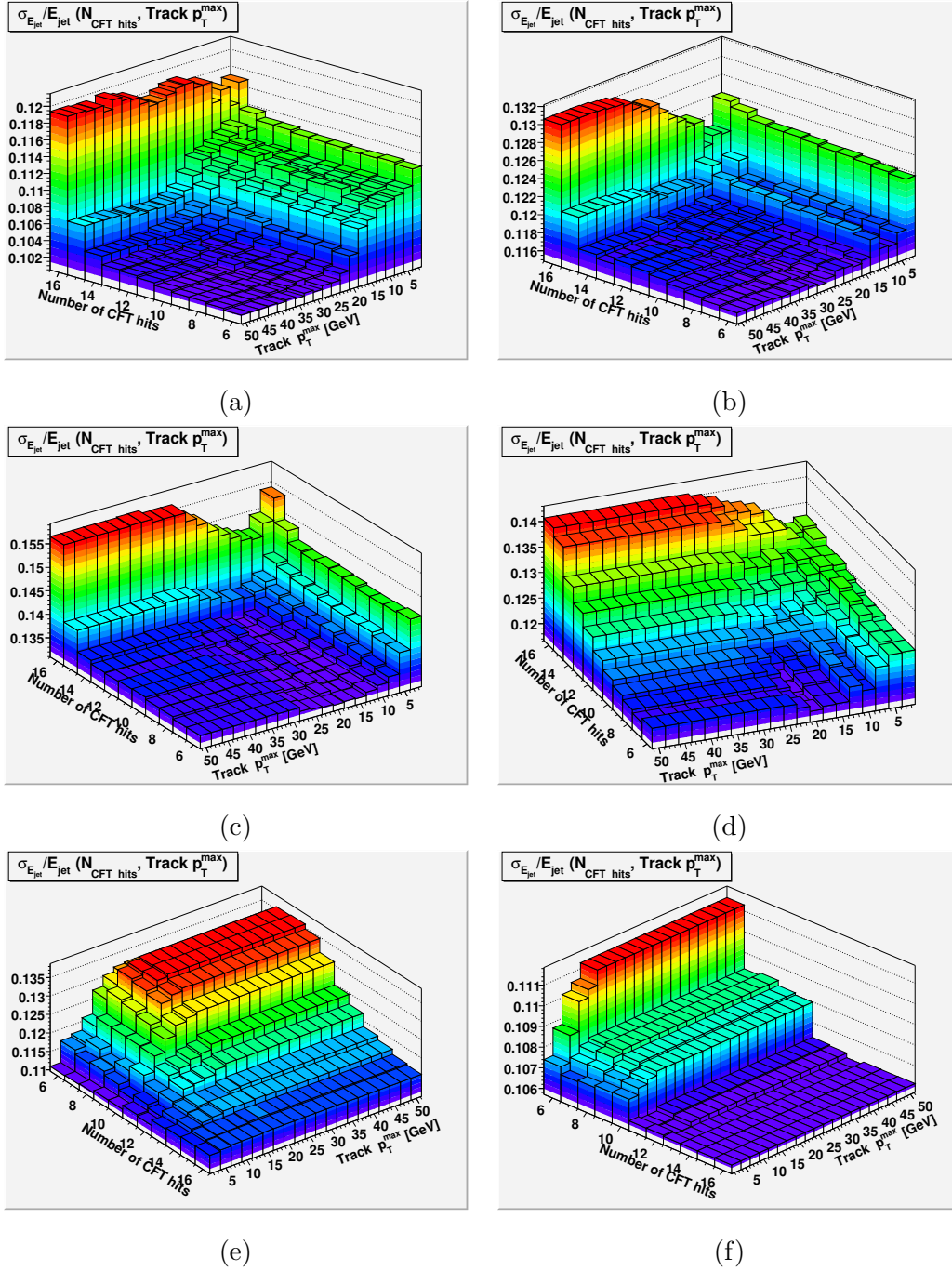
Figure 5.10: The optimization of track selection criteria (minimum number of CFT hits and maximum track p_T) in γ+jet events having $p_T^\gamma = 50$ GeV, for jets in six different regions of the calorimeter: (a)$|\eta_{\mathrm{jet}}| < 0.4$, (b) $0.4 < |\eta_{\mathrm{jet}}| < 0.8$, (c) $0.8 < |\eta_{\mathrm{jet}}| < 1.2$, (d) $1.2 < |\eta_{\mathrm{jet}}| < 1.6$, (e) $1.6 < |\eta_{\mathrm{jet}}| < 2.0$ and (f) $2.0 < |\eta_{\mathrm{jet}}| < 2.5$. The relative jet resolution $\sigma_{\mathrm{E_{jet}}}/\mathrm{E_{jet}}$ (see text), is considered to be the "Figure-of-Merit" for such optimization.
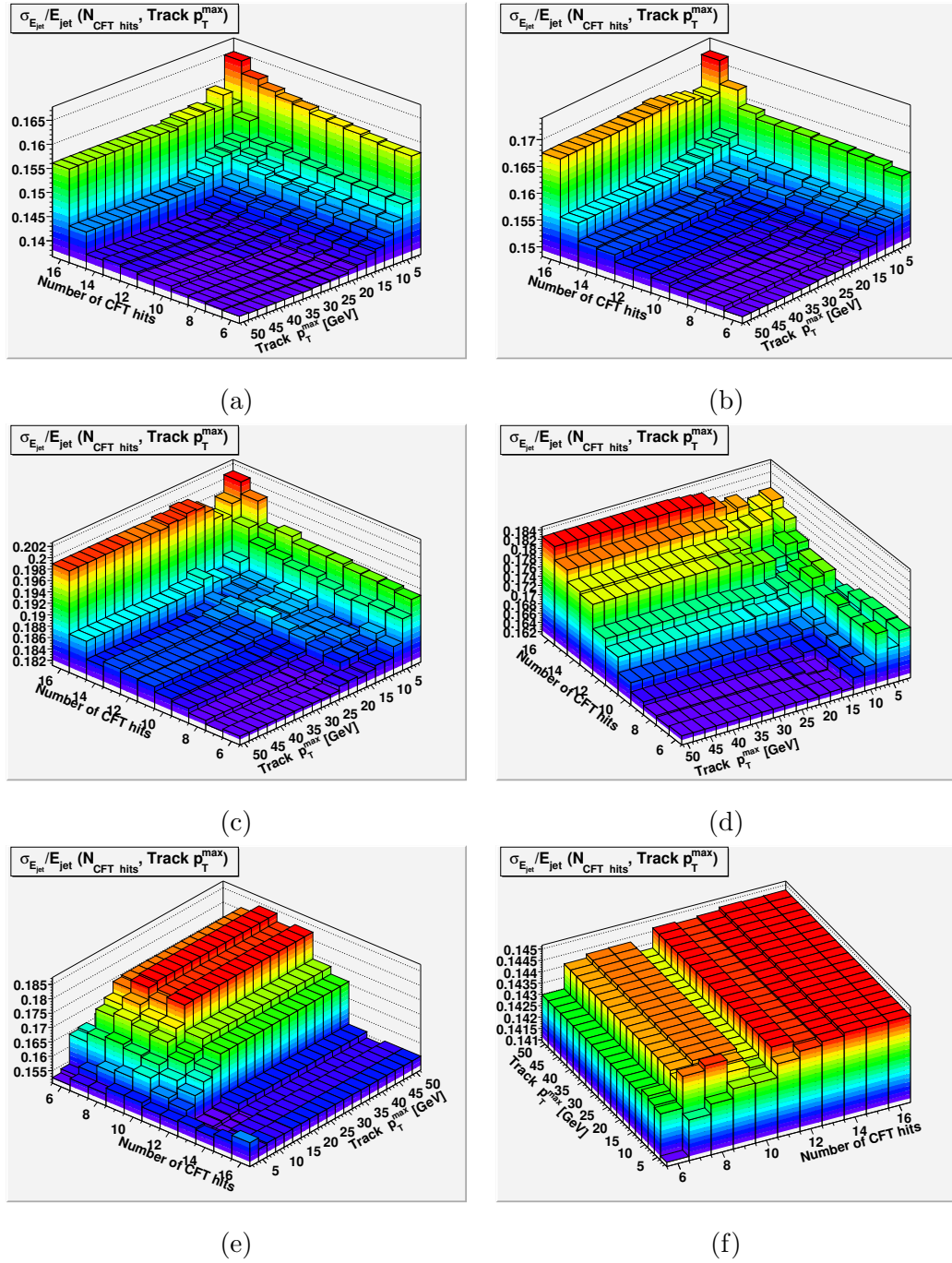
Figure 5.11: The optimization of track selection criteria (minimum number of CFT hits and maximum track p_T) in γ+jet events having $p_T^\gamma = 100$ GeV, for jets in six different regions of the calorimeter: (a)$|\eta_{\text{jet}}| < 0.4$, (b) $0.4 < |\eta_{\text{jet}}| < 0.8$, (c) $0.8 < |\eta_{\text{jet}}| < 1.2$, (d) $1.2 < |\eta_{\text{jet}}| < 1.6$, (e) $1.6 < |\eta_{\text{jet}}| < 2.0$ and (f) $2.0 < |\eta_{\text{jet}}| < 2.5$. The relative jet resolution $\sigma_{\text{E}_{\text{jet}}}/\text{E}_{\text{jet}}$ (see text), is considered to be the "Figure-of-Merit" for such optimization.
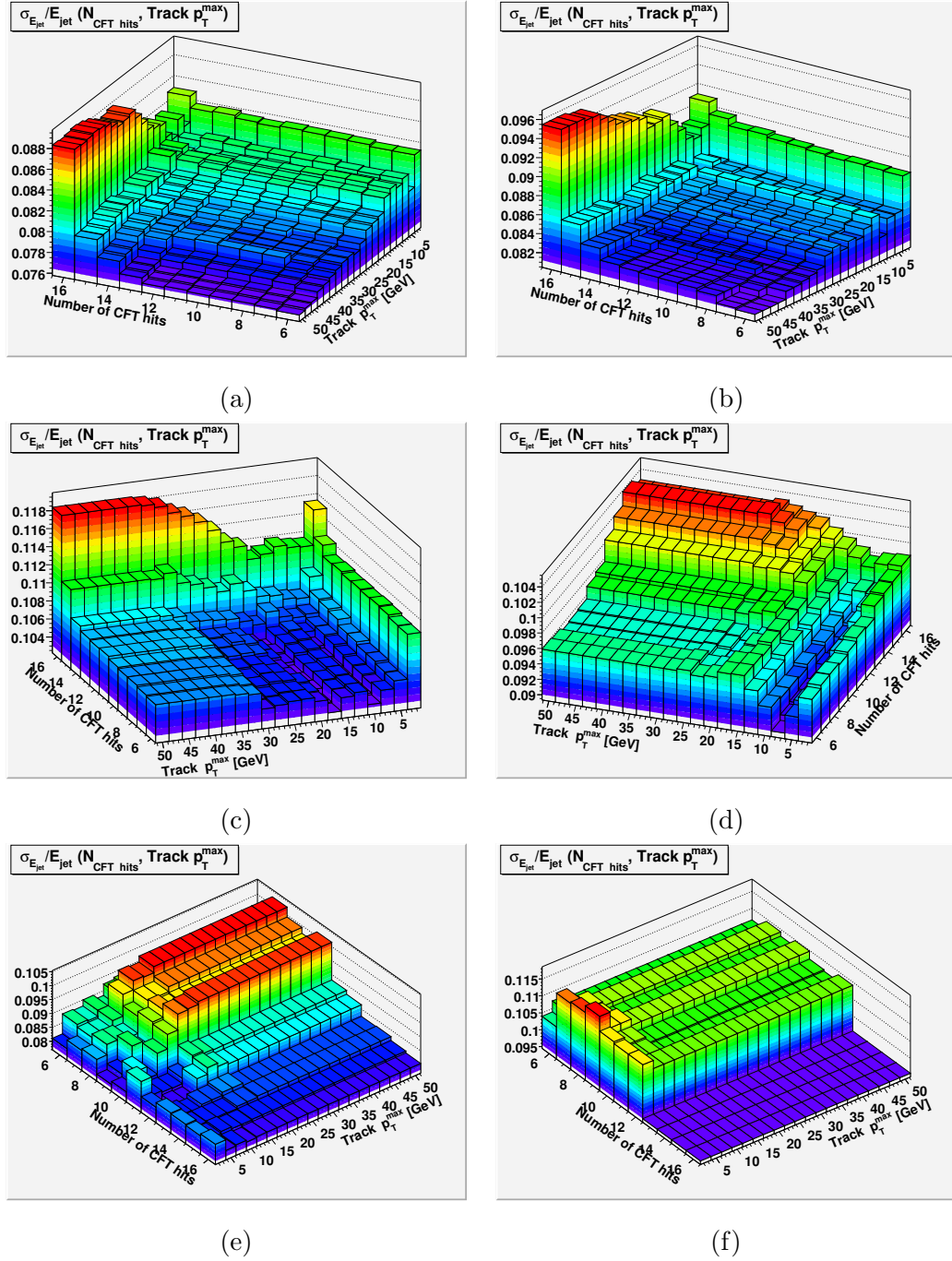
Calorimeter region	$N_{CFT\ hits}$	$p_{T,track}^{max}$ [GeV]
$|\eta| < 0.4$	12	50.
$0.4 < |\eta| < 0.8$	12	50.
$0.8 < |\eta| < 1.2$	12	50.
$1.2 < |\eta| < 1.6$	12	50.
$1.6 < |\eta| < 2.0$	6	2.5
$2.0 < |\eta| < 2.5$	6	2.5

Table 5.1: The optimized values of $N_{CFT\ hits}$ and $p_{T,track}^{max}$ (see Fig. 5.9-5.11).

$$E_{Trackcal\ jet}^{raw} = E_{cone}^{raw} + \sum_{track} p_{track}[1 - \bar{R}(p_{track}, \eta_{detector}^{jet}, \Delta R(jet,\ track))] + \sum_{muon} [p_{muon} - E_{MIP}].$$

(5.20)

It should be noted that this concept is also applied in the calorimeter-only jet energy scale, with an algorithm known as JESMU.

5.6.4 Jet Energy Scale for Trackcaljets

While the replacement of calorimeter measurements with tracking measurements does offer a truer particle level measurement, the measurement still suffers from the same deficiencies as calorimeter-only jets, except these are now primarily from inefficiencies in tracking and neutral particle contribution. We correct for these in the same manner as calorimeter only jets, and the form of the jet energy scale and its contributions remain unchanged. By adding tracking information in the jet energy scale correction more multi-variable dependent corrections can be made. The response correction is derived for different track multiplicities whereas it was inclusive previously. The addition of tracking information also begins to decouple the dependence of the jet energy measurement's dependence on the jet cone algorithm. As more tracking information is included, the only significant source of showering comes from neutral particles and therefore the dependence on the correction to this factor

is significantly reduced.

As stated, with the addition of tracking information the overall form of the correction is the same, but with the additional dependencies the correction is now given by:

$$\mathrm{E}^{\mathrm{true}}_{\mathrm{trackcal}} = \frac{\mathrm{E}^{\mathrm{raw}}_{\mathrm{Trkcal}} - \mathrm{E_O}}{\mathrm{F}_\eta(\mathrm{E_{trkcal}}) \times \mathrm{R_{CC}}(\mathrm{E_{trkcal}}, \mathrm{N_{trk}}) \times \mathrm{S}(\Delta\mathrm{R} = \inf, \mathrm{E_{trkcal}})} \qquad (5.21)$$

5.6.5 Response, Showering, Offset

Offset

Both of the components of the offset correction described in Section 5.5.1 are largely independent of the differences between the jet cone algorithm and trackcal jet algorithm and there is no demonstrable benefit from including the tracking information. Therefore, there is no need for a separate calculation of the correction, and the calorimeter only correction is used.

Response

The function and MPF method described in Section 5.5.2 remain the proper method to determine the response for trackcaljets, with the important modification of using trackcaljet energies in all calculations. We can also make one critical advance with tracking information now available. We take the central calorimeter response and bin it in track multiplicities. A statistics limited binning of 0-2,3-4,4-5,6-7,8 and above are used for the response. The new form of the response becomes:

$$R = R_{CC}(n_{trk})F_\eta \quad \text{and} \quad F_\eta = \frac{R(\eta)}{R_{CC}} \qquad (5.22)$$

The central calorimeter response for trackcaljets is given in Figures 5.12 and 5.13

Track Dependent Response

The track-dependent portion of the response is calculated only in the central region of the calorimeter ($|\eta| < 0.4$). Currently, as seen in Figures 5.14 and 5.15, the track binning is: 0-2 tracks , 3 & 4 tracks, 5 & 6 tracks, 7 & 8 tracks, >9 tracks.
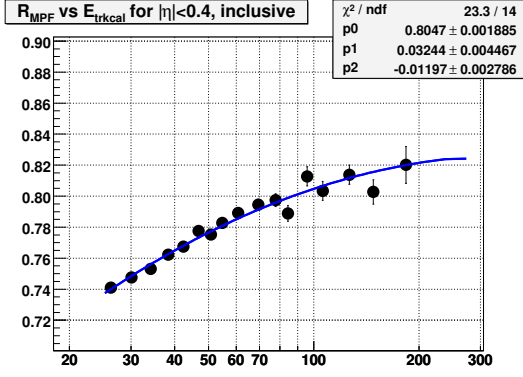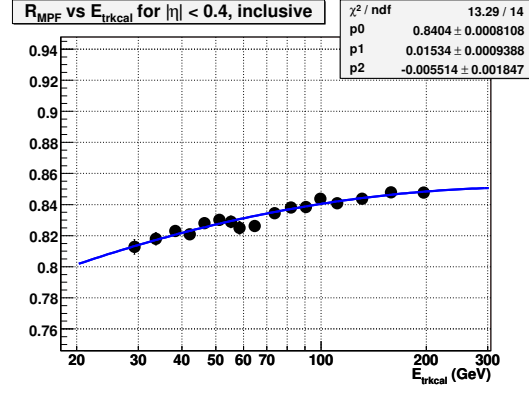
Figure 5.12: Run IIa Central Calorimeter Response inclusive of all tracks for (a) data and (b)Monte Carlo
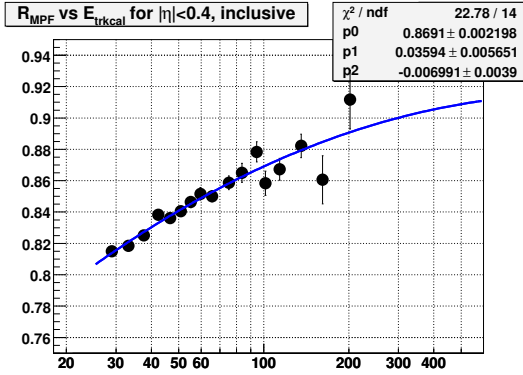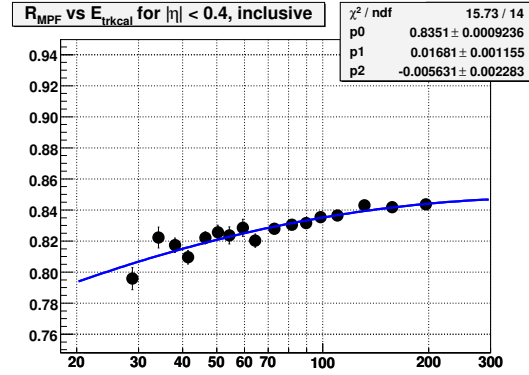
Figure 5.13: Run IIb Central Calorimeter Response inclusive of all tracks for (a) data and (b)Monte Carlo
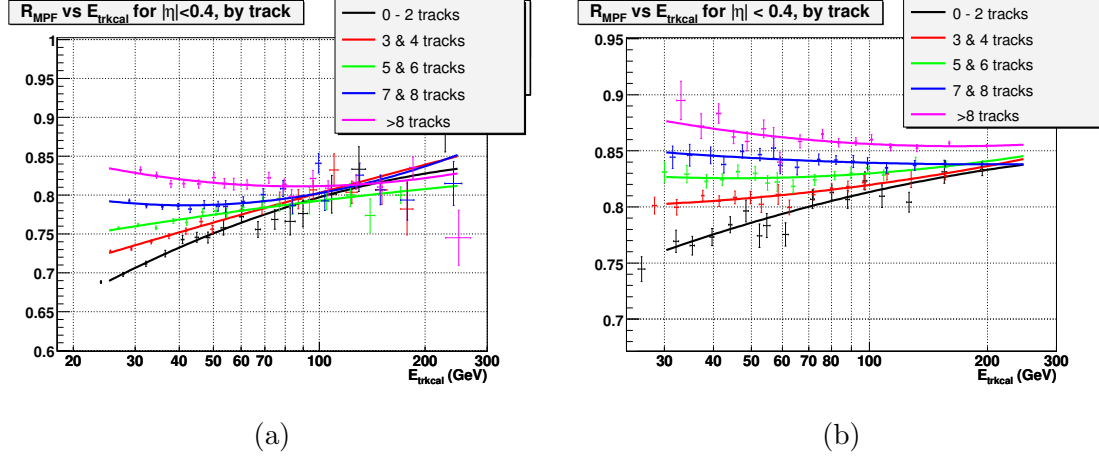
Figure 5.14: Run IIa Track Dependent Central Calorimeter Responses for (a) data and (b)Monte Carlo

These figures show two expected behaviors. First, the response approaches its high energy value as the number of tracks included in the energy calculation increases. This is due to increased precision of measurements made by the tracker that are replacing the calorimeter only measurements, leaving the inefficiencies in tracking as the dominate response correction. Also evident is that no matter how many tracks are included in the calculation of the energy measurement, after an energy of about 100 GeV, the degraded resolution of the tracker compared to the calorimeter is evident and the track-dependent central response is essentially equivalent to the track-inclusive measurement.

Eta - intercorrelated Response

The eta-dependent correction of the response accounts for the deficient response in regions outside the central calorimeter. This is achieved by making a measurement of the forward region of the calorimeter and creating a scale using the precisely measured central calorimeter response. Thus we have the form:

$$F_\eta = \frac{R(\eta)}{R_{CC}} \tag{5.23}$$

The eta dependent correction for trackcaljets is sectioned of in psuedorapidity bins of
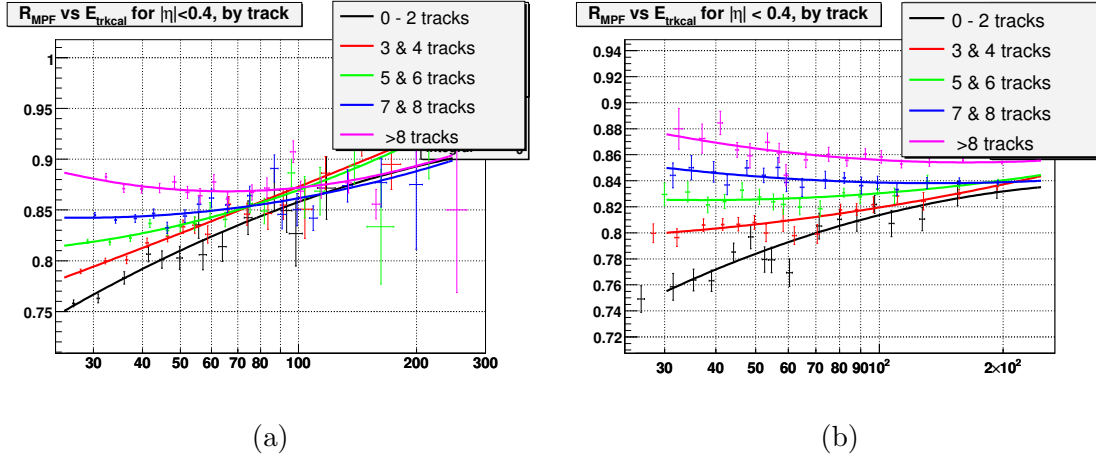
Figure 5.15: Run IIb Track Dependent Central Calorimeter Responses for (a) data and (b)Monte Carlo

0.2. For Monte Carlo the calorimeter is assumed to be symmetric and thus is binned in absolute psuedorapidity.

A sampling of the eta-dependent responses can be seen in Figure 5.16

Showering

The basic principle of the showering correction is to measure all true energy from a jet that is deposited in the calorimeter and compare this to the energy calculated by the jet algorithm. The primary source of out-of-cone showering in calorimeter-only jets is from charged particles bent in the tracker and then depositing outside the reconstruction cone.

However, in trackcaljets the momentum of the track is already accounted for in the algorithm. Therefore the showering correction is much less than the traditional correction. Another source of showering in trackcaljets is thought to come from neutral particle decay (handled in response) and pileup events (already handled in offset).

The showering correction is defined as

$$S = \frac{E_{jet}}{E_{act}} \tag{5.24}$$
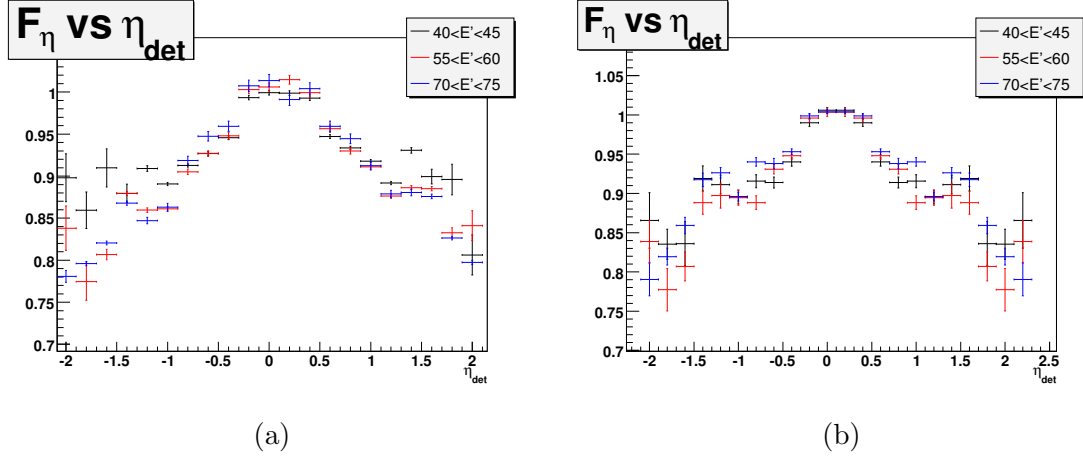
Figure 5.16: A sampling of Eta dependent responses for (a) Data and (b)Monte Carlo. As expected the reponse in the central calorimeter ($|\eta| < 0.4$ for this correction is unity.

Where

$$E_{act} = \sum_{allreco} E^{Reco} + \sum_{tracks} (1 - R(\Delta R = \inf))P_{track} \tag{5.25}$$

and

$$E_{RECO} = E_{cell} \frac{E_{CAEP}}{\sum_i E_{CAEP,i}} \tag{5.26}$$

$$E_{CAEP} = \sum_{MCPart}^{j} \sum_{cells}^{i} (E_{CAEP_j})_i \tag{5.27}$$

This formalism is nearly the same as presented in 5.5.3, with important modification to Equation 5.25. This equation is now consistent with the energy definition for trackcaljets.

To measure the average true response correction for the track we follow the same procedure as in determining the response for the raw trackcal jet energy. Except in this case, we don't just use the energy deposited inside the jet cone, we use all the energy deposited in the calorimeter by that particular particle.

In this case the charged pion response has been extended to include energy from the entire calorimeter and the "caljet" energy is the more traditional energy taken by the entire detector. The Showering correction is shown in Figure 5.17

Showering correction in 0.0 < |Eta| < 0.4

$p_0 + p_1 \log(x/700) + p_2(\log(x/700))^2$

$p_0 = 0.99218 \pm 0.00184$

$p_1 = -0.00245 \pm 0.00169$

$p_2 = -0.00034 \pm 0.00036$

$\chi^2/Ndf = 0.7167$

(a)

Showering correction in 0.4 < |Eta| < 0.8

$p_0 + p_1 \log(x/700) + p_2(\log(x/700))^2$

$p_0 = 0.98486 \pm 0.00321$

$p_1 = 0.00084 \pm 0.00276$

$p_2 = 0.00045 \pm 0.00057$

$\chi^2/Ndf = 0.6280$

(b)

Showering correction in 0.8 < |Eta| < 1.2

$p_0 + p_1 \log(x/700) + p_2(\log(x/700))^2$

$p_0 = 0.97922 \pm 0.00625$

$p_1 = 0.00441 \pm 0.00580$

$p_2 = 0.00236 \pm 0.00129$

$\chi^2/Ndf = 0.9072$

(c)

Showering correction in 1.2 < |Eta| < 1.6

$p_0 + p_1 \log(x/700) + p_2(\log(x/700))^2$

$p_0 = 0.99273 \pm 0.00908$

$p_1 = 0.02155 \pm 0.00855$

$p_2 = 0.00514 \pm 0.00191$

$\chi^2/Ndf = 1.6042$

(d)

Figure 5.17: Out-of-cone Showering correction for (a) $|\eta| < 0.4$ (b)$0.4 < |\eta| < 0.8$ (c)$0.8 < |\eta| < 1.2$ (d)$1.2 < |\eta| < 1.6$

5.6.6   Resolution

Using the calorimeter jet energy reconstruction algorithm, the energy resolution can be written with three main components as:

$$\frac{\sigma(\mathrm{E})}{\mathrm{E}} = \frac{\mathrm{a}}{\sqrt{\mathrm{E}}} + \frac{\mathrm{b}}{\mathrm{E}} + \mathrm{c}, \tag{5.28}$$

These three components are:

- Stochastic response ($\mathrm{a}/\sqrt{\mathrm{E}}$): This term accounts sampling and for intrinsic fluctuations in the development of the jet shower. This is the dominate term in the resolution.

- Electronic noise (b/E): This term accounts for detector contribution as well as pile-up inside the detector. It is the limiting factor for the calorimeter performance at low energy.

- Constant term (c): This constant component is due to the calibration errors, non-uniformities and non-linearities of the calorimeter response, dead material in front of the calorimeter, magnetic field etc. This component sets the limit for the performance at very high energy.

We use two different methods for calculating the jet energy resolution.

Gamma + jet Resolution

As explained earlier, a γ + jet event event is an ideal environment to compare the energy of the jet to a well measured object. Therefore, we can again use this environment to explore how well our corrections are being made. We use the variable:

$$E' = p_{T\gamma}^{meas} \cosh(\eta_{jet}) \tag{5.29}$$

$p_{T\gamma}^{meas}$ is the transverse momenta of the photon and $\cosh(\eta_{jet})$ is the psuedo rapidity with respect to the primary vertex. Both of these quantities are measured more precisely

than the jet energy and are therefore more correlated to the true particle level energy. To examine the jet energy resolution we take the quotient of the trackcaljet energy and E':

$$R = \frac{E_{trkcal}}{E'} \tag{5.30}$$

The deviation and mean of the resulting distribution are used as the measure of the jet energy resolution. Figures 5.18, 5.19, and 5.20 compare the resolution of the trackcaljets and caljets in different pseudorapidities as a function of E'. In each epoch (p17 and p20) and for Data and Monte Carlo there is a 5-10% improvement in jet energy resolution using trackcaljets.
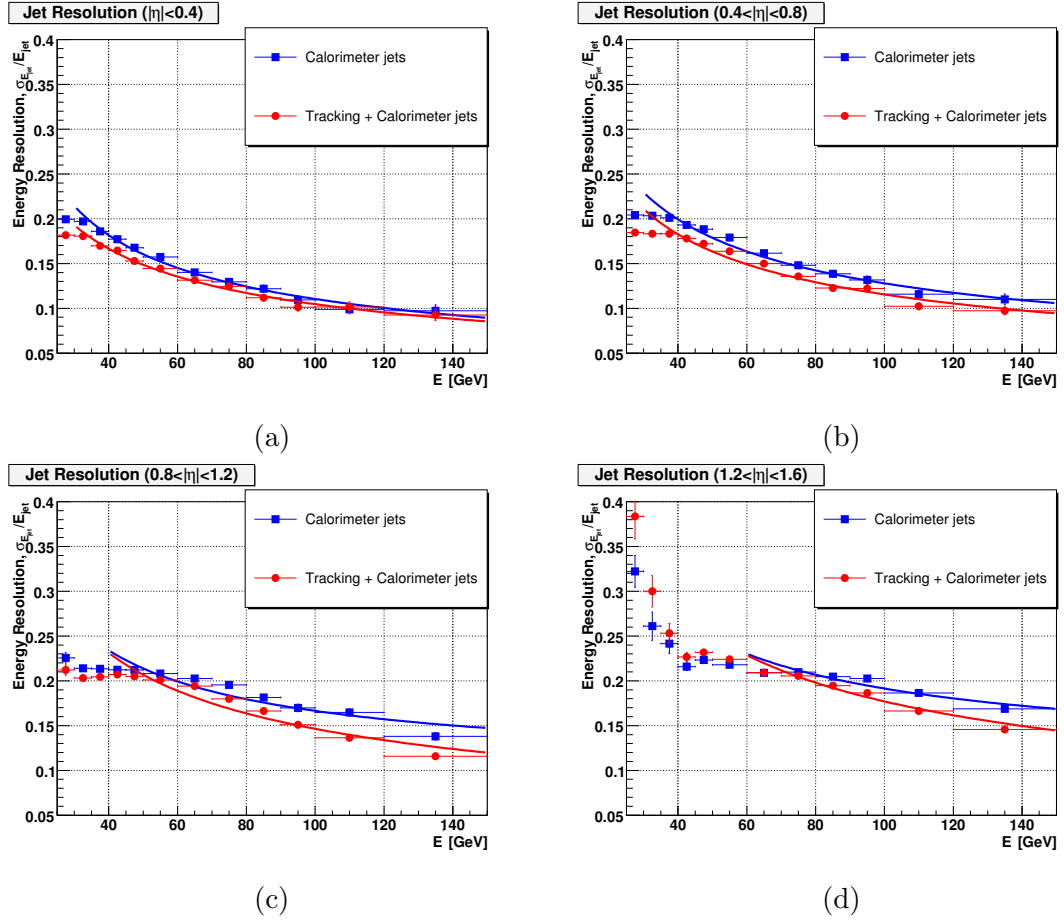
Figure 5.18: $\gamma + jet$ Resolution for Run IIa data in (a) $|\eta| < 0.4$ (b)$0.4 < |\eta| < 0.8$ (c)$0.8 < |\eta| < 1.2$ (d)$1.2 < |\eta| < 1.6$

(a)

(b)

(c)

(d)
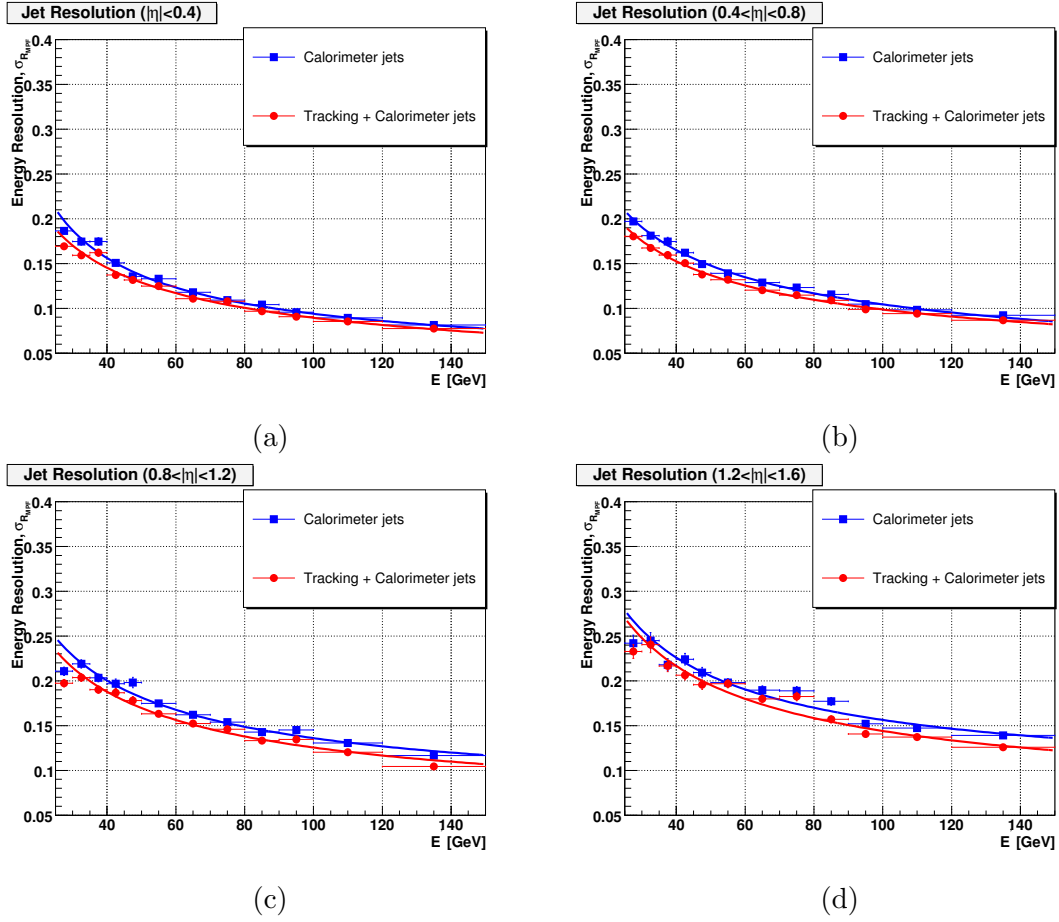
Figure 5.19: $\gamma + jet$ Resolution for Run IIa Monte Carlo in (a) $|\eta| < 0.4$ (b)$0.4 < |\eta| < 0.8$ (c)$0.8 < |\eta| < 1.2$ (d)$1.2 < |\eta| < 1.6$
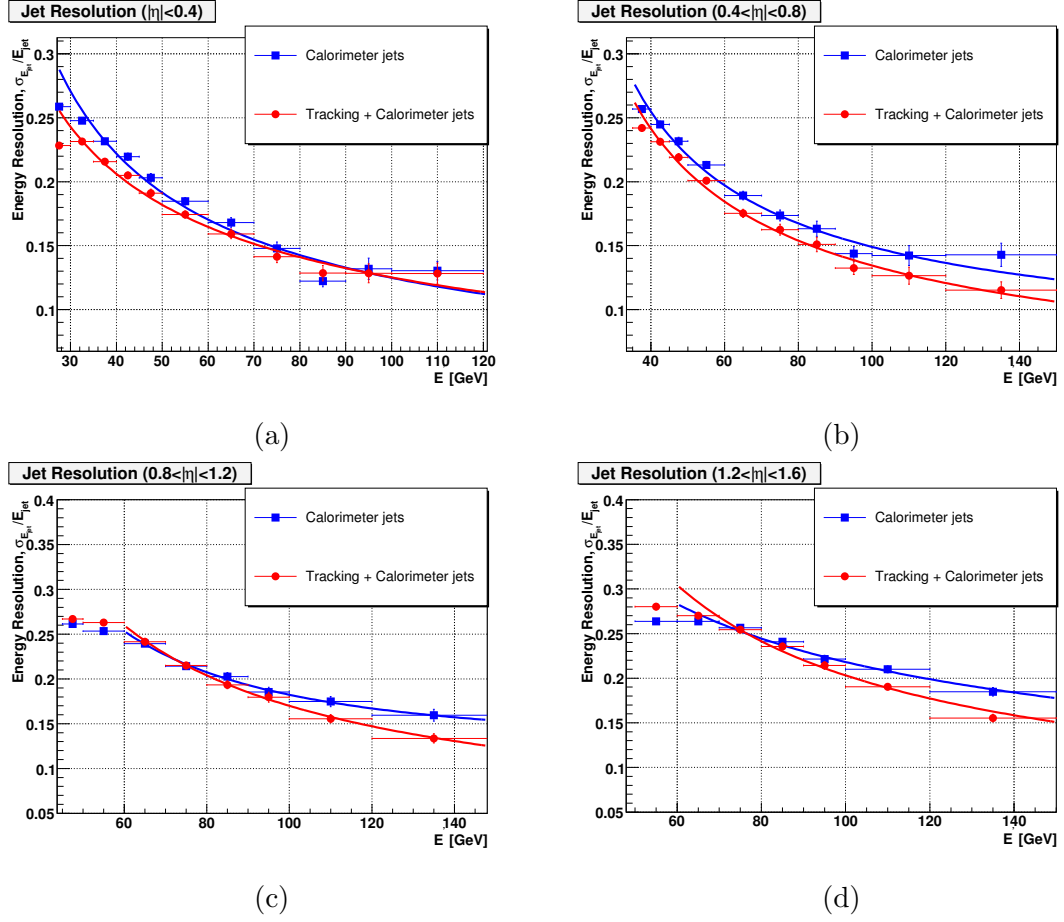
Figure 5.20: $\gamma + jet$ Resolution for Run IIb Data in (a) $|\eta| < 0.4$ (b)$0.4 < |\eta| < 0.8$ (c)$0.8 < |\eta| < 1.2$ (d)$1.2 < |\eta| < 1.6$

Dijet Resolution

The jet energy resolution can also be measured in dijet events. In a typical dijet event, the jets are back-to-back in azimuthal angle and thus we can define an asymmetry variable as

$$\mathcal{A} = \frac{p_{T,1} - p_{T,2}}{p_{T,1} + p_{T,2}} \tag{5.31}$$

Where the ordering of the jets is in increasing rapiditiy in order to observe any possible residual jet energy scale shifts in the forward regions of the calorimeter when compared to the central region. [22]

(a)

(b)

(c)
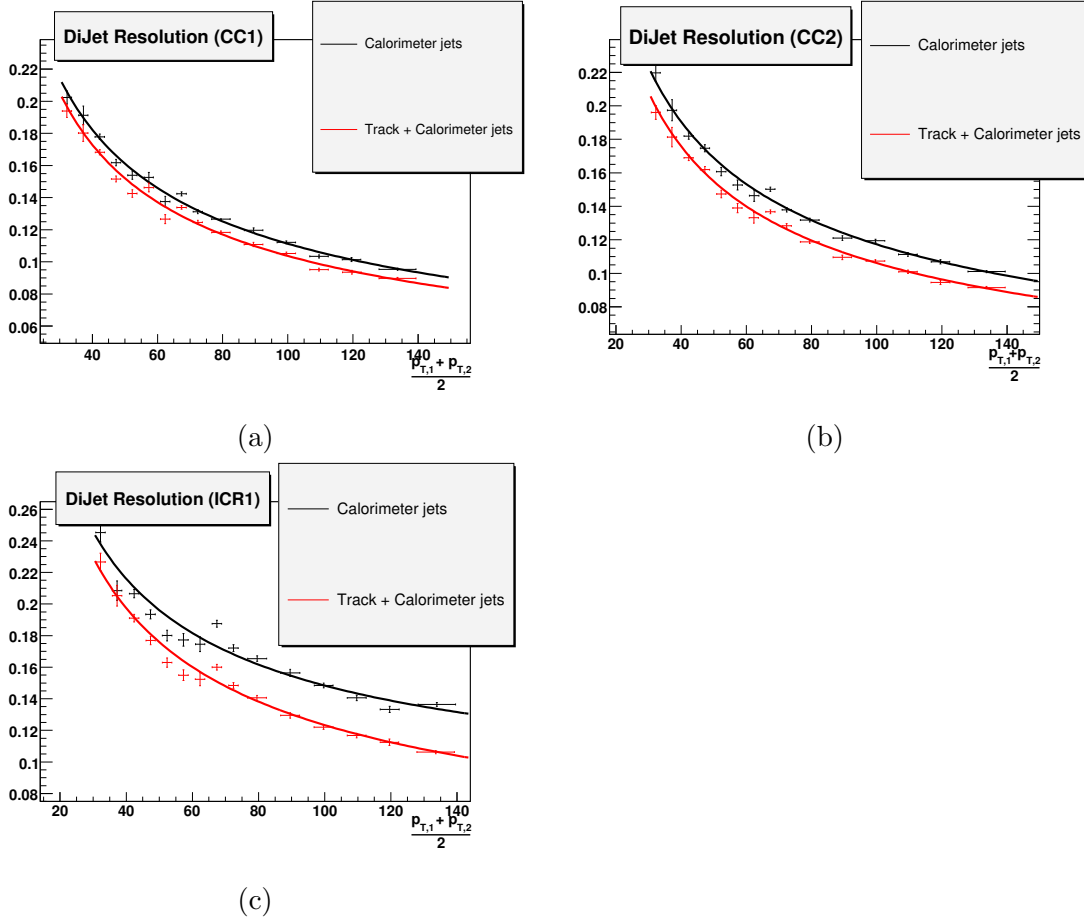
Figure 5.21: DiJet Resolution for Run IIa data for (a) $|\eta| < 0.4$ (b)$0.4 < |\eta| < 0.8$ (c)$0.8 < |\eta| < 1.2$

It can be shown that the resolution are given by:

$$\frac{\sigma(E)}{E} = \sqrt{2}\sigma_{\mathcal{A}} \tag{5.32}$$

Here also we measured the jet resolution separately for each region of the calorimeter. Figures 5.21 and 5.22 again show a marked improvement in jet energy resolution.
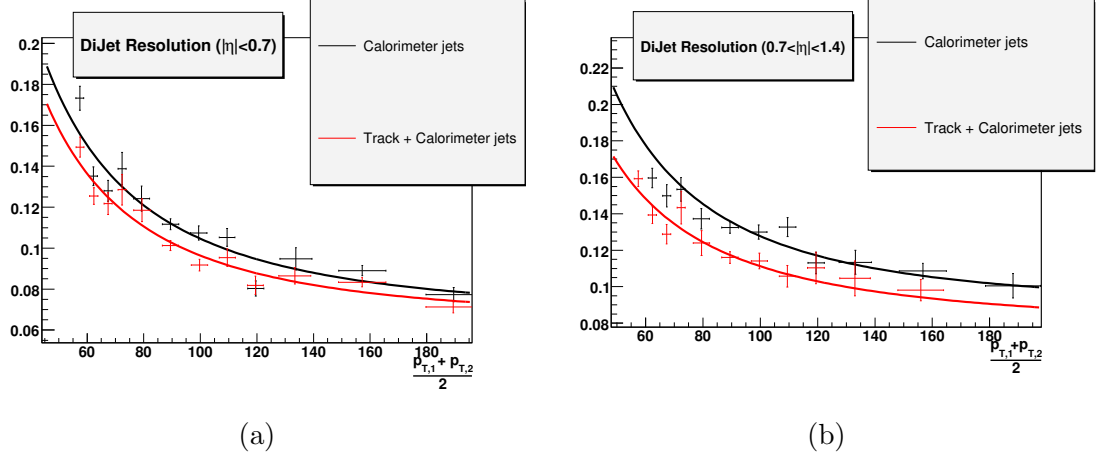
Figure 5.22: DiJet Resolution for Run IIb data for (a) $|\eta| < 0.4$ (b)$0.4 < |\eta| < 0.8$

5.6.7 Closure

It is expected that, on average, the energy derived from calorimeter only jets is a close approximation the true jet energy. As a closure test we compare the average ratio of the calorimeter only jet energy and the trackcaljet energy. Due to the jet reconstruction threshold of 6 GeV in raw energy we see a discrepancy in low energy trackcal jets. We also noticed a discrepancy in high energy jets, which is to be expected from the degraded resolution of the tracker in the high jet energy regime. We restrict the use of the trackcaljet energy scale to certain transverse energy ranges. The restrictions to apply the trackcaljet energy scale, as opposed to the traditional energy scale are:

$$15 < E < 150 \text{ for } |\eta| < 0.4$$
$$15 < E < 150 \text{ for } 0.4 < |\eta| < 0.8$$
$$20 < E < 120 \text{ for } 0.8 < |\eta| < 1.2$$
$$40 < E < 110 \text{ for } 1.2 < |\eta| < 1.6$$

The resultant ratios after these cuts can be seen in Figure 5.23

(a)

(b)

(c)

(d)
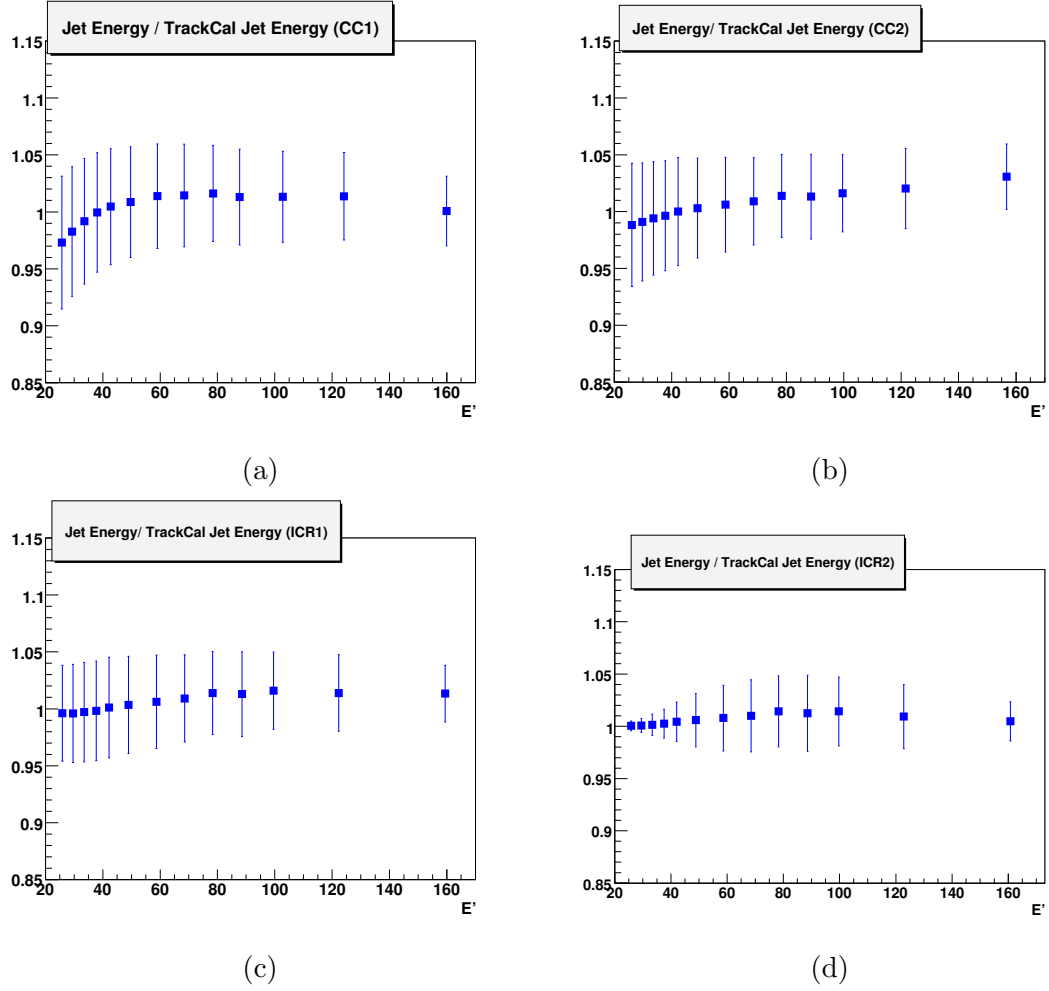
Figure 5.23: Average ratio of calorimeter jet energy to trackcaljet energy (a) $|\eta| < 0.4$ (b)$0.4 < |\eta| < 0.8$ (c)$0.8 < |\eta| < 1.2$ (d)$1.2 < |\eta| < 1.6$

Chapter 6

HIGGS BOSON SEARCH

As shown in Chapter 2, we can theoretically infer many traits of the Higgs boson, the most important being the production cross-section and branching fractions. The standard model Higgs boson naturally couples to the most massive kinematically available particle. In the energy regime most likely to produce the standard model Higgs this leads to a natural division in production mechanisms when the mass of the higgs is roughly $2M_W$ in the rest mass frame. With a mass lower than $2M_W$, the Higgs is most likely to decay to a pair of b-quarks. However, the W^+W^- decay mode becomes available before $2M_W$ due to the boosting of the Higgs. We optimize searches according to the high branching fraction in each regime from the division at $m_H = 135$ GeV. Figure 6.1 shows the production cross-section $\times$ branching ratio for these important processes. For this search we focus on $m_H < 135$ GeV and thus optimize about the $H \to b\bar{b}$ final states.

The production cross-section of $gg \to h$ is nearly an order of magnitude higher than any other. However, the $H \to b\bar{b}$ final state is overwhelmed by the various background QCD interactions. Thus, we use other production modes, like the so-called associated production channels, or *Higgstrahlung*. Knowing we will use associated production with vector bosons, and knowledge of the branching fractions of the vector bosons, there come three natural search channels: di-lepton, lepton $+ \not{E}_T$, and pure $\not{E}_T$, with missing $\not{E}_T$ due to neutrinos.

Each channel has it's own advantages. The dilepton channel, coming from ZH production with $Z \to \ell\ell$, has the lowest production cross-section and branching fraction. However, the two leptons and the absence of neutrino allow for significant suppression of the QCD background, which is mainly hadronic, and allow for complete reconstruction of the final state including the dilepton and dijet invariant mass. Also, the s- and t- channel contributions [23]can be distinguished. The lepton $+ \not{E}_T$ channel, from associated W production, benefits from the larger production cross-section and branching fractions as well as a lepton
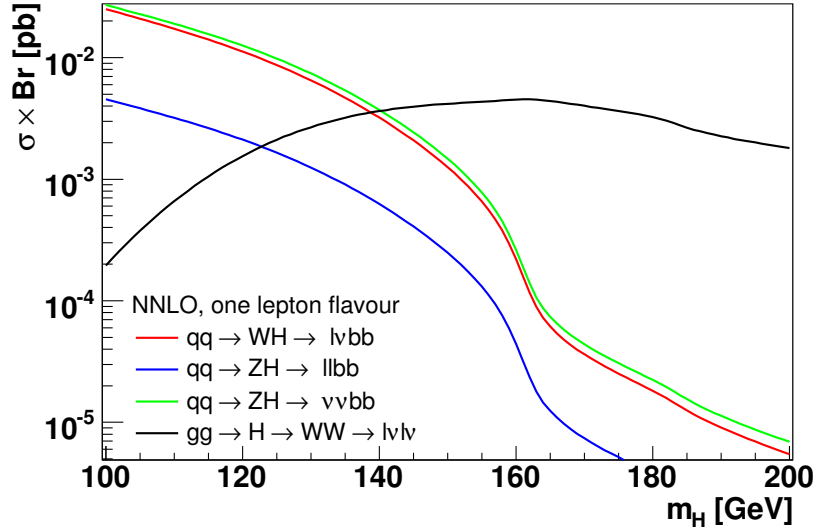
Figure 6.1: The NNLO productions Cross-sections times branching fractions for the Standard Model Higgs boson. Given here are for boson branching fractions for a single lepton flavor. [25]

to suppress QCD. Further exploitation of the W kinematics, such as the W boson transverse mass, leads to better background suppression [24]. The final channel, $\not{E}_T + b\bar{b}$, is normally attributed to the $ZH \to \nu\bar{\nu}b\bar{b}$ production, which benefits from a branching fraction three times the $\ell\ell$ branching fraction, but a cross-section half that of associated W production. However, as will be shown, the $WH \to \ell^{\pm}\nu b\bar{b}$, benefiting as above, also contributes a roughly equal amount to the final signal yield. Additionally, there is no dedicated search from associated production in tau final states, so these final states are included in this search. However, without a lepton, the multijet background, arising from QCD and instrumental effects, is much more significant. Still, the $\not{E}_T + $ bb final states is among the most promising for observing a low-mass Higgs boson at the Fermilab Tevatron [26].

Of all the channels presented above, the $\not{E}_T$ is inundated with the largest multijet background. Further, any process which creates a heavy quark in the final state contributes to background. In the initial stages of the analysis, these are predominately $W \to cs$ and $Z \to b\bar{b}$. In the final stages of the analysis, the predominate background is single- and double-top production. A additional contribution to background processes are ones that

directly mimic the signal, the are the diboson processes, WW, WZ, ZZ, all of which contain the exact decay modes of our signal process.

In February 2010, the DØ collaboration published a search for this process based on 5.2 fb^{-1} of data [27]. In what follows, an extension of this search, performed by the author in collaboration with Krisztian Peters, Gabriel Facini, Abhinav Dubey, Murilo Rangel, and Jean-Francois Grivaz, to 6.4 fb^{-1} is presented.

6.1   Preselection and Strategy

A thorough and efficient analysis must account for the limitations of available resources in the formulation of a strategy o maximize the use of available data. This is includes the ability to rapidy absorb new data and improved methods in the face of limited computing resources. To this end we have devised a strategy such that the most time intensive and least sensitive to improved methods are performed at the beginning of the analysis, and performed the least. Successive stages will take less time to perform and optimized more frequently, and will be better suited to include improved methods. In the first stage, we make use of very general criteria that minimize the overwhelming multijet background and retain a large number of signal-like event. This stage has the loosest cuts and retains the most information from events, so is done very rarely, so that successive stages can make use of this smaller dataset.

In a second stage, we place stricter criteria to further reduce background, and we also define four distinct samples with the following purposes:

- a signal sample (Sec. 6.8) used to search for a Higgs-boson. Here, further topological criteria are applied to reduce the multijet background, among which a tighter cut on the $\not{E}_T$. In addition, a veto on isolated leptons is applied to reduce the background from $W \rightarrow \ell\nu$+jets;

- an electroweak control sample (Sec. 6.6), enriched in $(W \rightarrow \mu\nu)$+jets events, where the jet system has a topology similar to that of the signal sample, and used to validate the SM background simulation. The selection is similar to the one used for the signal sample, except that the veto on isolated muons is reversed;

- a "MJ-model" sample, dominated by multijet events, and used to model the multijet background in the signal sample. This sample is selected in the same way as the signal sample, except for one defining topological selection criterion that is reversed;

- a large multijet control sample (Sec. 6.7), used to validate this modeling procedure. Here, the topological selection criteria are sufficiently relaxed to lead to a sample largely dominated by multijet events.

Once these selection criteria have been applied, a "multijet decision tree" (MJ-DT) is used to further discriminate against the multijet background (Sec. 7.2). At this point we use b-tagging to define two orthogonal samples and further reduce backgrounds. Finally another decision tree is used to discriminate against standard model backgrounds and is used as the final discriminate to in the search.

The first stage of preselection is made in the data acquisition process and involves making decision based on large scale topography of events as well as the formation of primitive objects (jets, vertices, etc.). Eventually, we use a set of criteria from these decision, known as triggering, that definite a consisting of the the logical ORing of three jets+$\not{E}_T$ triggers. The calibration of the trigger response was derived with $Z \rightarrow \mu\mu$+jets events which, when considering the MIP nature of Muons in the calorimeter, have the same jet topology as our signal selection. Both the description of the trigger and the trigger simulation can be found in detail in [28].

In addition to our trigger requirements, we have basic data quality requirements. For instance, during collisions, the relevant detector systems should have no major problems, such as power not being in some sector of the detector, or to high of a bias voltage which might lead to a mismeasured $\not{E}_T$. Also, the event must be properly reconstructed in the data acquisition system (DAQ). After these are applied, we require the following for our preselection. The primary vertex (PV) must be reconstructed within the acceptance of the silicon vertex detector ($|z_{\mathrm{PV}}| < 40$ cm), and at least three charged particle tracks have to originate from that vertex (known as vertex confirmation). Only jets with $p_T > 15$ GeV within $|\eta| < 3.2$ are considered in the analysis, and are ordered in decreasing p_T. There

must be two or more jets in the event, of which at least one must be considered taggable. The missing transverse energy is required to be larger than 30 GeV. Finally, there must be no bad jets in the event with $p_T > 15$ GeV, not considering those for which the only bad-jet criterion is EM frac. > 0.95 (See Sec. 6.4.1). The numbers of events after each cut for the MC signal samples and the observed data events can be seen in Table 6.1.

Selection	Data			$ZH \rightarrow \nu\overline{\nu}b\overline{b}$ MC (115 GeV)			$WH \rightarrow \ell^{\pm}\nu b\overline{b}$ MC (115 GeV)		
	Events	Rel.(%)	Abs.(%)	Events	Rel.(%)	Abs.(%)	Events	Rel.(%)	Abs.(%)
New Phenomena skim[(*)]	162278545	100.00	100.00	874354	100.00	100.00	653001	100.00	100.00
Bad runs & LBNs	138585867	85.40	85.40	872565	99.80	99.80	650345	99.59	99.59
Event quality	127898384	92.29	78.81	845271	96.87	96.67	629738	96.83	96.44
First PVz $\leq$ 40cm	115777258	90.52	71.34	755404	89.37	86.40	562793	89.37	86.19
First PV has $\geq$ 3 tracks	112020947	96.76	69.03	743062	98.37	84.98	555776	98.75	85.11
Trigger	29244092	26.11	18.02	–	–	–	–	–	–
$N_{\mathrm{jets}} \geq 2$[(**)]	25472190	87.10	15.70	612847	82.48	70.09	450446	81.05	68.98
Trigger Simulation	–	–	–	238225	38.87	27.25	174570	38.75	26.73
$\not{E}_T \geq 30$ GeV	14066274	55.22	8.67	229839	96.48	26.29	166935	95.63	25.56
Two Candidate Jets[(***)]	6359015	45.20	3.92	195269	84.95	22.33	136452	81.74	20.90

Table 6.1: Cut-flow for p20 preselection. (Generated number of MC events for the signal, scale factors not applied.)

[(*)] *This skim looks for* $\not{H}_T > 20$ *and good jet clusters*

[(**)] *Good jets with* $p_T > 15$ *GeV and* $|\eta| < 3.2$

[(***)] *At least 2 taggable jets or only one taggable jet and at least one good jet with* $p_T > 20 GeV$ *and* $|\eta| < 2.5$

6.2 Data

The Tevatron has had two major running stage separated by major upgrades in detectors and the accelerator. The first stage ran from August 1992 to February 1996. It was designated Run I and delivered 180 pb^{-1} at $\sqrt{s} = 1.8$ GeV. Run I highlights include the first $p\overline{p}$ collisions and the discovery of the top quark [29], the prediction for this received the Nobel prize in 2008. This analysis will only use data from Run II, which commenced in March 2001 with higher beam energy of $\sqrt{s} = 1.96 GeV$. and the previously mention detector upgrades. The first data-taking epoch of RunII ran until February 2006, and is known as Run IIa. From June 2006 until the present consists of Run IIb. The integrated luminosities for Run II are given in Table 6.2. As described earlier, in each Run II epoch we have subdivided the analysis sample into two orthogonal samples, a "one tag" and a "two tag." Described here are the details of the Run IIb two tag analysis which incorporates the most data and a more sophisticated decision tree. The remaining three samples are similar in structure to this analysis, but use the methods described in [27]. The differences and all control plots are for these analyses are contained in the appendices. The final result, however, will contain the information from all four samples.

Epoch	Delivered	Recorded	Good
Run IIa	1156.4	1069.5	945.3
Total Run IIb	6401.2	6058.1	5498.9

Table 6.2: Run II luminosity

6.3   MC Sample and Corrections

For Run II we use the following Monte Carlo samples (see tables 6.3–6.9). For all samples, the PYTHIA version v6.409 [30] with "DØ tune A" and the CTEQ6L1 [31] LO PDF set are used.

All W/Z+jets and $t\bar{t}$ processes were generated with ALPGEN v2.11 [32] interfaced with PYTHIA for the simulation of initial and final state radiation, and of jet hadronization. In the ALPGEN stage, the generated partons are required to have $p_T > 8$ GeV and a separation $\Delta R > 0.4$. The scale is set to the sum in quadrature of the mass and p_T of the boson in each event. After PYTHIA showering, any particle jet with $p_T > 8$ GeV is required to match an ALPGEN parton [33], except in the highest parton multiplicity (inclusive) sample, where additional (unmatched) particle jets are allowed. The inclusive di-boson MC samples were produced with PYTHIA. The single top samples were produced with COMPHEP [34], interfaced with PYTHIA.

The WH and ZH signal samples were simulated with PYTHIA.

Feynman diagrams for the major standard model processes are given in Figures 6.2-6.4
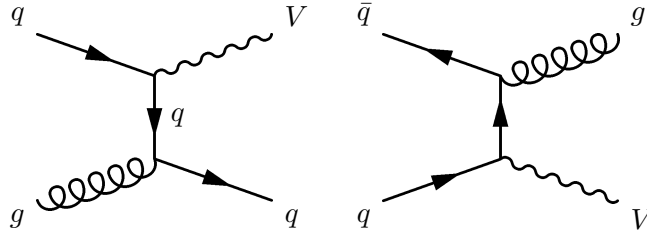
Figure 6.2: Two channels for background processes with a vector boson

6.3.1   Additional MC Information

Events that are simulated with PYTHIA are done so and calculated with a leading order (LO) cross-section calculation. ALPGEN generated events are calculated at Leading Logarithm order (LL). State-of-the-art calculations have provided these cross-sections at next-to-leading order (NLO) or one generation further, NNLO. A ratio is calculated that

Mode	Run IIb
	σ (pb)$\times$ BR
$ZH \to \nu\nu bb(m_h = 100)$	0.027280
$ZH \to llbb(m_h = 100)$	0.013773
$ZH \to \nu\nu cc(m_h = 100)$	0.001203
$ZH \to \nu\nu\tau\tau(m_h = 100)$	0.002690
$ZH \to \nu\nu bb(m_h = 105)$	0.022927
$ZH \to llbb(m_h = 105)$	0.011575
$ZH \to \nu\nu cc(m_h = 105)$	0.001011
$ZH \to \nu\nu\tau\tau(m_h = 105)$	0.002282
$ZH \to \nu\nu bb(m_h = 110)$	0.019081
$ZH \to llbb(m_h = 110)$	0.009634
$ZH \to \nu\nu cc(m_h = 110)$	0.000840
$ZH \to \nu\nu\tau\tau(m_h = 110)$	0.001916
$ZH \to \nu\nu bb(m_h = 115)$	0.015671
$ZH \to llbb(m_h = 115)$	0.007912
$ZH \to \nu\nu cc(m_h = 115)$	0.000690
$ZH \to \nu\nu\tau\tau(m_h = 115)$	0.001587
$ZH \to \nu\nu bb(m_h = 120)$	0.012553
$ZH \to llbb(m_h = 120)$	0.006338
$ZH \to \nu\nu cc(m_h = 120)$	0.000553
$ZH \to \nu\nu\tau\tau(m_h = 120)$	0.001282
$ZH \to \nu\nu bb(m_h = 125)$	0.009790
$ZH \to llbb(m_h = 125)$	0.004943
$ZH \to \nu\nu cc(m_h = 125)$	0.000431
$ZH \to \nu\nu\tau\tau(m_h = 125)$	0.001007

Table 6.3: Signal ZH MC samples with cross sections. The number of events is calculated after applying the DQ cuts and duplicate events removal.

Mode	Run IIb σ (pb)$\times$ BR
$ZH \rightarrow \nu\nu bb(m_h = 130)$	0.007360
$ZH \rightarrow llbb(m_h = 130)$	0.003716
$ZH \rightarrow \nu\nu cc(m_h = 130)$	0.000324
$ZH \rightarrow \nu\nu\tau\tau(m_h = 130)$	0.000763
$ZH \rightarrow \nu\nu bb(m_h = 135)$	0.005311
$ZH \rightarrow llbb(m_h = 135)$	0.002681
$ZH \rightarrow \nu\nu cc(m_h = 135)$	0.000234
$ZH \rightarrow \nu\nu\tau\tau(m_h = 135)$	0.000554
$ZH \rightarrow \nu\nu bb(m_h = 140)$	0.003654
$ZH \rightarrow llbb(m_h = 140)$	0.001845
$ZH \rightarrow \nu\nu cc(m_h = 140)$	0.000161
$ZH \rightarrow \nu\nu\tau\tau(m_h = 140)$	0.000384
$ZH \rightarrow \nu\nu bb(m_h = 145)$	0.002381
$ZH \rightarrow llbb(m_h = 145)$	0.001202
$ZH \rightarrow \nu\nu cc(m_h = 145)$	0.000105
$ZH \rightarrow \nu\nu\tau\tau(m_h = 145)$	0.000252
$ZH \rightarrow \nu\nu bb(m_h = 150)$	0.001434
$ZH \rightarrow llbb(m_h = 150)$	0.000724
$ZH \rightarrow \nu\nu cc(m_h = 150)$	0.000063
$ZH \rightarrow \nu\nu\tau\tau(m_h = 150)$	0.000153

Table 6.4: Signal ZH MC samples with cross sections. The number of events is calculated after applying the DQ cuts and duplicate events removal.

Mode	Run IIb
	σ (pb)$\times$ BR
$WH \rightarrow l\nu bb(m_h = 100)$	0.075973
$WH \rightarrow l\nu cc(m_h = 100)$	0.003350
$WH \rightarrow l\nu\tau\tau(m_h = 100)$	0.007490
$WH \rightarrow l\nu bb(m_h = 105)$	0.063234
$WH \rightarrow l\nu cc(m_h = 105)$	0.002787
$WH \rightarrow l\nu\tau\tau(m_h = 105)$	0.006294
$WH \rightarrow l\nu bb(m_h = 110)$	0.052134
$WH \rightarrow l\nu cc(m_h = 110)$	0.002296
$WH \rightarrow l\nu\tau\tau(m_h = 110)$	0.005253
$WH \rightarrow l\nu bb(m_h = 115)$	0.042404
$WH \rightarrow l\nu cc(m_h = 115)$	0.001868
$WH \rightarrow l\nu\tau\tau(m_h = 115)$	0.004295
$WH \rightarrow l\nu bb(m_h = 120)$	0.033693
$WH \rightarrow l\nu cc(m_h = 120)$	0.001483
$WH \rightarrow l\nu\tau\tau(m_h = 120)$	0.003440
$WH \rightarrow l\nu bb(m_h = 125)$	0.026036
$WH \rightarrow l\nu cc(m_h = 125)$	0.001146
$WH \rightarrow l\nu\tau\tau(m_h = 125)$	0.002679

Table 6.5: Signal WH MC samples with cross sections. The number of events is calculated after applying the DQ cuts and duplicate events removal.

Mode	Run IIb
	σ (pb)$\times$ BR
$WH \to l\nu bb(m_h = 130)$	0.019385
$WH \to l\nu cc(m_h = 130)$	0.000853
$WH \to l\nu\tau\tau(m_h = 130)$	0.002009
$WH \to l\nu bb(m_h = 135)$	0.013861
$WH \to l\nu cc(m_h = 135)$	0.000610
$WH \to l\nu\tau\tau(m_h = 135)$	0.001447
$WH \to l\nu bb(m_h = 140)$	0.009452
$WH \to l\nu cc(m_h = 140)$	0.000416
$WH \to l\nu\tau\tau(m_h = 140)$	0.000993
$WH \to l\nu bb(m_h = 145)$	0.006100
$WH \to l\nu cc(m_h = 145)$	0.000268
$WH \to l\nu\tau\tau(m_h = 145)$	0.000645
$WH \to l\nu bb(m_h = 150)$	0.003644
$WH \to l\nu cc(m_h = 150)$	0.000160
$WH \to l\nu\tau\tau(m_h = 150)$	0.000388

Table 6.6: Signal WH MC samples with cross sections. The number of events is calculated after applying the DQ cuts and duplicate events removal.

Mode	Run IIb σ (pb)
$W \to \ell\nu + 0lp\ excl$	4510
$W \to \ell\nu + 1lp\ excl$	1280
$W \to \ell\nu + 2lp\ excl$	304
$W \to \ell\nu + 3lp\ excl$	72.6
$W \to \ell\nu + 4lp\ excl$	16.8
$W \to \ell\nu + 5lp\ incl$	5.15
$W \to \ell\nu + 2c + [0-3]lp\ incl$	87.96
$W \to \ell\nu + 2b + [0-3]lp\ incl$	87.96
WZ $\to$ any	3.25
WW $\to$ any	11.6
ZZ $\to$ any	1.33
$t(q)b \to \ell\nu b(q)b$ tb-eνbb	1.06
$t\bar{t} \to 2b + 4lp + [0-2]lp\ incl$	2.23
$t\bar{t} \to 2b + \ell\nu + 2lp + [0-2]lp\ incl$	2.22
$t\bar{t} \to 2b + 2\ell + 2\nu + [0-2]lp\ incl$	.5561

Table 6.7: Background MC samples with cross sections (without K-factors). For the W+jets samples, only leptonic W decays are simulated. The number of events is calculated after applying the DQ cuts and duplicate events removal. The $t\bar{t}$ cross sections correspond to an inclusive $t\bar{t}$ production cross section of 7.26 pb, this value will be scaled in the limit setting stage to 7.04 pb [35].

Mode	Run IIb
	σ (pb)
$z \to \mu\mu + [0-3]lp\ incl\ M_Z[15-75]$	516.1
$z \to \mu\mu + [0-3]lp\ incl\ M_Z[75-130]$	245
$z \to \mu\mu + [0-3]lp\ incl\ M_Z[130-250]$	1.79
$z \to \tau\tau + [0-3]lp\ incl\ M_Z[15-75]$	508
$z \to \tau\tau + [0-3]lp\ incl\ M_Z[75-130]$	240
$z \to \tau\tau + [0-3]lp\ incl\ M_Z[130-250]$	1.86
$z \to \nu\nu + [0-5]lp\ incl$	1470

Table 6.8: Z + light flavor MC samples with cross sections (without K-factors). The number of events is calculated after applying the DQ cuts and duplicate events removal.
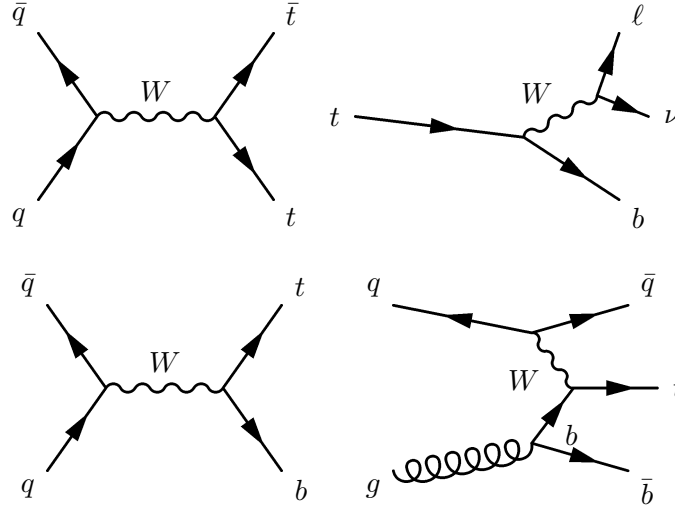
Figure 6.3: Top Left: Production mode for a $t\bar{t}$. Top Right: decay channel for a single top quark. Bottom left: S-Channel single top production Bottom Right: T-Channel Single top production

brings the LO or LL calculation in line with the NNLO calculation. These factors are k and k' for LO and LL cross-sections, respectively. In addition, we have dedicated Monte Carlo for $Z + cc/bb$ and $W + cc/bb$ processes. These are further corrected by taking the ratio of the heavy flavor process to a corresponding light flavor process. For example the

Mode	Run IIb
	σ (pb)
$z \to \mu\mu + c\bar{c} + [0-3]lp\ incl\ M_Z[15-75]$	11.8
$z \to \mu\mu + c\bar{c} + [0-3]lp\ incl\ M_Z[75-130]$	3.82
$z \to \mu\mu + c\bar{c} + [0-3]lp\ incl\ M_Z[130-250]$	0.032
$z \to \tau\tau + c\bar{c} + [0-3]lp\ incl\ M_Z[15-75]$	12.0
$z \to \tau\tau + c\bar{c} + [0-3]lp\ incl\ M_Z[75-130]$	3.66
$z \to \tau\tau + c\bar{c} + [0-3]lp\ incl\ M_Z[130-250]$	0.0311
$z \to \nu\nu + c\bar{c} + [0-3]lp\ incl\ M_Z[130-250]$	22.3
$z \to \mu\mu + b\bar{b} + [0-3]lp\ incl\ M_Z[15-75]$	1.55
$z \to \mu\mu + b\bar{b} + [0-3]lp\ incl\ M_Z[75-130]$	1.42
$z \to \mu\mu + b\bar{b} + [0-3]lp\ incl\ M_Z[130-250]$	0.0121
$z \to \tau\tau + b\bar{b} + [0-3]lp\ incl\ M_Z[15-75]$	1.54
$z \to \tau\tau + b\bar{b} + [0-3]lp\ incl\ M_Z[75-130]$	1.43
$z \to \tau\tau + b\bar{b} + [0-3]lp\ incl\ M_Z[130-250]$	0.012
$z \to \nu\nu + b\bar{b} + [0-3]lp\ incl\ M_Z[130-250]$	8.4

Table 6.9: Z + heavy flavor MC samples with cross sections (without K-factors). The number of events is calculated after applying the DQ cuts and duplicate events removal.
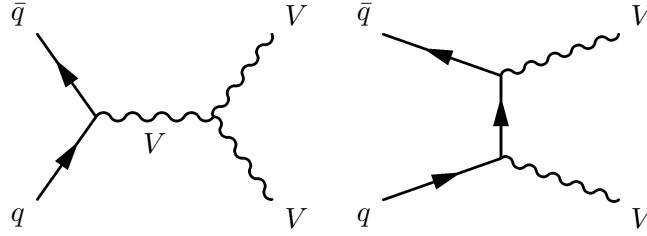
Figure 6.4: Diboson backgrounds. Note that V can be either a W or Z, but charge conservation rules dictate available channels

$W(\rightarrow l\nu)$ + light flavors	1.3	$Z(\rightarrow ll, \rightarrow \nu\nu)$ + light flavors	1.3
$W(\rightarrow l\nu)$ + cc	1.3*1.47	$Z(\rightarrow ll, \rightarrow \nu\nu)$ + cc	1.3*1.67
$W(\rightarrow l\nu)$ + bb	1.3*1.47	$Z(\rightarrow ll, \rightarrow \nu\nu)$ + bb	1.3*1.52
$W(\rightarrow l\nu)$ + c	1.3*1.42		
$t\bar{t} \rightarrow$ any decay	1.43	WW	1.0
single top$\rightarrow l\nu b$ (s-channel)	0.99	WZ	1.06
single top$\rightarrow l\nu b$ (t-channel)	0.99	ZZ	1.03

Table 6.10: $k(')$ and HF-factors used for Run II Monte Carlos

$Z \rightarrow (\ell\ell, \nu\nu)+bb$ is corrected using the ratio of the k factors for $Z \rightarrow any+2b/Z \rightarrow any+2lp$. This is called the HF factor and is calculated for bb,cc or inclusive c+jet production.

For W+light flavor processes an event may be generated with a single charm quark due to a strange quark in the initial state. To account for this we segregate these events from the other $W+$ light flavor processes. In plotting we keep this separation of variables, but combine single and double top as well as diboson processes.

The di-boson production cross sections are calculated with MCFM, and the cross sections for top-pair and single-top are taken from Ref. [35].

A full list of cross-sections and branching ratios for Higgs MC can be found in Table **??**.

A summary of the different k, k', and HF factors is shown in Table 6.10.

6.3.2 Heavy Flavor skimming

All ALPGEN samples are produced with initial state light partons (gluons, u, d, or s quarks) in exclusive multiplicity bins, except the highest bin which is inclusive of higher multiplicities. All ALPGEN W/Z+jets samples have undergone a process of heavy-flavor (HF) skimming. Meaning events containing heavy-flavored partons generated by PYTHIA in the region of phase space where they are also generated by ALPGEN in the hard process, have been removed in order to avoid double counting of heavy flavor production.

6.3.3 ALPGEN Reweighting

The Z and W p_T spectra are not properly modeled in ALPGEN and PYTHIA below their production threshold. For this reason, independent reweighting functions are derived on a $Z \to ee$ data sample. For PYTHIA samples, $Z \to ee$ samples are generated in Z mass windows of 15-60, 60-130, 130-250 GeV. Then a data-to-MC scale factor is applied as fit by [36]

$$\left(p_0 + p_1 \left[1 + Erf \left\{ \frac{p_T - p_2}{\sqrt{2}p_3} \right\} \right] \right) e^{-p_4 p_T} + p_5 \sqrt{p_T} e^{p_6 p_T^2} \tag{6.1}$$

For ALPGEN, a similar procedure is followed, but the samples are also generated with additional initial state light and heavy quarks. The fit for ALPGEN is:

$$\left(p_0 + p_1 \left[1 + Erf \left\{ \frac{p_T - p_2}{\sqrt{2}p_3} \right\} \right] \right) e^{-p_4 p_T} \tag{6.2}$$

For W+jets, no complementary distribution to the Z boson exists, so a new reference distribution must be sought. A study has been done on the ratio of W to Z cross-sections at NLO and NNLO as a function of p_T [37]. The ratio is expressed by:

$$\frac{1}{\sigma} d\sigma(W) dp_T / \frac{1}{\sigma} d\sigma(W) dp_T = 1.0095 \times e^{-p_T/543} \tag{6.3}$$

However, this ratio is not reproduced perfectly in the generators, thus the Z p_T reweighting distributions can not directly be applied to the W samples. Instead the ratio is applied to the Z p_T distribution and new reweighting functions of the same form are derived.

After these reweightings is was still found that in many selections ALPGEN samples do not perfectly model angular distributions. For this reason we derive reweighting functions which correct for these generator level imperfections. This reweighting function was derived on our independent electroweak control sample and is described in Appendix D. After deriving and applying a reweighting function to the $\Delta\eta$ distribution between the two leading jets, we find an improvement also in the modeling of the $\Delta\phi$ between the two leading jets and the dijet mass distribution. For this reason we keep this simple form of corrections.

In addition, we apply to the (W/Z)+light-flavor-jets samples a reweighting recommended in Ref. [38], designed to correct the MLM matching p_T threshold, which was seen to be more appropriate at 13 GeV than at the default 8 GeV used in our MC sample generation.

6.3.4 Luminosity Reweighting

To describe ambient noise in our detector in the MC simulation, real zero bias events overlay the MC production. Due to differences in the instantaneous luminosity of those zero bias events compared to the data set, all MC events have been reweighted in luminosity to match the data distribution.

6.3.5 Data Quality

For MC, we apply the same data quality requirements as for our data samples. Because real zero-bias events are overlaid on the MC, some events will be be flagged as noise. These flagged events are rejected at preselection.

6.3.6 Jet Shifting Smearing and Removing (JSSR)

To account for differences in energy scale, resolution, and reconstruction and identification efficiency between data and simulation, MC jets are shifted and smeared and possibly removed [39]. As suggested in Ref. [40], we turn off the shifting for quark dominated final states (double and single top, dibosons, V+bb/cc, and signal). The energy changes resulting from this processor are then propagated to the $\not{E}_T$.

6.3.7   Vertex Confirmation and Direct Taggability Scale Factors

In general, the MC simulation of our detector overestimates the efficiency of our subdetectors. When subject to the criteria for taggability more jets are passed. This is especially prevalent in the poorly instrumented ICD region. A scale factor dependent on η_{det} and jet p_T is derived and applied to bring the MC prediction in line with data.

6.4   Signal Selection

In a second set of criteria, we further distinguish events which exhibit desired characteristics of the large $\not{E}_T$ final state. Here, we describe the criteria that give the analysis sample where the search for the Higgs boson is performed. To create control samples to investigate and verify background modeling, a criterion maybe inverted, thus creating an orthogonal sample. The signal sample is defined as:

- The highest p_T good jet in the event has to be taggable.

- At least one but no more than three taggable jets with $p_T > 20$ GeV and $|\eta| < 2.5$. This primarily reduces contamination from double top events

- Acoplanarity $\Delta\phi(\text{jet}_1, \text{jet}_2) < 165°$ (The two leading jets must not be back-to-back in the plane transverse to the beam direction as we expect a boosted Higgs boson.)

- $\not{E}_T > 40\,\text{GeV}$

- $\not{E}_T$ Significance > 5. The "missing E_T significance", $\mathcal{S}$, variable takes into account the resolution of jet energies to assess the significance of the observed $\not{E}_T$ relative to expected fluctuations in measured jet energies. The larger the $\mathcal{S}$, the more likely it is that the observed $\not{E}_T$ is not due to such fluctuations. It is calculated using the standard DØ algorithm [41], and unclustered energy smeared in the simulation as described in Ref. [42]. The distribution of missing E_T significance in the electroweak control and analysis sample (see Section 6.6) is shown in Fig. 6.5, with the $\mathcal{S} > 5$ cut removed.

- Veto on isolated electrons and muons as described in section 5.3. This cut is designed to reduce the background from $(W \rightarrow \ell\nu)$+jets, and ensure orthogonality to other searches

- $\mathcal{D} < \pi/2$, where $\mathcal{D} = \Delta\phi(\not{E}_T, \not{p}_T)$. For signal, the missing track-p_T, $\not{p}_T$, defined as the opposite of the vectorial sum of the charged particle transverse momenta, is expected to point in a direction similar to that of $\not{E}_T$. This is not expected in multijet events, in which the $\not{E}_T$ originates mainly from mismeasurements of jet energies, this is further described in section 6.4.3

In the following, any "dijet" quantity, such as dijet invariant mass, dijet acoplanarity, or dijet ΔR, is calculated using the two leading taggable jets when available or the taggable jet and the preferred remaining jet. Taggable jets are preferred. In the absence of a taggable jet, we use a good jet with $p_T > 20 GeV$ and $|eta| < 2.5$; the jet with the remaining highest p_T is preferred.

6.4.1   Bad Jets

Events that contain bad jets with $p_T > 15\,$GeV are rejected. In this context, bad jets are those jets that do not pass the Jet-ID criteria. Events with bad jets contribute largely to the instrumental background because of two reasons: a) the JES correction is not applied for these jets, thus their p_T is mis-measured and this is also propagated to the $\not{E}_T$; b) coarse hadronic cells for the $\not{E}_T$ computation are only taken into account if they belong to jets passing the Jet-ID criteria. One of the reasons why these bad jets fail the Jet-ID is due to the CHF being larger than 0.4. Thus, we expect in these events a large energy deposited in the coarse hadronic part of the calorimeter which is not taken into account for the $\not{E}_T$ computation.

Events with two good jets are not rejected if they have only one bad jet with the only failed Jet-ID criterion being the EM fraction > 0.95, to retain acceptance for the WH signal where the electron from the W decay fakes a jet. The JES corrections are not applied on these bad jets (as they are misidentified EM objects). All good jets and retained bad jets
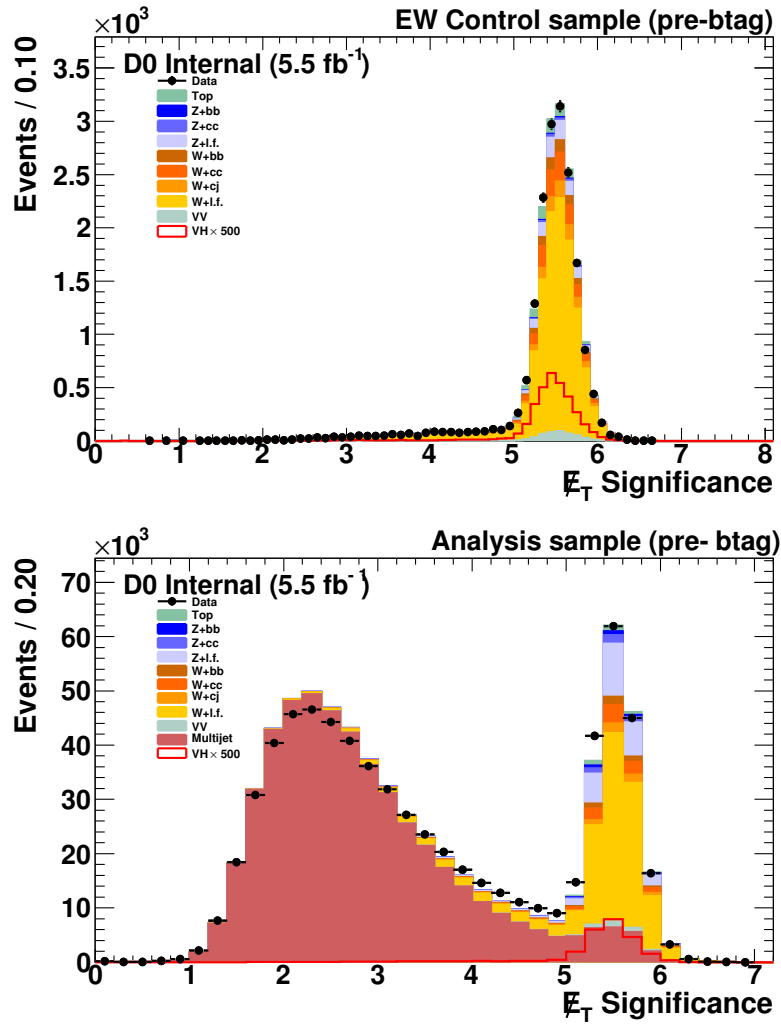
Figure 6.5: Missing E_T significance in the electroweak control sample (top) and in the analysis sample (bottom) before any cut is applied.
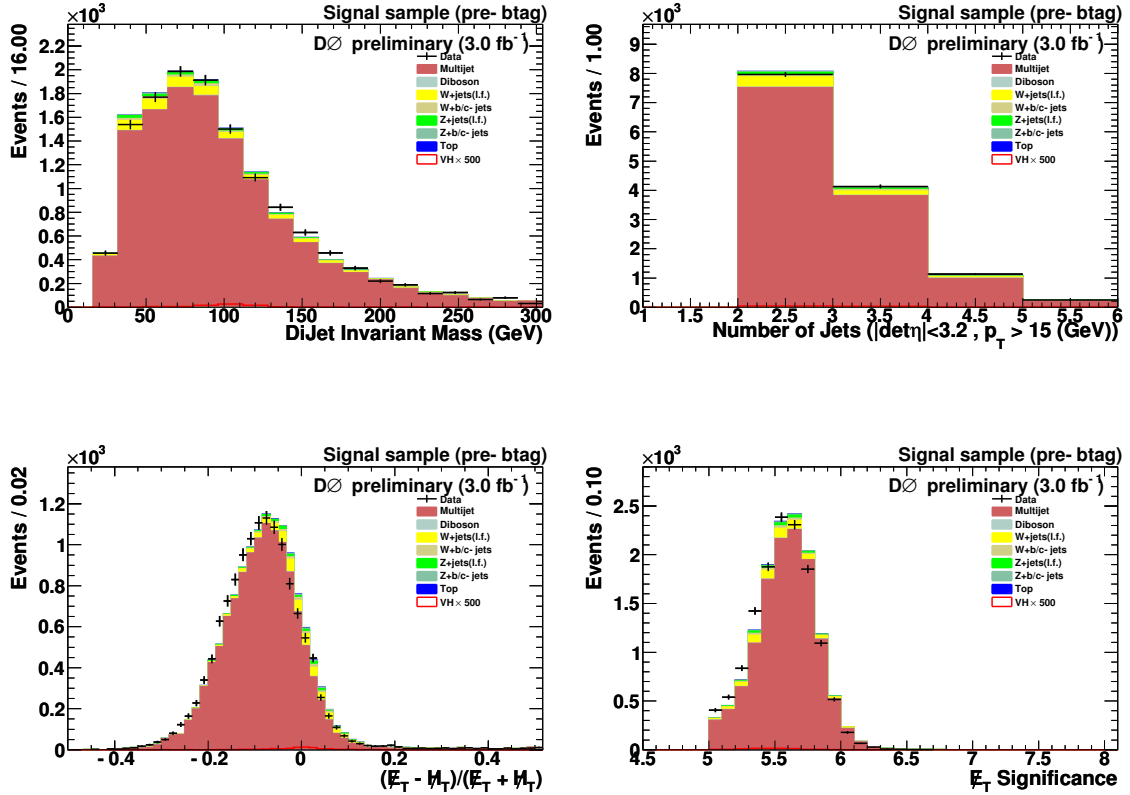
Figure 6.6: Distributions in events where a jet fails the Jet-ID criteria and which otherwise pass the cuts applied in the signal sample.

are propagated to the H_T and $\not{H}_T$ calculation.

To check the effect on the multijet background, and overall modeling of the data, the veto on these events with a bad jet was inverted in our signal sample, obtained as described later (Sec. 6.4). It can be seen from Fig.6.6 that the modeling of these bad jets matches very well the data, once the small standard model contributions are included. This gives confidence in the bad-jet veto not biasing the multijet modeling.

6.4.2   Vertex confirmation and taggability

For the Run IIb samples, there must be one taggable jet, and the second jet, if not taggable, must have $p_T > 20 GeV$ and $|\eta| < 2.5$. These requirements remove a large fraction of the

instrumental background (Table 6.1) by rejecting events with fake jets, or events where the wrong primary vertex was selected.

6.4.3   Sideband and MJ-model sample

The variable $\mathcal{D}$ is used to define the "signal sideband." It is selected in the same way as the signal sample, except that the requirement $\mathcal{D} < \pi/2$ is now inverted. To define the multijet model (MJ-model), the small contribution from SM processes in that $\mathcal{D} > \pi/2$ sideband is subtracted, and the resulting sample is used to model the multijet background in the signal sample, i.e., in the $\mathcal{D} < \pi/2$ region. The MJ-model sample is normalized such that, after adding contributions from the SM backgrounds in the signal sample, the expected number of events is identical to the number observed in the signal sample.

A multijet model sample described in section 6.7 is constructed realizing all criteria designed to constrain multijet events. This sample is used to verify the Multijet modeling

The multijet-model sample is normalized such that, after adding the SM background contribution, the number of events expected is equal to the number of events observed in the signal sample with $\mathcal{D} < \pi/2$.
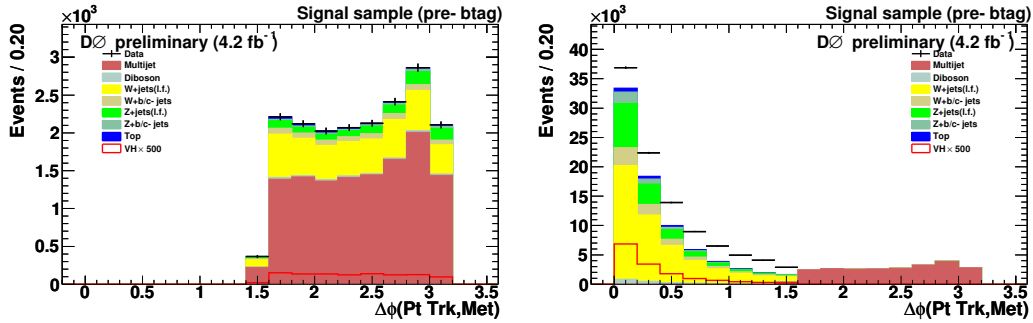
Figure 6.7: The left plot shows details of the signal sideband: below the SM contributions, the events used to model the multijet background (MJ-model sample) are shown in brown. The right plot shows those same MJ-model events, in brown, for $\mathcal{D} > \pi/2$, with the SM contributions removed; here the MJ-model normalization is adjusted such that the MJ-model compensates the difference between data and SM contributions seen for $\mathcal{D} < \pi/2$ (data shown as black points, SM contributions as colored histograms).

6.4.4   Cut Flow

The number of events after each selection cut for the MC signal samples and the observed data events in the signal sample for RunIIb can be seen in Table 6.11.

Selection	Data			$ZH \to \nu\overline{\nu}b\overline{b}$ MC (115 GeV)			$WH \to \ell^{\pm}\nu b\overline{b}$ MC (115 GeV)		
	Events	Rel.(%)	Abs.(%)	Events	Rel.(%)	Abs.(%)	Events	Rel.(%)	Abs.(%)
Pre-selection	6359015	-	-	33.41	-	-	59.20	-	-
Bad Jet Veto	6105220	96.01	96.01	33.14	99.19	99.19	58.59	98.97	98.97
Leading Jet Taggable	4502085	73.74	70.80	29.80	89.93	89.20	51.69	88.21	87.30
$\Delta\phi(\text{jet}_1, N\text{jet}_1) \le 165°$	3849543	85.51	60.54	29.40	98.65	87.99	49.17	95.14	83.06
Veto on $N_{\text{taggable jets}} \le 3$	3669352	95.32	57.70	28.63	97.37	85.68	47.77	97.16	80.70
$\not{E}_T \ge 40\,\text{GeV}$	1334393	36.37	20.98	27.88	97.38	83.44	45.15	94.51	76.27
METsign ≥ 5	276848	20.75	4.35	25.34	90.88	75.83	39.35	87.16	66.47
Isolated Muon Veto	250340	90.43	3.94	23.38	92.28	69.98	30.90	78.52	52.19
Isolated Electron Veto	231526	92.48	3.64	23.30	99.64	69.73	26.29	85.09	44.41
$\Delta\phi(\not{E}_T, \not{p}_T^{\text{trk}}) < \pi/2$	183749	79.36	2.89	21.47	92.16	64.26	22.24	84.59	37.57

Table 6.11: Cut-flow for Run IIb selection (All scale factors applied for the signal, with an integrated luminosity of 5.5 fb^{-1})
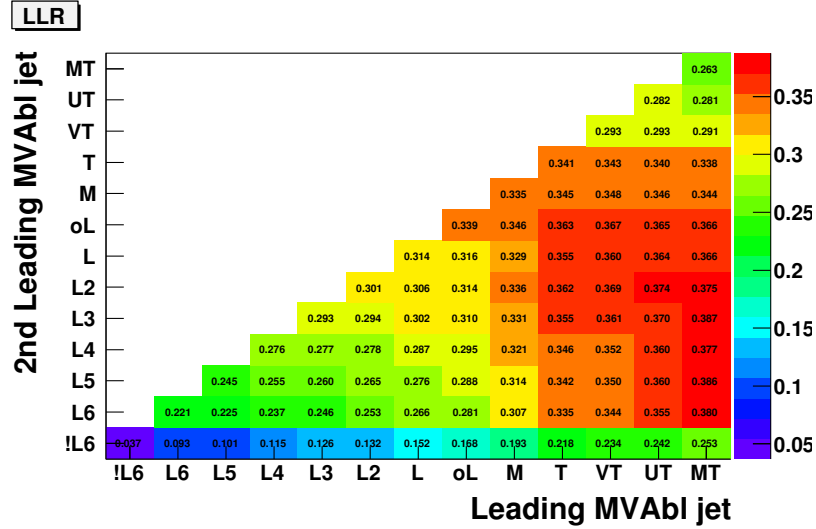
Figure 6.8: Distribution of ΔLLR for the various MVA Operating points for the two leading taggable jet s. Tighter cuts go from left to right, bottom to top

6.4.5   Tagged Samples

As described in Section 5.4.1, different tagging points are made as a compromise between efficiency and fake rate. We choose our tagging point using the optimal sum by histogram bin of the log-likeliehood ratio in the final discriminate after MJ-DT cut (see Figure 6.8):

$$\Delta LLR = \sum_{bins} \delta LLR = \sum_{bins} S \times Log(1 + \frac{S}{B})$$

(6.4)

We believe this gives us a good measure of the sensitivity provided at the different operating points. We make a matrix of available tagging points for the two taggable jets to be optimized.

It is found that the optimal combination for this analysis is a MegaTight(MT)-L3 asymmetric tag point. However, the improvement gained over the previously used VeryTight(VT)-L3 point is minimal, and to keep a coherence among all low mass searches this point is used. To further enhance our sensitivity an orthogonal tagging point is created defined with on VT tag and requiring the other jet not be tagged above L3 (or !L3). We also include all events with one taggable jet that can VT tagged in this single tag sample.

6.4.6 Calculated Variables

From the detector output, we are given a great deal of information about the kinematic variables in an event. The distributions of η and the invariant mass can be used to differentiate background and signal-like events. However, combining information about many of these variables, can provide additional separation ability. Here we describe some variables that we found to have undamental differences for signal and background events.

Higgs decay angle, $\cos(\theta_{Higgs})$

θ_{Higgs} is the angle between the Higgs-candidate direction and the leading analysis jet, boosted back in the Higgs-candidate rest frame. We use the cosine of this angle, expected to be flat for the decay of a scalar, in contrast to gluon splitting.

Jet Pull, $\theta_{rel,jet}$

It has been shown in [43] that two jets with identical 4-vector kinematics can be distinguished by their "jet pull" vectors:

$$\vec{p} = \Sigma_i \frac{E_T^i |r_i|}{E_T^{jet}} \vec{r}_i \tag{6.5}$$

Where the summation is over the cells that make up the jet and $\vec{r}_i$ is in the direction of the jet center to the cell.

Jets originating from color singlets (signal b-quarks) will have jet pull vectors pointing towards each other, while non-matched color pairs (background) will tend to point away from each other and along the beam. In this analysis we use the relative jet pull angle $\theta_{rel,jet} = \theta_j - \theta_{p,jet}$ where θ_j is the angle in the eta-phi plane between the centers of the two jets and $\theta_{p,jet}$ is the angle calculated from the jet pull vector.

Sigma

The variable Σ is calculated between a jet and the Higgs candidate, in the rest frame of the candidate and also considering the fraction of transverse momentum carried by the jet as

given by:

$$\Sigma(\hat{d}) = \frac{\Sigma_i \Delta R(\hat{d}, jet_i) \times p_T^{jet_i}}{\Sigma_{jets} p_T^{jet}} \tag{6.6}$$

Where $\hat{d}$ is the direction of the Higgs candidate in its rest frame and the summation over i can be over one, two, or three candidate jets in the calculation. This is a p_T weighted ΔR distribution and is sensitive to mother particle's mass. We expect signal events to be relatively back-to-back in the rest frame of the Higgs candidate and with equal distribution of p_T in the jets. Thus we expect a symmetric distribution while this may not be the case for background events. For this analysis we use Σ calculated with the next-to-leading jet.

Recoil Subtracted dijet $p_\perp$

The recoil subtracted dijet p$_\perp$ is closely related to a similar variable defined in DØ's $ZZ \rightarrow ll\nu\nu$ result [44]. In the transverse plane we define a dijet thrust axis, which is the transverse momenta of the leading minus the next-to-leading jet, $\vec{p}_T^{Ljet} - \vec{p}_T^{NLjet} = \vec{a}_l$ in the direction $\hat{a}_l$ and perpendicular component $\hat{a}_t$. The dijet transverse momentum is then decomposed into parallel and perpendicular components to the thrust axis, $\vec{p}_{T,l}^{jj}$ and $\vec{p}_{T,t}^{jj}$, respectively. We keep only the transverse component "dijet p$_\perp$" $= p_{T,t}^{jj} = \vec{p}_T^{jj} \cdot \hat{a}_t$, which is robust against jet resolution effects so it gives a good discrimination against multijet events which have high $\not{E}_T$ due to jet mismeasurements. A recoil activity correction is further defined either using the jet-uncorrected $\not{E}_T$ or the remaining jets in the event ($p_T > 15$ GeV and $|\eta| < 3.2$) which has a p_T in the opposite direction of the jet pair. We choose the one with the largest projected magnitude in the hemisphere opposite to the dijet pair, i.e. the one that minimizes the "dijet p$_\perp$". The recoil activity is enhanced with a factor of two to account for the underestimation of the true recoil energy. So our variable is:

$$\text{recoil subtracted dijet } p_\perp = p_{T,t}^{jj} + 2 \times min(-\not{E}_{T\,uncorr} \cdot \hat{a}_t, \sum_{jets} p_T^{jet} \cdot \hat{a}_t, 0) \tag{6.7}$$

6.5 *Normalization*

In the presentation of the analysis and control samples, we adopt a data-driven normalization procedure for the main SM backgrounds. This is done in an effort to better discern between shape-dependent issues from those arising from sample production and normalization. These normalizations are not used in the final limit setting, as the application that does this calculates the normalizations independently. However, the normalizations used here are close in form to those calculated for limit setting and are used in the training of decision trees.

We calculate separate normalization (scale) factors for all $W/Z + jets$ samples and for top production. We also calculate a separate scale factor for heavy flavor production in $W/Z + jets$.

The figure of merit for the scale factor calculation is the jet multiplicity distributions in the zero, one, and two tag samples. For each of the electroweak control sample, signal sample before cutting on the MJ-DT output, and signal sample after applying that cut, we perform a χ^2 fit of these three scale factors to the jet multiplicity distributions in the 0, 1 and 2-tag samples. The heavy flavor and top scale factors are constrained within their a priori uncertainties, taken to be Gaussian, of 20% and 10%, respectively, while the overall (W/Z)+jets scale factor is left floating in the fits. In the signal sample before MJ-DT cut, we calculate in addition the normalization of the multijet component by including in the fit the forty bins of the MJ-DT distribution. This multijet normalization is kept after MJ-DT cut.

The results of these various fits are given in Table 6.12.

Sample	Electroweak	signal pre-MJDT cut	signal after MJDT cut
(W/Z)+jets	1.08 ± 0.02	1.11 ± 0.01	1.13 ± 0.01
Heavy flavors	0.94 ± 0.10	0.98 ± 0.02	0.93 ± 0.07
Top	1.08 ± 0.08	1.00 ± 0.05	1.00 ± 0.08

Table 6.12: Scale factors obtained from fits in the various samples.

6.6 Electroweak Control Sample

A W+jets sample is constructed and used used to verify our MC modeling of the electroweak (EW) backgrounds, the trigger simulation and the b-tagging performance. To construct this sample we again make use of the fact that the muon acts as a minimum ionizing particle in the detector. By requiring a muon (from $Wh \rightarrow \nu\mu b\bar{b}$), and subsequently subtracting its contribution inside the detector we can closely mimic the $\not{E}_T + bb$ final state. The advantage here is that we create an orthogonal sample with which we can test our background model that is virtually void of multijet background.

We apply in this sample the analysis cuts we use in the signal sample and in addition we cut on the tight muon-corrected $\not{E}_T > 20\,\mathrm{GeV}$ and require that the transverse mass of the W candidate is greater than 30 GeV. These additional cuts are used to remove all the remaining multijet contribution from this sample, and it has been verified that the multijet background is less than 1%.

With the scale factors from Table 6.12, the numbers of events observed and expected from the various background sources are given in Table 6.13 before b tagging and for an asymmetric VT-L3 double tag.

Plots of various variable distributions before b-tagging can be seen in Figure 6.9. and after double asymmetric (VT-L3) tagging in Figure 6.10. Overall, there is good agreement between the observed data and the expected background, both before and after b-tagging.

Sample	Before b-tagging		1 VT and 1 L3 tag	
ZH (115 GeV)	0.71	± 0.01	0.21	± 0.01
WH (115 GeV)	5.66	± 0.06	1.64	± 0.03
W+jets	11093.27	± 51.30	8.02	± 2.16
W+c+jet	832.47	± 15.90	5.55	± 1.43
W+cc	1401.51	± 18.47	16.83	± 2.34
W+bb	614.80	± 7.16	67.93	± 2.49
Z+jets	968.61	± 16.99	0.83	± 0.45
Z+cc	138.39	± 3.75	1.95	± 0.41
Z+bb	68.19	± 1.50	8.38	± 0.49
top	703.65	± 2.83	134.34	± 1.01
di-boson	482.53	± 7.15	6.18	± 0.60
Total Bgrd	16303.43	± 60.34	250.00	± 4.52
Observed	16282		267	

Table 6.13: RunIIb number of events after applying all analysis cuts including requiring the transverse mass of the W candidate to be greater than 30 GeV and before and after b-tagging. Errors are statistical only.
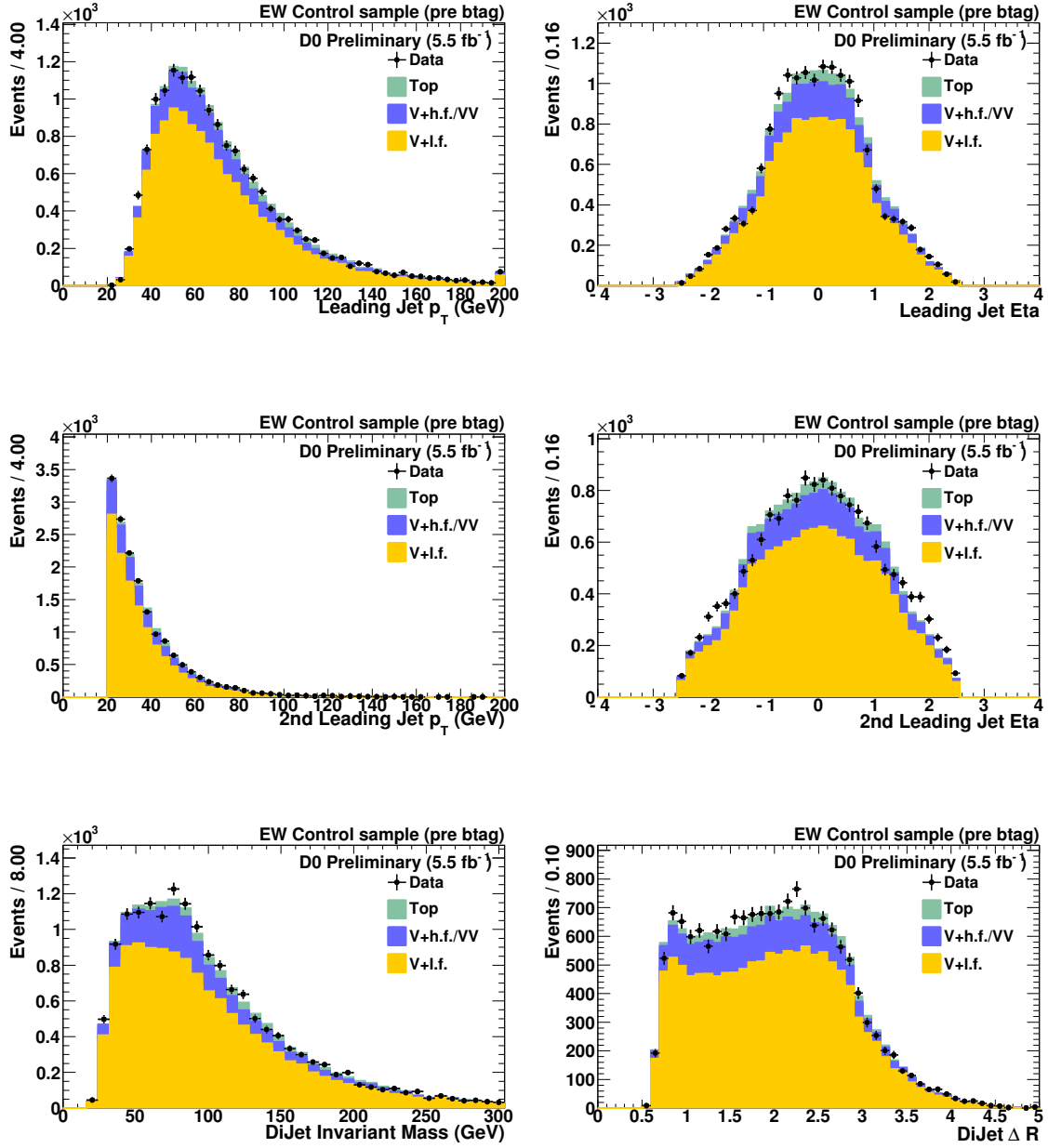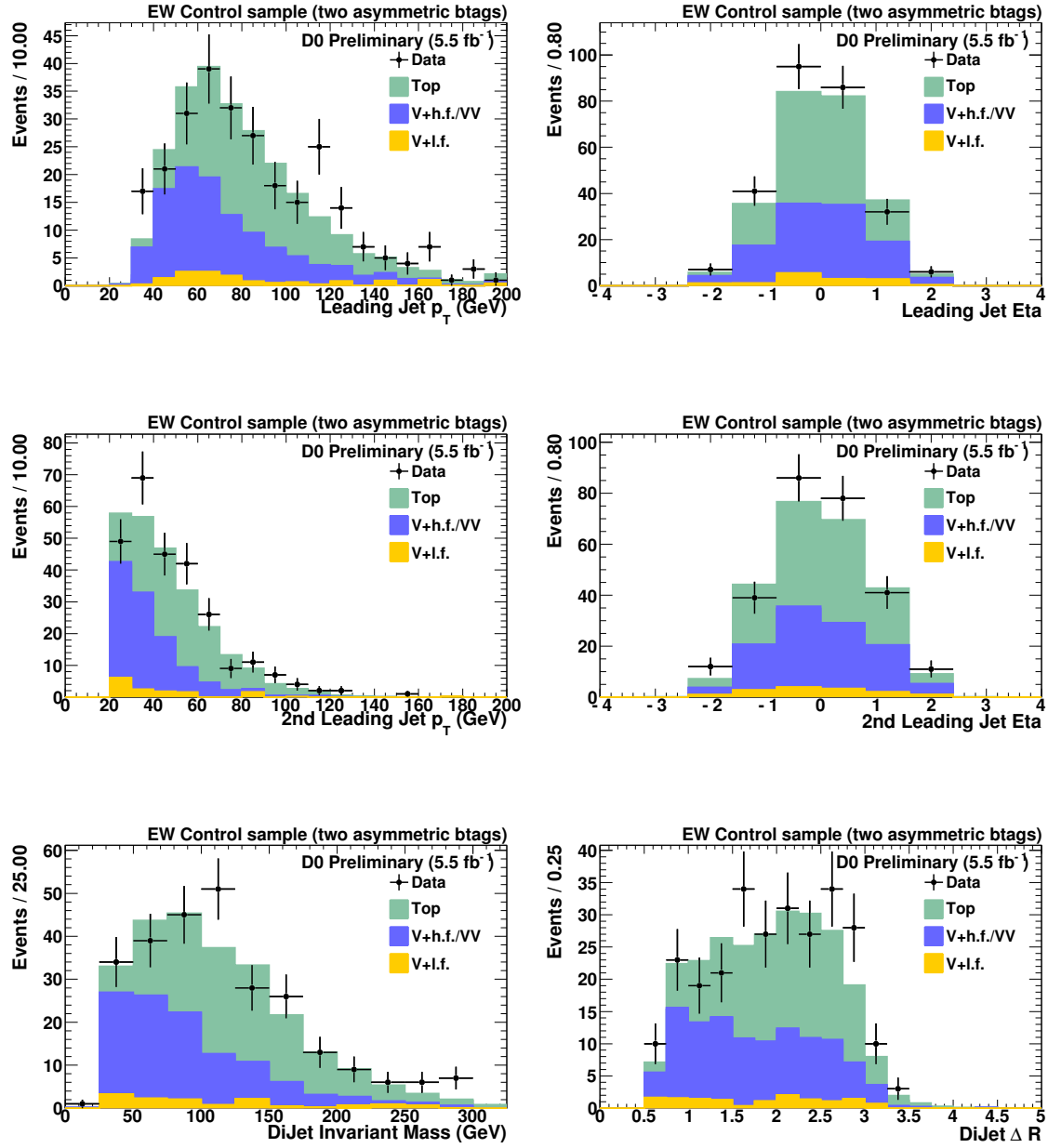
Figure 6.9: Electroweak control sample before *b*-tagging

Figure 6.10: Electroweak sample with one tight and one loose b-tag

6.7 Multijet Control Sample

As described in Section 6.4.3, the variable $\mathcal{D} = \Delta\phi(\not{E}_T, \not{p}_T^{\text{trk}})$ is used to define a sample dominated by the multijet background. It is selected in the same way as the signal sample, except that the cut $\mathcal{D} < \pi/2$ is now inverted, we call this our signal sideband. The $\not{p}_T^{\text{trk}}$ is computed only with tracks that originate from the primary vertex within $r_{dca} < 2\,\text{mm}$ and $z_{dca} < 5\,\text{mm}$ and have a $p_T \leq 400\,\text{GeV}$. The latter cut is used to reject fake tracks, as most tracks with a very high p_T are fake. After SM background subtraction, the signal sideband is used as the multijet-model in the signal sample, i.e., in the $\mathcal{D} < \pi/2$ region. The distribution of $\mathcal{D}$ after applying all selection cuts, before b-tagging, is plotted in Figure 6.7.

To test this multijet-background modeling procedure, we define a multijet control sample which is largely enhanced in multijet events. This sample is selected in the same way as the signal sample, but the $\not{E}_T$ cut is relaxed from 40 to 30 GeV and other cuts specifically designed to reject multijet events are dropped. These are the $\not{E}_T$ triangle cut for Run IIa, and the cut $\mathcal{S} > 5$ on the $\not{E}_T$ significance. A multijet-model sample is then defined in the same way as for the signal sample, and compared with the multijet control sample in the $\mathcal{D} < \pi/2$ region.

With $\mathcal{D} > \pi/2$ we would like to model events where a calorimeter jet energy is mismeasured, thus leading to significant $\not{E}_T$ close to one of the jets. However, the $\not{E}_T$ can be also opposite to $\not{p}_T^{\text{trk}}$ in a perfect signal like event if the tracks of the highest energy jet are missing. This is more likely to happen for jets in the forward region where we would disregard tracks that have a CFT requirement, so this is abandoned for the enhanced sample..

To further suppress events in our multijet-model samples with such nature we compare the leading jet p_T measured with the calorimeter and the tracking in the multijet control sample. These two dimensional distributions are plotted for the $\mathcal{D} < \pi/2$ and $\mathcal{D} > \pi/2$ regions in Figure 6.11. As can be seen in these plots, the events from our multijet-model have more events with small jet p_T^{trk}. To reject events from our multijet-model sample with missing tracks we further define the multi-jet model to only include events with $3.0 * LJTrkPt + 20 > LJetPt$ where $LJTrkPt$ is the track p_T of the leading jet (vectorial sum

of tracks in the jet) and $LJetPt$ is the jet p_T measured with the calorimeter.
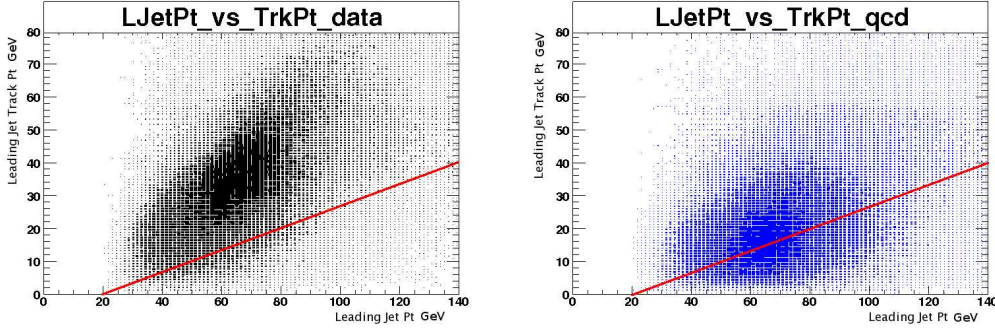

Figure 6.11: Data events from the signal like selection (black) and from the multijet sideband region (blue) in the Leading Jet Pt vs. Leading Jet Track Pt plane (p17). The red line shows the triangle cut on the 2-D plane.

All the calorimeter related variables in the multijet control sample are very well described by our multijet model, as shown before b tagging in Figure 6.12. The normalization factor for the multijet model is 1.32 for Run IIb.

The multijet-model sample has to be derived and normalized for each b-tagging point separately. The normalization factor in the multijet control sample is 1.40. Plots for the pretag and double tag multijet control sample are shown in Figs.6.12-6.13.

After applying b-tagging and the MJ-DT cut on the events used to model the multijet background, the statistics are strongly reduced and the results degraded by statistical fluctuations. We solve this problem by using the pre-tag shapes for the multijet background after MJ-DT cut. Prior to the MJ-DT cut we still use the single tag and double tag events.

We verified that the shapes in the single and double tag samples are reasonably reproduced by the pretag sample as shown in Figures and 6.14. For the final discriminants, nevertheless, we apply a pre-tag to post-tag correction as follows. In each of the one and two-tag samples, we take the final discriminant distribution of the multijet-model events with direct tagging, and divide it by the distribution obtained in the pretag sample (normalized to the same number of events). We fit this distribution of ratios by a first order polynomial, and obtain a slope by which we correct the pretag distribution, and an uncer-

tainty thereon that we use as systematic uncertainty. (Actually, we use the full 2x2 error matrix from the fit.) In practice, the slopes do come out consistent with zero (see Fig. 6.15).
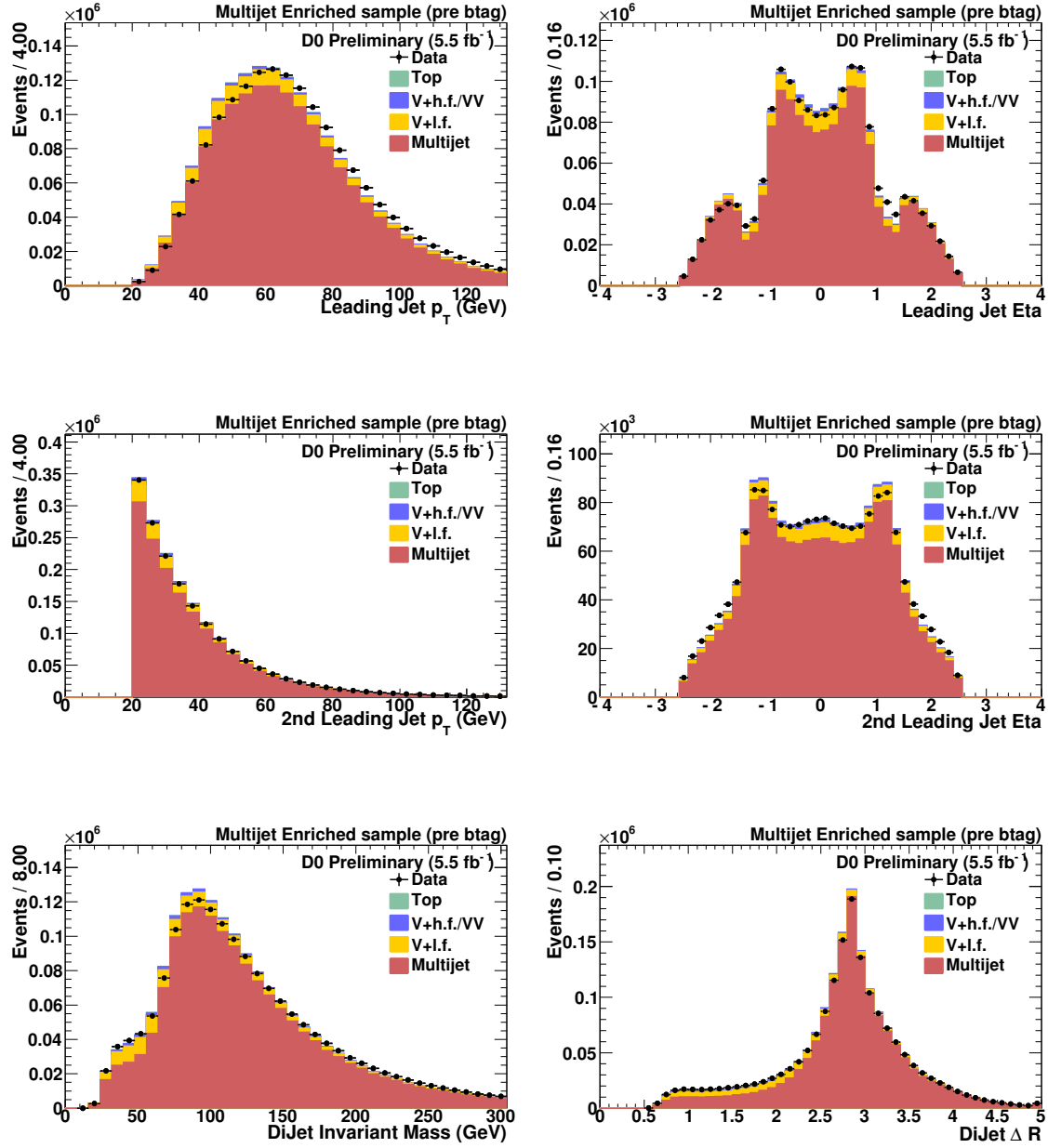
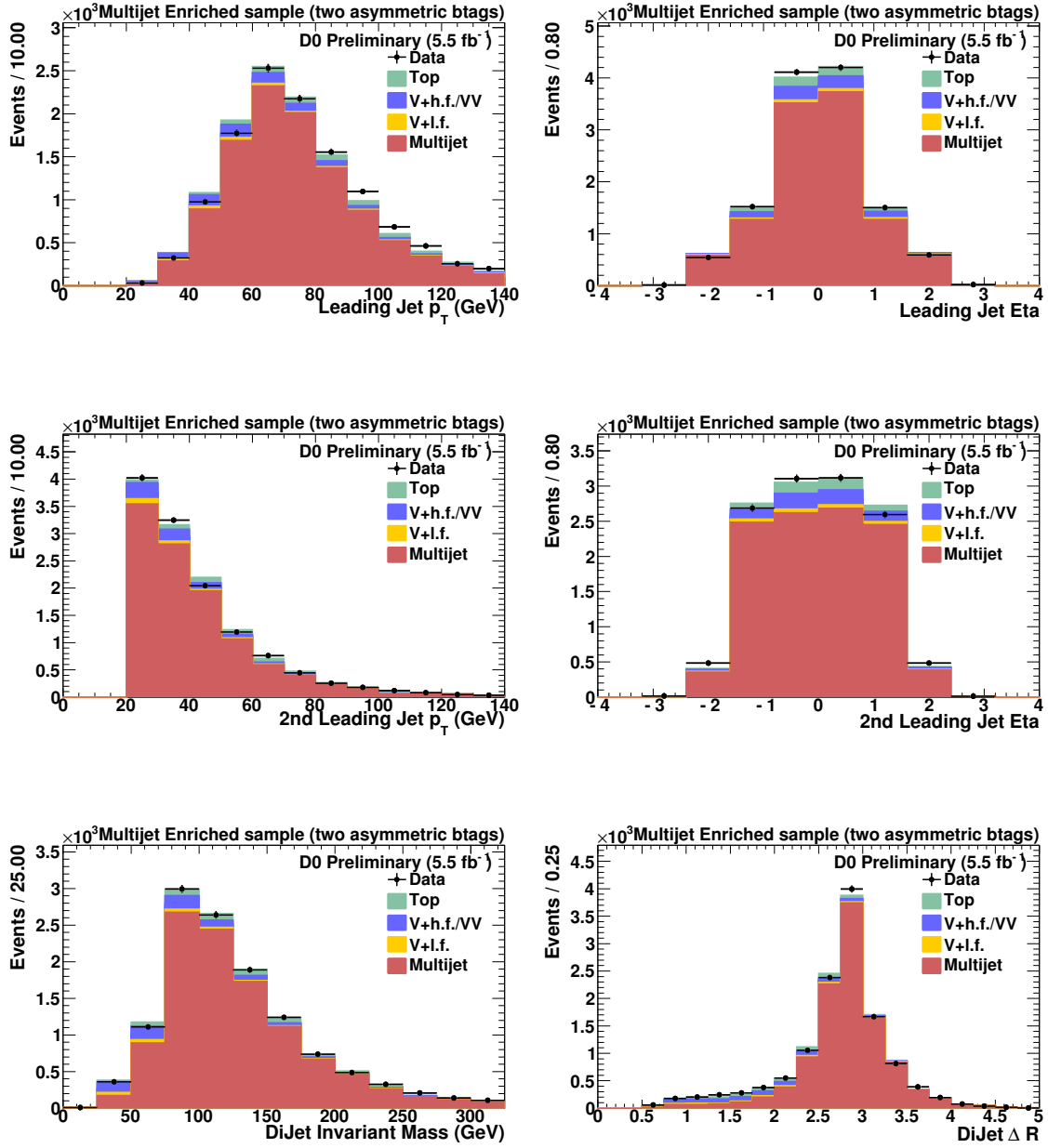Figure 6.12: Multijet control sample before *b*-tagging

Figure 6.13: Multijet control sample with one tight and one loose b-tag
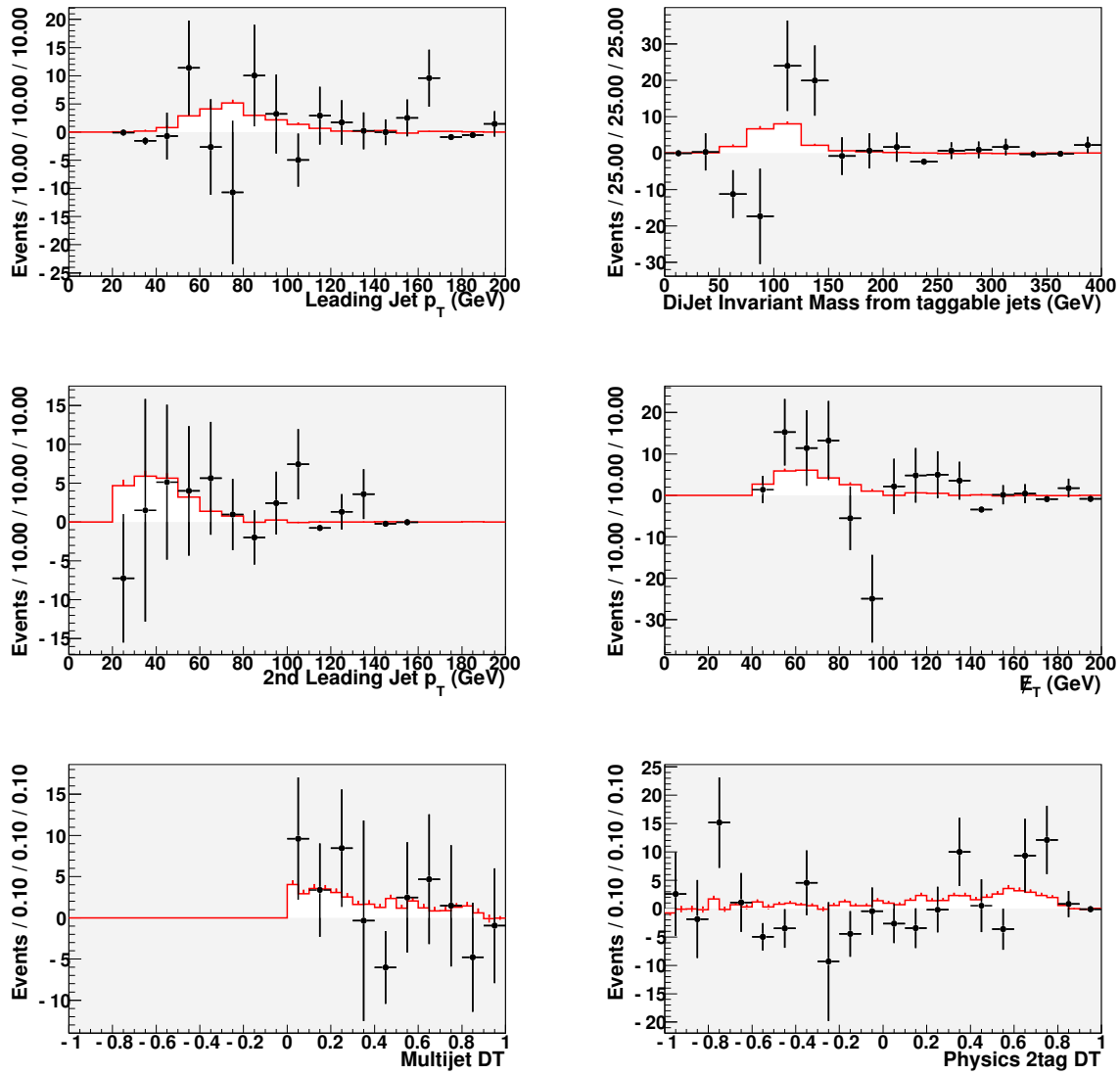
Figure 6.14: Comparison of pretag (solid line) and double tag (points) Multijet background shapes after MJ-DT cut
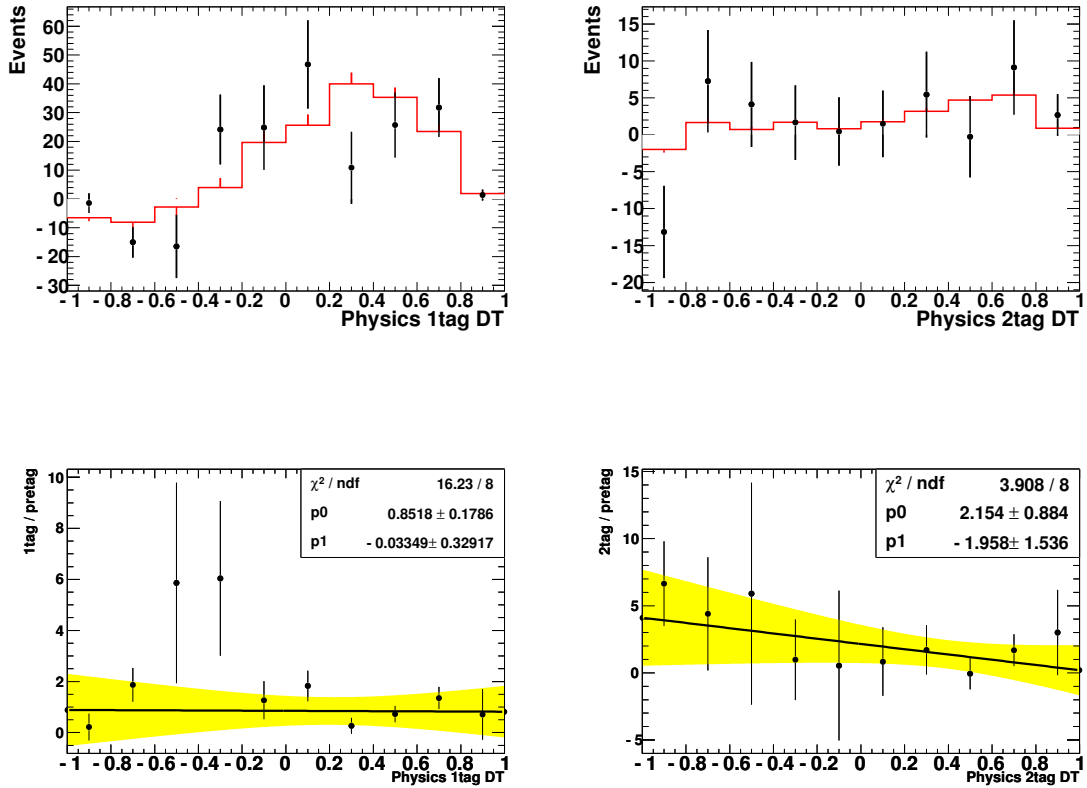
Figure 6.15: Top: Distributions of pre-tag (red histograms) and post-tag multijet background after MJ-DT cut. (The pre-tag is normalized to the number of post-tag events.) Bottom: Ratio of post-tag to pre-tag multijet background after MJ-DT cut, with a linear fit superimposed. (The yellow band is the fit uncertainty.)

126

Figure 6.16: Comparison of pretag (solid line) and single tag (points) Multijet background shapes after MJ-DT cut

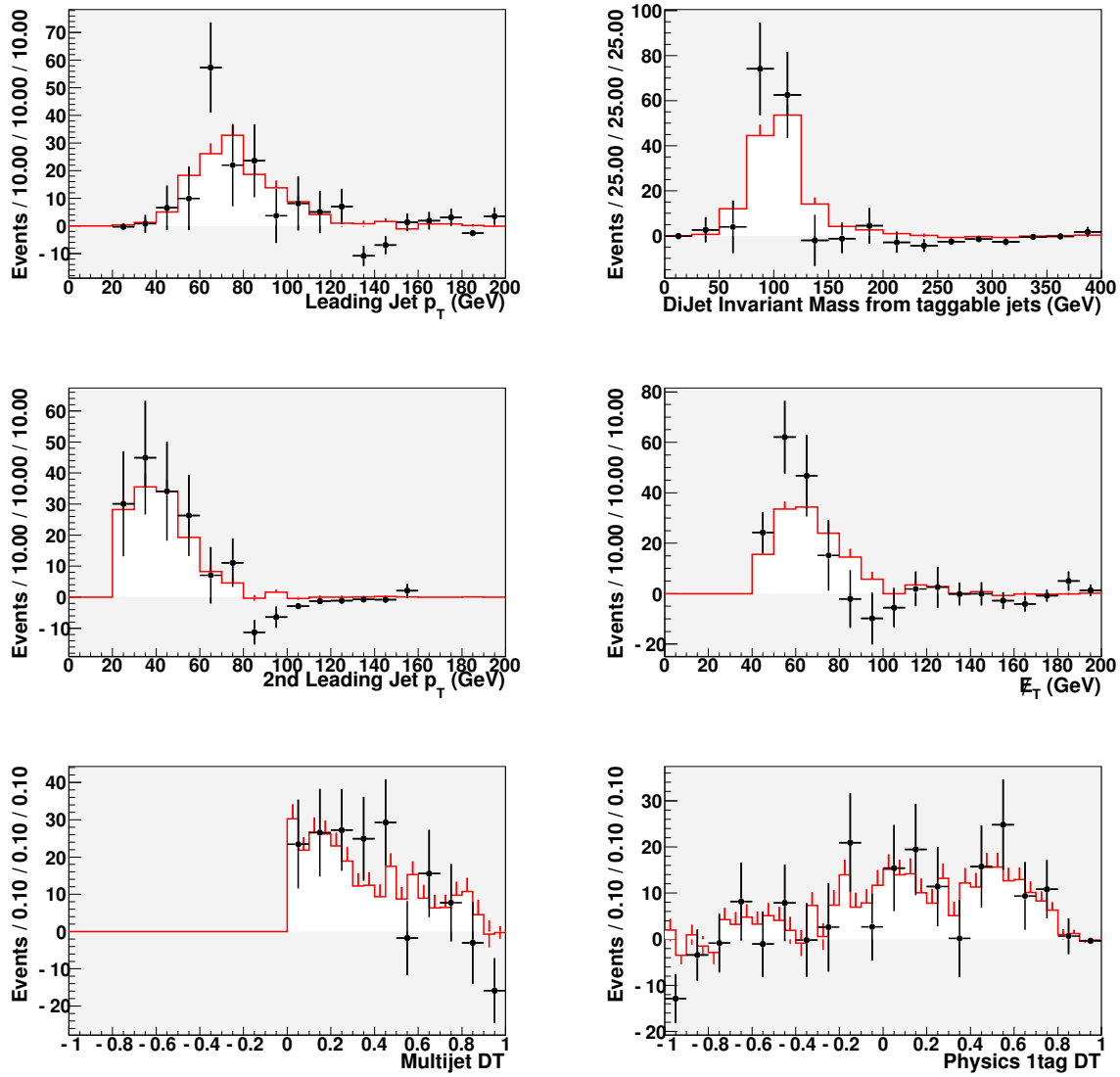## 6.8   Signal sample

The signal sample (also called analysis sample) is selected as described in Sec. 6.4. The background normalizations are obtained as explained in Sec. 6.5. To normalize the MJ-model in the signal sample after b-tagging, we use the shape of the MJ-DT before tagging and derive the scale for the tagged sample in that tagged sample.

In a later stage, we also use in this analysis the number of isolated tracks. A track is called isolated if it has a $p_T > 5$ GeV, fulfills certain quality criteria and there is no other track with $p_T > 0.5$ GeV in the hollow-cone of $0.06 < \Delta R < 0.3$ around this track. This definition of isolated tracks was devised in [45], where it was optimized for a similar jets+$\displaystyle{\not}E_T$ final state to reject $(W \to \ell\nu)$+jets events with unidentified leptons. The track quality criteria used for this definition are described in that note.

The numbers of events observed and expected from the various background sources are given in Table 6.14 before b tagging, for an exclusive VT tag, and for an asymmetric VT-L3 double tag. There is agreement between numbers of events expected and observed in the b-tagged samples, once the systematic uncertainties reported in Chapter 8 are taken into account.

Plots of various variable distributions before b-tagging can be seen in Figure 6.17 and after double asymmetric (VT-L3) tagging in Figure 6.18 Overall, there is good agreement between the observed data and the expected background, both before and after b-tagging. Additional plots including all plots for the Run IIa and single tag analysis can be found in the Appendices.

Sample	Before b-tagging		1 VT and 1 L3 tag	
ZH (115 GeV)	21.47	$\pm$ 0.08	5.93	$\pm$ 0.04
WH (115 GeV)	22.24	$\pm$ 0.12	5.76	$\pm$ 0.06
W+jets	95629.18	$\pm$ 207.85	134.49	$\pm$ 11.73
W+c+jet	5045.09	$\pm$ 52.84	36.87	$\pm$ 4.84
W+cc	8934.95	$\pm$ 52.96	86.58	$\pm$ 5.75
W+bb	3882.53	$\pm$ 21.05	345.13	$\pm$ 6.49
Z+jets	24921.97	$\pm$ 167.61	20.90	$\pm$ 8.26
Z+cc	3937.51	$\pm$ 37.02	46.21	$\pm$ 3.73
Z+bb	1855.44	$\pm$ 16.28	210.90	$\pm$ 4.89
top	2630.38	$\pm$ 6.04	423.56	$\pm$ 2.03
di-boson	2862.42	$\pm$ 17.11	44.61	$\pm$ 2.06
Total Physics	149699.50	$\pm$ 281.60	1349.25	$\pm$ 18.72
Instr. Bgrd	33507.06	$\pm$ 339.92	312.72	$\pm$ 29.18
Total Bgrd	183206.50	$\pm$ 441.41	1661.97	$\pm$ 34.67
Observed	183749		1707	

Table 6.14: RunIIb number of events after applying all analysis cuts before and after b-tagging. Errors are statistical errors only.
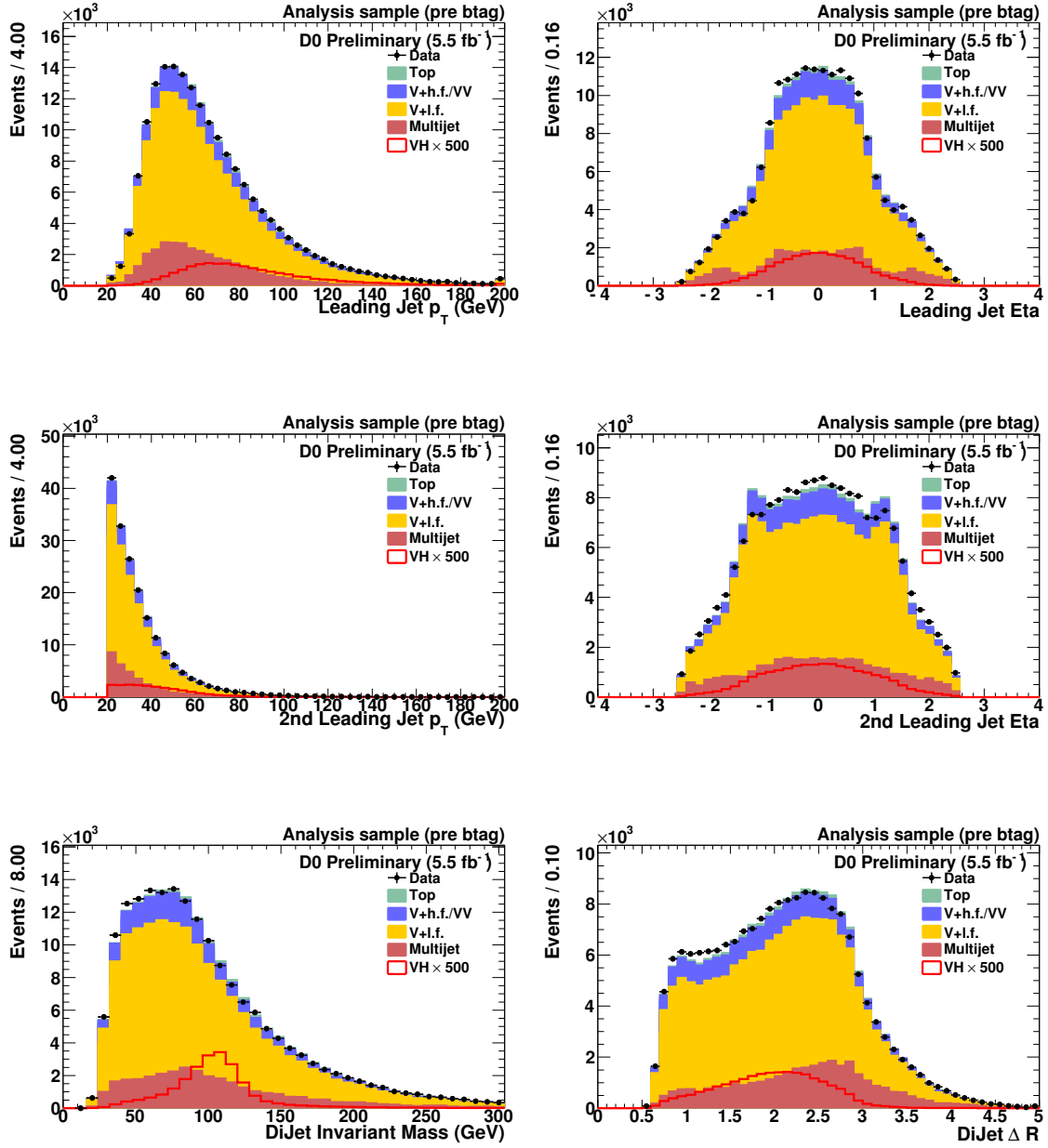
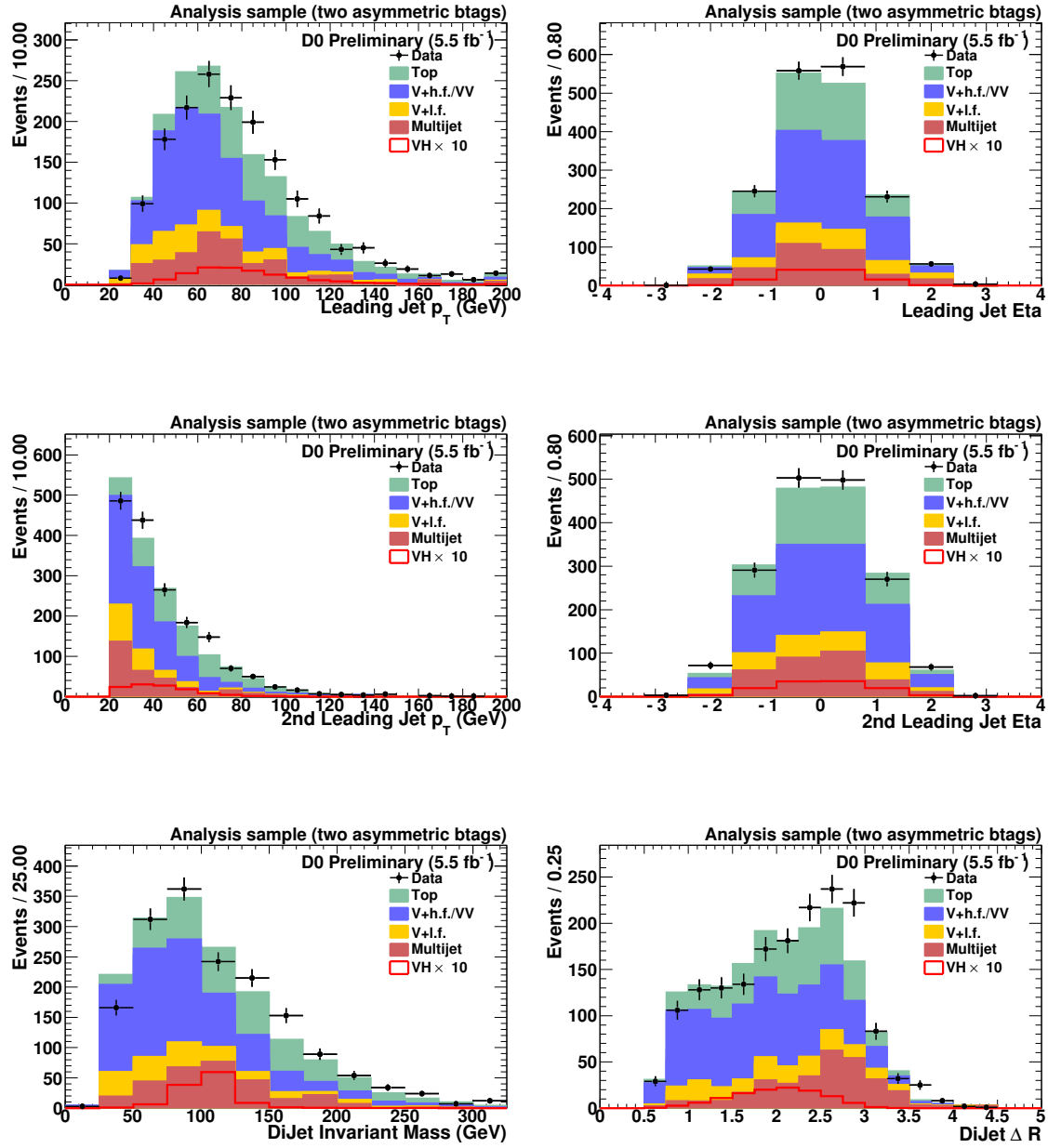Figure 6.17: Signal sample before *b*-tagging

Figure 6.18: Signal sample with one tight and one loose b-tag

Chapter 7

DECISION TREES

At this point we have a well-modeled sample that is kinematically similar to the final state of our desired Higgs process. However, the signal is still overwhelmed by background. We must now extend our analysis such that we are no longer discarding events solely based on single physical criteria. Instead, we want combinations of these criteria to best discern between a background and signal event. We optimize the ordering and values of criteria placed on variable, to best attain this discrimination. In doing so, we extend a cut based analysis to a multivariate by analyzing events they have failed certain criteria [46].

7.1   Tree construction

Mathematically, decision trees are rooted binary trees. An example is shown in Figure 7.1. Consider a training sample made of known signal and background events; they form the root node of the tree. This node, and the resulting child nodes, are continually split in an attempt to separate signal and background events. To determine the optimal splitting at each node we use the Gini index:

$$p(1 - p) \tag{7.1}$$

Where p, purity, is given by $s/(s + b)$ where s (b) is the weighted sum of signal (background) events. Since a cut which selects predominantly background is as valuable as a cut which selects signal, the criterion is symmetric with respect to the event class. The maximum is when the samples are fully mixed at a purity of 0.5. The sum of the indices of the two daughter nodes, weighted by their relative fraction of events, is less than that of the parent when the separation of the two populations has increased. The cut on the variable which maximizes this difference is chosen to split each node. Two new nodes are created, one corresponding to events satisfying the split criterion (labeled P for passed in Figure 7.1), the
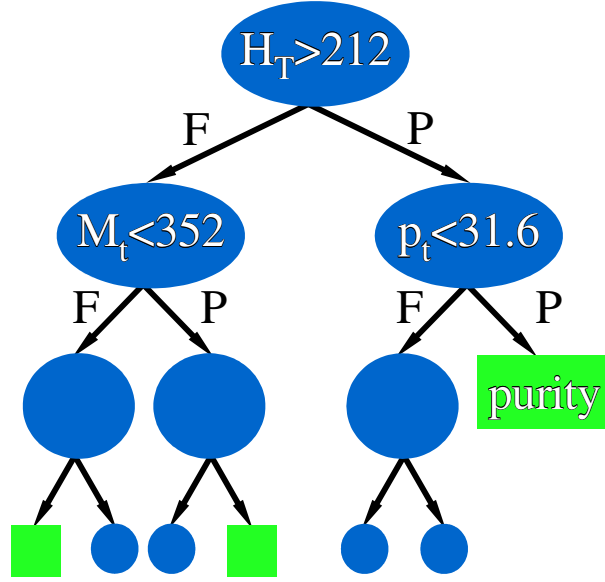
Figure 7.1: A schematic example of a Decision Tree. Nodes are shown in blue, with their associated splitting test; terminal nodes (leaves) are in green.

other containing events that failed it (labeled F). The algorithm is then applied recursively until a stop criterion, being the creation of 15 nodes, is fulfilled. A terminal node is called a leaf and labeled signal if the purity is larger than 0.5, background otherwise. The choice of a small number of nodes keeps overtraining effects at bay. Overtraining occurs when there are too few data points to properly set the model parameters; in other words, there are too many degrees of freedom. The severity of this problem depends on the machine technique used. Boosted decision trees usually suffer from at least partial overtraining, owing to their large number of nodes. The effect of overtraining is a falsely measured increase in the performance over the objectively achievable one if measured in the training sample and an effective performance decrease when measured with an independent test sample. A simple way to test for and measure the effect of overtraining is to compare the performance results between the independent training and test samples, which can be seen in Figure **??** where one-third of the analysis sample is used for training.

For this analysis, we use sets of three decision trees, one set for each Higgs boson mass. In each set, a first tree ("multijet DT") is trained to separate V+H signal from multijet

background. This tree is trained at pretag level on the multijet-model for the signal sample, and applied to the pretagged and tagged signal samples. As we aim to optimize our sensitivity in the two tag sample we only train this tree on the two taggable jet pretag sample. Two other trees ("Physics DT") are trained to separate V+H from top, V+jets, and diboson backgrounds, one at the single-tag level, and the other at the double-tag level. The various backgrounds are weighted according to their expected contributions.

Decision Tree Settings	
$N_{trees} = 200$	shrinkage $= 0.90$
Bagging fraction $= 0.6$	Gini index for separation
$N_{cuts,gini} = 20$	$N_{nodes,max} = 15$

Table 7.1: The settings for the training of the Stochastic Gradient Boosted Decision Trees

7.2 The multijet and physics decision trees

The final results are obtained using the Physics Decision Tree outputs, after a cut on the multijet Decision Tree. The multijet DT cut was optimized using the binned log likelihood ratio as described in Section 5.4.1, with result of 0.0 being chosen. The default approach is to train the Physics DT before cutting on the multijet DT. It was verified that no improvement is obtained by training the Physics DT on samples with the multijet DT cut applied.

All variables exhibit sufficient agreement in data/MC modeling. A ranking of the input variables is derived by counting how often the variables are used and by weighting each split occurrence by the separation gain-squared it has achieved and by the number of events in the node. The variables and their rankings used in the decision trees are given in Tables 7.2- 7.3.

Figure 7.2 shows the multijet DT output distribution for all Higgs boson masses at the pretag level. The multijet normalization was obtained in the signal sample before MJ-DT cut, as explained in Sec. 6.5. It is left unchanged, while the (W/Z)+jets, heavy flavor fraction, and top normalizations are re-adjusted to the jet multiplicity distributions in the

Variable	Ranking
$\not{E}_T$	0.1336
second jet p_T	0.09315
dijet mass	0.09011
$\not{H}_T / H_T$	0.07994
Transverse mass	0.06876
$\max \Delta\phi(\not{E}_T, \mathrm{jet_i}) - \min \Delta\phi(\not{E}_T, \mathrm{jet_i})$	0.06279
$\not{H}_T$	0.06239
recoil subtracted dijet $P_\perp$	0.05418
$\Delta\phi(\not{E}_T, \mathrm{jet_2})$	0.0424
$\Sigma(\mathrm{jet_2}, dijet_{higgs})$	0.04143
$cos(\theta_{Higgs})$	0.03688
leading jet p_T	0.03517
$\max \Delta\phi(\not{E}_T, \mathrm{jet_i}) + \min \Delta\phi(\not{E}_T, \mathrm{jet_i})$	0.03473
relative second jet pull $\theta_{rel,2}$	0.03449
$\Delta\phi(\mathrm{jet_1}, \mathrm{jet_2})$	0.03441
$\Delta\eta(\mathrm{jet_1}, \mathrm{jet_2})$	0.03351
relative leading jet pull $\theta_{rel,1}$	0.0293
$\Delta R(\mathrm{jet_1}, \mathrm{jet_2})$	0.02051
Number of taggable jets	0.01221

Table 7.2: Variables and rankings of inputs to the multi-jet decision tree.

Variable	Ranking
dijet mass	0.09681
$\not{H}_T / H_T$	0.08249
$\Delta R(\text{jet}_1, \text{jet}_2)$	0.06117
$\Delta \eta(\text{jet}_1, \text{jet}_2)$	0.05851
$\not{H}_T$	0.05704
$cos(\theta_{Higgs})$	0.05401
$\Delta \phi(\not{E}_T, \text{jet}_2)$	0.05353
relative second jet pull $\theta_{rel,2}$	0.05281
leading jet p_T	0.05247
$\Sigma(\text{jet}_2, dijet_{higgs})$	0.05162
$\max \Delta \phi(\not{E}_T, \text{jet}_i) - \min \Delta \phi(\not{E}_T, \text{jet}_i)$	0.05128
relative leading jet pull $\theta_{rel,1}$	0.05009
$\not{E}_T$	0.04868
recoil subtracted dijet $P_\perp$	0.04837
Transverse mass	0.04702
$\Delta \phi(\text{jet}_1, \text{jet}_2)$	0.04372
$\max \Delta \phi(\not{E}_T, \text{jet}_i) + \min \Delta \phi(\not{E}_T, \text{jet}_i)$	0.03643
second jet p_T	0.03252
Number of taggable jets	0.02144

Table 7.3: Variables and rankings of inputs to the double tag physics decision tree.

Sample	Before b-tagging		1 VT and 1 L3 tag	
ZH (115 GeV)	18.56	± 0.07	5.30	± 0.03
WH (115 GeV)	18.26	± 0.11	4.91	± 0.05
W+jets	40319.34	± 125.94	50.57	± 6.57
W+c+jet	1923.75	± 30.42	12.12	± 2.52
W+cc	4302.46	± 34.65	41.77	± 3.89
W+bb	1924.27	± 14.01	181.61	± 4.51
Z+jets	11892.16	± 112.66	7.98	± 3.70
Z+cc	2037.27	± 25.62	25.20	± 2.67
Z+bb	1002.77	± 11.65	115.37	± 3.54
top	2074.50	± 5.45	335.64	± 1.82
di-boson	1876.21	± 13.85	31.94	± 1.86
Total Physics	67352.73	± 178.58	802.19	± 11.19
Instr. Bgrd	3325.41	± 168.70	46.96	± 17.31
Total Bgrd	70678.14	± 245.66	849.15	± 20.61
Observed	70815		881	

Table 7.4: Number of events after applying all selection cuts and after cutting on the multijet-DT output, before and after b-tagging. Errors are statistical errors only.

0, 1 and 2-tag samples after the cut at 0.0 on the MJ-DT output, with results shown in Table 6.12. The physics DT output distributions are shown in Figures 7.5.

The numbers of events observed and expected from the various background sources are given in Table 7.4 after the cut at 0.0 on the multijet DT output before b tagging and for an asymmetric VT-L3 double tag. The effect of the cut on the multijet-DT output can be seen by comparing with Table 6.14.

Kinematic variable distributions after the cut at 0.0 on the multijet DT output are shown here for a Higgs boson mass of 115 GeV. Distributions before b-tagging can be seen
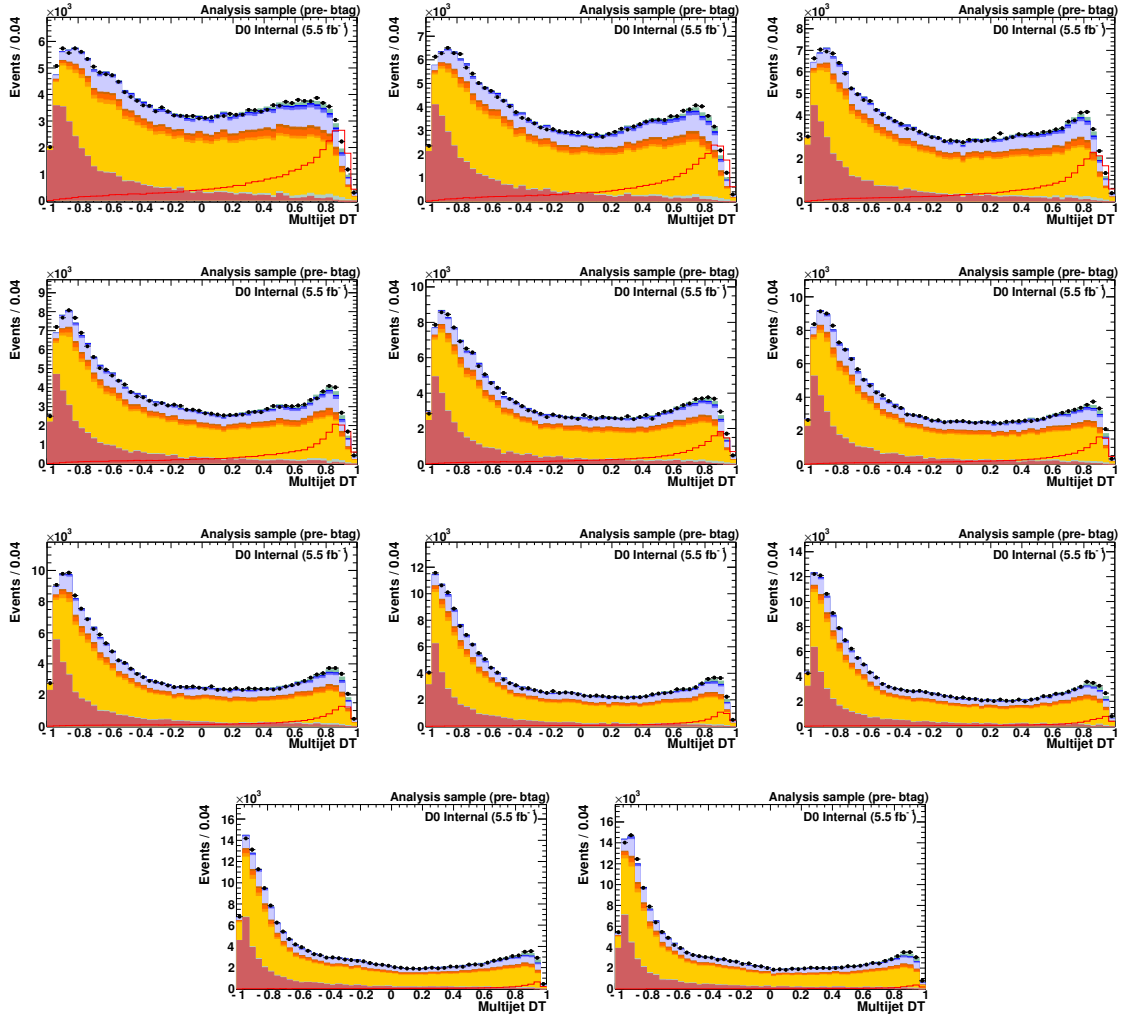
Figure 7.2: Multijet DT distribution for different Higgs masses (100-150 GeV) at the pretag level.

in Figure 7.3 and for the two-tag sample in Figs. 7.4. Overall, there is good agreement between the observed data and the expected background, both before and after b-tagging.
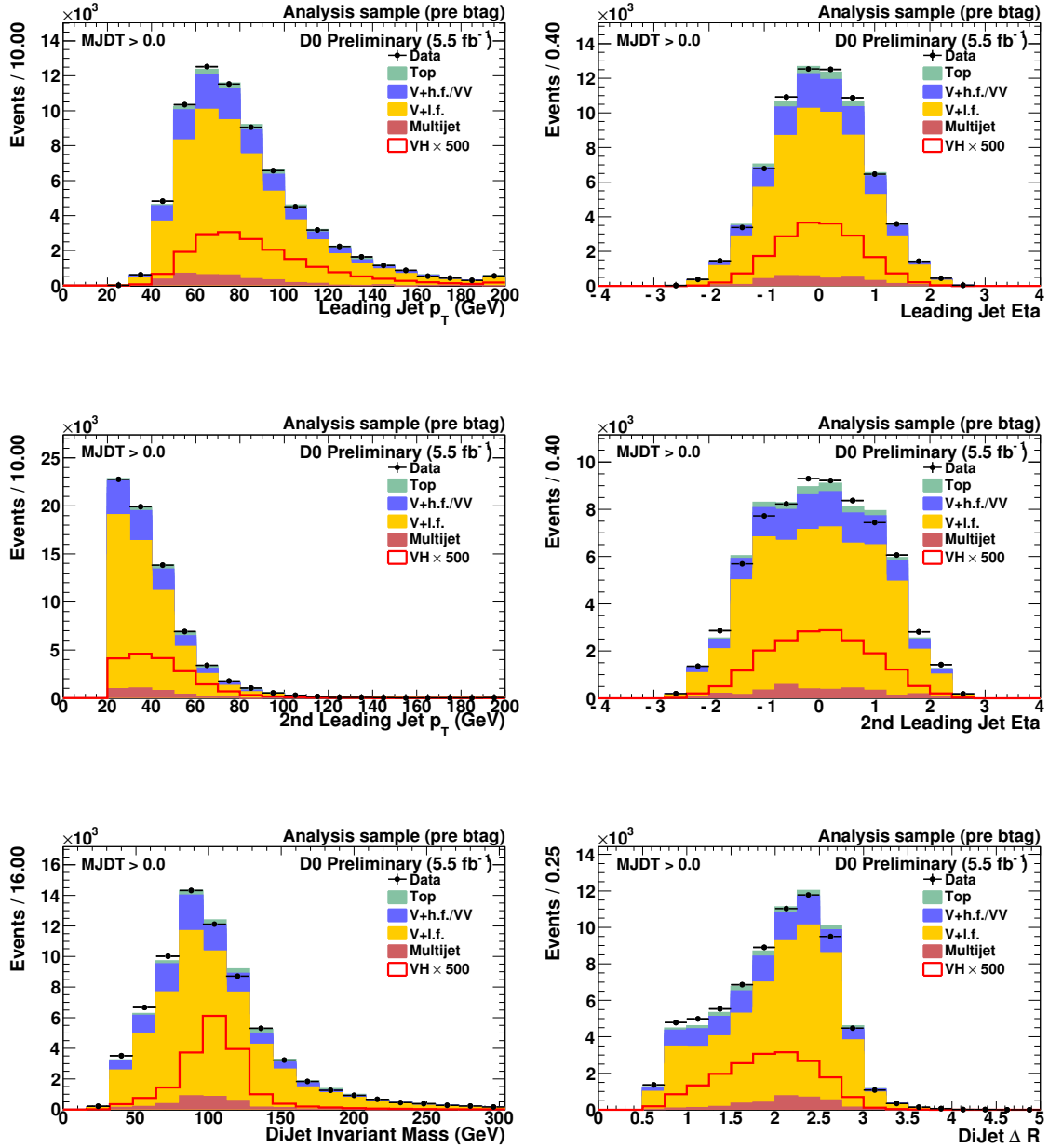
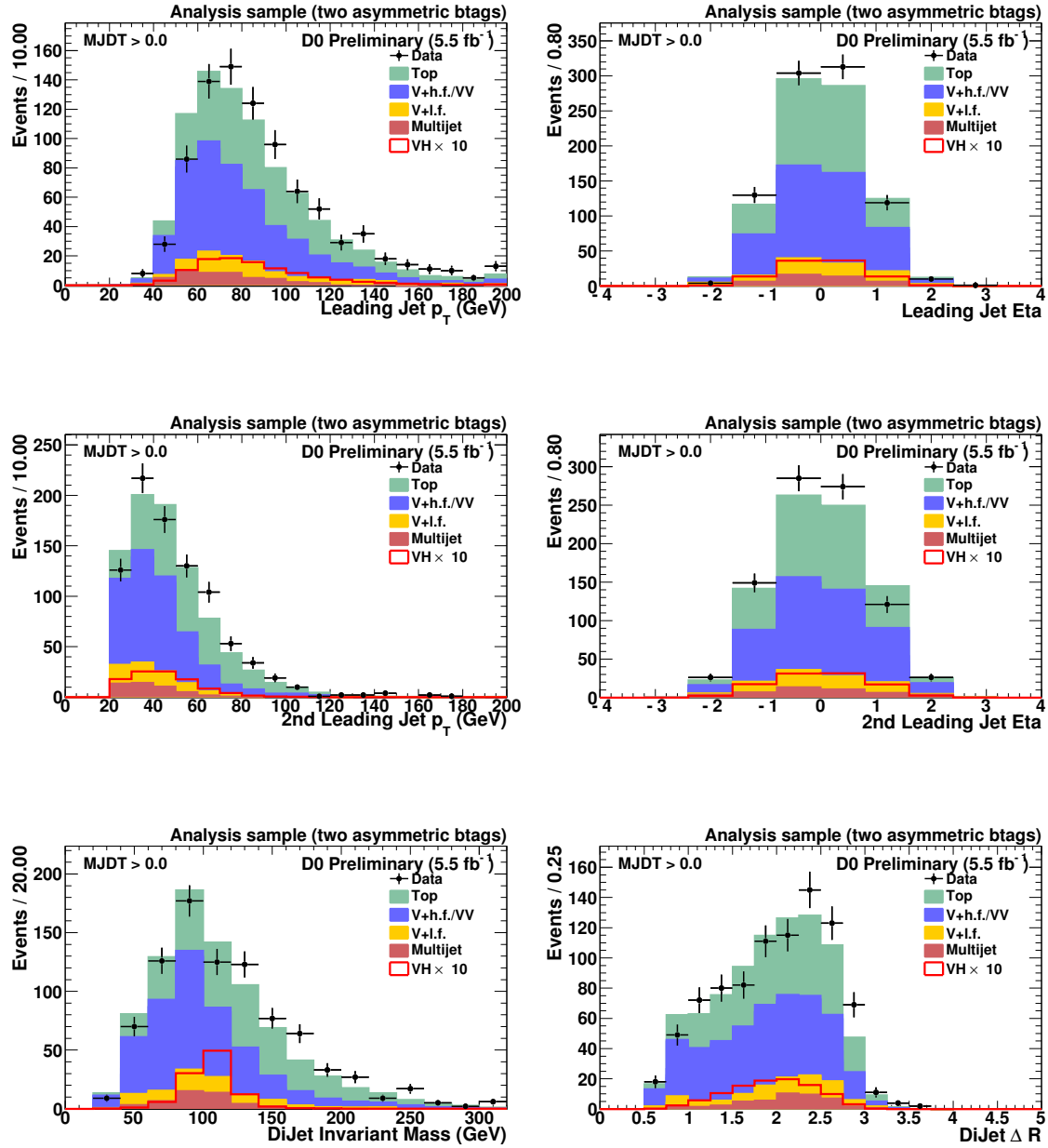Figure 7.3: Signal sample before *b*-tagging after requiring a multijet decision tree cut of $DT > 0.0$.

Figure 7.4: Signal sample with one tight and one loose b-tag after requiring a multijet decision tree cut of $DT > 0.0$.
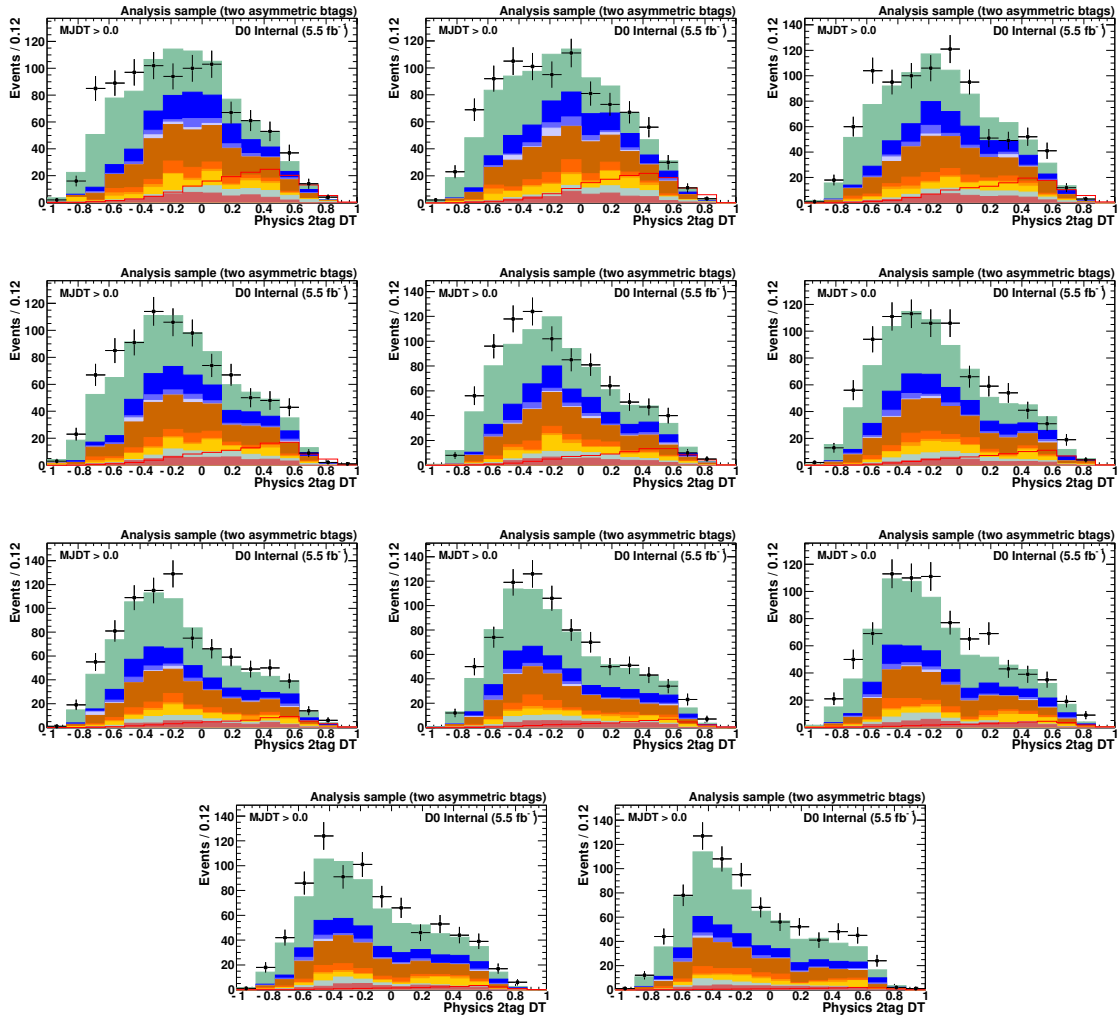
Figure 7.5: Physics DT distribution for different Higgs Masses (100-150 GeV)in the double tag sample. The multijet DT output is required to be greater than 0.0.

Chapter 8

SYSTEMATIC UNCERTAINTIES

Systematic uncertainties enter the calculation of the Higgs boson production cross-section upper limit as normalization uncertainties that only affect the expected signal and/or background yields, and as shape uncertainties that affect the distributions of the discriminant variables used to derive the results. For the discussion of the systematic uncertainties, we now speak of the entire Run II data set as most are of similar origin, but discern which effects are correlated between the two datasets, and which are not as this will effect the combination of the two epochs.

We have considered the following experimental systematic uncertainties. Since these uncertainties are largely of statistical origin, they are considered uncorrelated between the two data-taking epochs, except for lepton identification and luminosity.

- **Trigger:**

  A thorough discussion of the trigger systematic and simulation is given in [28]. There are two sources of uncertainty in the trigger. The first is how well the trigger parameterization performs on an orthogonal data sample which is tested by applying the parameterization on a $W \rightarrow \mu\nu$ data sample and comparing to the true decision. This is fit to 0.99 with 2% error. The second is how well the parameterization performs on simulation. To do this the MC is fit bin-by-bin to the data and the parameterization is then applied to both data and MC. The ratio of shapes is fit 1 with 3% error. The full systematic is sum in quadrature of these two uncertainties.

- **Jet energy scale:**

  Initial MC jet energies were shifted after modifying the JSSR shifting correction factors by $\pm 1\sigma$ of their uncertainties. The shape distortions are evaluated in the 0-tag sample, as explained in Appendix C. The same approach is used for the other jet

systematics: energy resolution, reconstruction and identification, vertex confirmation, and taggability.

- **Jet energy resolution:**

  Initial MC jet energies were smeared after modifying the JSSR smearing correction factors by $\pm 1\sigma$ of their uncertainties.

- **Jet reconstruction and identification:**

  Scale factors are used to remove MC jets to account for data/MC differences in jet reconstruction and identification efficiencies. These are varied by -1σ of their uncertainties, and the result was symmetrized.

- **Vertex confirmation and Taggability:**

  The Jet-ID group now provides combined scale factors for vertex confirmation and taggability, to account for data/MC differences in both. They are used to remove MC jets, and were varied by -1σ of their uncertainties. The result was symmetrized.

- **b tagging:**

  Flavor-dependent scale-factors provided by the b-ID group were used to weight MC events according to the flavor of the jets in the event to account for data/MC differences in efficiencies for direct tagging. These weights were varied by $\pm 1\sigma$ of their uncertainties.

- **Lepton identification:**

  Lepton identification efficiencies affect the lepton veto used in the selection of the signal sample. Muon identification efficiencies also affect the selection of the electroweak control sample. For each lepton flavor, the uncertainties associated with the various sources of inefficiency are combined in quadrature. Each of these lepton-ID efficiencies is then varied by $\pm 1\sigma$ of its uncertainty. The main sources of uncertainty are of systematic origin and are taken correlated between epochs. These are normalization-only systematic uncertainties.

- **Multijet modeling:**

  We compute the all-flavor multijet normalization in the signal sample after selection cuts, with negligible statistical uncertainty. An uncertainty comes from keeping this normalization after MJ-DT cut.

  The normalizations of the tagged multijet samples are obtained by direct tagging in the sideband. They are corrected by heavy-to-all flavor multijet ratios obtained in the high statistics multijet control sample with negligible statistical uncertainties. An uncertainty is due to the fact that we propagate these ratios to the signal sample, as well as after MJ-DT cut.

  In our final selection after MJ-DT cut, the multijet contribution is however reduced to a very small amount in the 1-tag and 2-tag samples. We assign a 25% normalization-only systematic uncertainty to this contribution, which we believe is conservative enough to cover the above effects.

- **Luminosity:**

  The error on the integrated luminosity is 6.1% [48]. This is a normalization-only systematic uncertainty, correlated across data taking epochs.

The following systematic uncertainties are of theoretical nature, and therefore correlated between epochs.

- **Cross sections:**

  The systematic uncertainties on the cross sections of the various processes involved are set as agreed in the Tevatron New Phenomena and Higgs Working Group (TEVN-PHWG) [49]. They range from 6% for signal and for the inclusive production of W/Z, to 10% for single and double top production.

- **$(W/Z)+$2-jet cross section:**

  We take as systematic uncertainty for the $(W/Z)+$2-jet cross section the difference from unity of the scale factor derived in the electroweak control sample, i.e., 10%,

from which we subtract in quadrature the 6% assigned to the total W/Z production cross section, which results in 8%.

- **Heavy flavor ratio:**

  The uncertainty on the $(W/Z)b\bar{b}$ and $(W/Z)c\bar{c}$ cross sections is calculated within MCFM to be +19/-18% [50]. We assign a 20% uncertainty on the ratio of heavy to light flavor production.

- **ALPGEN parameters uncertainties:**

  Uncertainties arise in ALPGEN from the choice of MLM matching p_T threshold, the choice of MLM clustering radius, and from two scaling parameters, the $k_\perp$- and Q-factor. These are combined into two independent shape-only uncertainties: related to the MLM algorithm and related to the light and heavy flavor scaling parameters. The MLM algorithm uncertainty is only applied to V+jets samples with light flavor jets.

- **ALPGEN angular reweighting:**

  As described in Appendix D, a reweighting was derived in the electroweak control sample to correct generator level imperfections. Half of the difference between the unweighted and reweighted distribution was symmetrized to obtain the $\pm 1\sigma$ uncertainty. This is a shape only uncertainty.

- **Underlying event and fragmentation modeling:**

  From studies of the impact on the dijet mass of various PYTHIA tunes and of the comparison of ALPGEN interfaced with PYTHIA and with HERWIG, a shape-only systematic uncertainty is applied to all V+jets samples as recommended in Ref. [51].

- **PDF Uncertainty:**

  The signal acceptance and modeling is sensitive to the PDFs used in generation. To assess the impact of the uncertainties on these PDFs, a re-weighting is used. The signal has been generated using CTEQ6L1 PDF, but to assess the PDF uncertainty we perform a per-event re-weighting (based on the properties of the incoming partons)

to CTEQ6.1M and the 20 pairs of associated error sets. Figure 8.1 shows the size and shape of each of the 20 pairs. We take all the available sets for the shape systematic. For the final shape uncertainty we take the the largest pair of uncertainties for signal and background separately. We have determined these to be pair 9-10 for signal and 15-16 for backgrounds. Variations of the nominal distributions are required to preserve the normalization as normalization changes are accounted for in the cross section uncertainty.

The extent of the systematic correlations are shown in Table 8.1. For each source of systematic uncertainty, the samples which are subject to this uncertainty and the extent of the correlation, if any, are explicitly shown.

Tables 8.4-8.5 summarize all normalization systematic uncertainties in the p20 analysis evaluated for SM background expectations and for signal efficiencies. The signal is evaluated for a Higgs-boson mass of $m_H = 115$ GeV, summing the $ZH \to \nu\overline{\nu}b\overline{b}$ and $WH \to \ell^{\pm}\nu b\overline{b}$ contributions. The $t\overline{t}$ and single top contributions are added together as well.
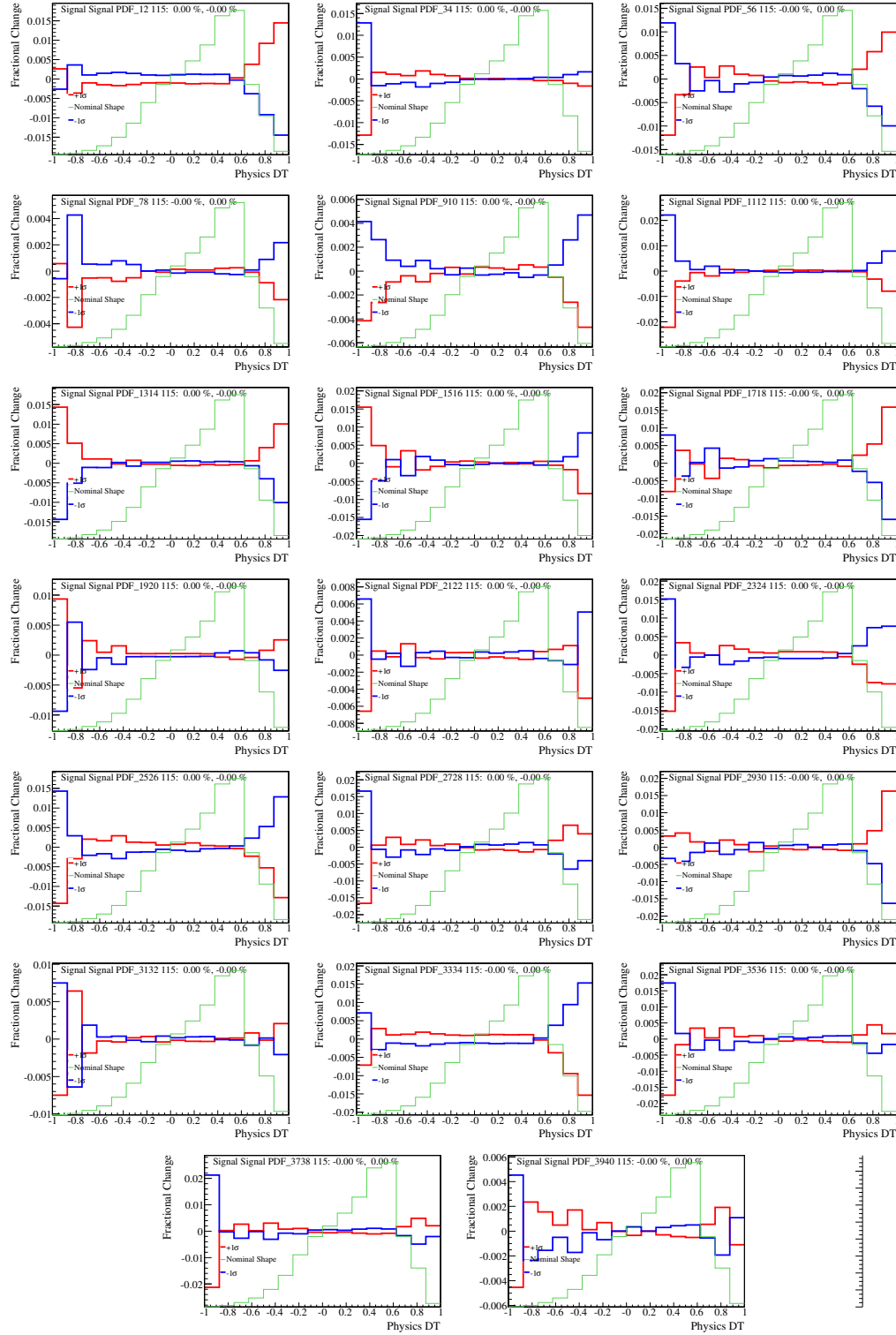
Figure 8.1: PDF uncertainties on the signal in the 2 tag channel, for a Higgs boson mass of 115 GeV. These are shape only uncertainties as the normalization uncertainty is accounted for in the cross section error.

Systematic Uncertainty	COLLIE Tag	Type	Sample	Correlated
σ_{ZH}	XS_ZH	Flat Norm	S	Full
Jet Energy Scale	JES	Shape & Norm	B & S	Within Epoch
Jet Reco*ID	EFF	Shape & Norm	B & S	Within Epoch
Jet Resolution	RES	Shape & Norm	B & S	Within Epoch
$\sigma_{Diboson}$	Bkgd_XS_EW	Flat Norm	Diboson	Full
σ_{Top}	Bkgd_XS_Top	Flat Norm	Top	Full
σ_{V+Jets}	V+jets	Flat Norm	$(W/Z) + Jets$	Full
σ_{V+hf}	V+hf	Flat Norm	$(W/Z) + hf$	Full
Vp_T reweighting	V+jets	Flat Norm	$(W/Z) + Jets$	Full
Mulit-jet Normalization	MJ	Flat Norm	Mulit-jet	None
Parton Distribution Functions	PDF	Shape	B & S	Full
Vertex Conf./ Taggability	TAG	Shape & Norm	B & S	Within Epoch
B-Tagging HF Rate	btagHF	Shape & Norm	B & S	Within Epoch
B-Tagging LF Fake Rate	btagLF	Shape & Norm	B & S	Within Epoch
Trigger Simulation	TRIG_D_MC	Shape & Norm	B & S	Within Epoch
μ ID	MUID	Flat Norm	B & S	Full
EM ID	EMID	Flat Norm	B & S	Full
Alpgen MLM	ALPGEN_MLM	Shape	$V + lf$	Full
Alpgen Event Scale	ALPGEN_S	Shape	$V + Jets$	Full
Alpgen Underlying Event	ALPGEN_UE	Shape	$V + Jets$	Full
Alpgen Angular RW	ALPGEN_RW	Shape	$V + Jets$	Full
Luminosity	Luminosity	Flat Norm	B & S	Full

Table 8.1: Table of correlations among systematics; B denotes all Monte Carlo backgrounds, S denotes signal, $Full$ denotes correlations across data taking epochs. The uncertainties affecting both W+jets and Z+jets are correlated between the two processes.

	$\sum$ Bkgd	signal	Top	Diboson
Jet energy scale	3.9/ 3.5	3.5/ -2.6	-0.7/ 0.1	5.9/ -5.7
Jet resolution	1.8/ 1.2	-0.2/ 0.4	-0.4/ -0.2	1.5/ -0.9
*Jet reco*ID*	$\mp$ 0.3	$\pm$ 0.6	$\mp$ 4.1	$\pm$ 1.1
Direct taggability	$\pm$ 2.8	$\pm$ 4.2	$\pm$ 0.3	$\pm$ 4.3
MC b-tag Heavy Flavor	3.2/ 3.4	-0.3/ -1.1	3.4/ -3.9	3.5/ -3.8
MC b-tag Light Flavor	$\pm$ 0.9	$\mp$ 0.1	$\mp$ 0.2	$\pm$ 0.6
Trigger	$\pm$ 1.7	$\pm$ 0.8	$\pm$ 1.2	$\pm$ 2.5
Electron identification	$\pm$ 0.3	$\pm$ 0.4	$\pm$ 0.6	$\pm$ 0.3
Muon identification	$\pm$ 1.0	$\pm$ 0.9	$\pm$ 1.8	$\pm$ 0.9
Heavy-flavor fractions	$\pm$ 8.9	–	–	–
Cross section	$\pm$ 7.3	$\pm$ 6.0	$\pm$ 10.0	$\pm$ 7.0
Luminosity	$\pm$ 6.1	$\pm$ 6.1	$\pm$ 6.1	$\pm$ 6.1
	Z+lf	Z+hf	W+lf	W+hf
Jet energy scale	6.8/ -5.0	6.1/ -4.5	6.7/ -6.4	$\pm$ 5.2
Jet resolution	3.5/ -2.2	2.1/ -0.9	4.5/ -1.8	2.4/ -2.3
*Jet reco*ID*	$\pm$ 1.1	$\pm$ 1.0	$\pm$ 1.3	$\pm$ 1.1
Direct taggability	$\pm$ 4.5	$\pm$ 4.2	$\pm$ 4.4	$\pm$ 3.7
Vertex confirmation	–	–	–	–
MC b-tag Heavy Flavor	$\pm$ 0.3	3.8/ -4.2	$\pm$ 2.7	3.8/ -4.1
MC b-tag Light Flavor	$\pm$ 8.3	$\mp$ 0.1	$\pm$ 3.6	–
Trigger	$\pm$ 2.0	$\pm$ 2.2	$\pm$ 1.6	$\pm$ 2.1
Electron identification	–	–	$\pm$ 0.1	$\pm$ 0.6
Muon identification	$\pm$ 0.1	$\pm$ 0.1	$\pm$ 0.6	$\pm$ 1.6
Heavy-flavor fractions	–	$\pm$ 20.0	–	$\pm$ 20.0
Cross section	$\pm$ 6.3	$\pm$ 6.3	$\pm$ 6.3	$\pm$ 6.3
Luminosity	$\pm$ 6.1	$\pm$ 6.1	$\pm$ 6.1	$\pm$ 6.1

Table 8.2: Relative systematic uncertainties (in %) on SM background expectations and on the ZH/WH signal ($m_H = 115$ GeV) for the RunIIa single tag analysis. Shape-only systematic uncertainties are omitted. Shape dependent errors are in *italic* and the quoted numbers are just the integral values to give an order estimate. The normalization uncertainity on the multijet background is included in the cross section catagory for the total background.

	$\sum$ Bkgd	signal	Top	Diboson
Jet energy scale	3.3/ 3.1	3.6/ -3.1	-0.8/ 0.2	6.9/ -6.5
Jet resolution	1.3/ 1.1	-0.8/ 1.2	-0.3/ -0.1	1.9/ -1.1
Jet reco*ID	$\mp$ 1.0	$\pm$ 0.6	$\mp$ 4.5	$\pm$ 1.2
Direct taggability	$\pm$ 2.7	$\pm$ 4.1	$\pm$ 0.4	$\pm$ 4.5
MC b-tag Heavy Flavor	$\pm$ 7.4	$\pm$ 7.6	$\pm$ 8.2	$\pm$ 7.1
MC b-tag Light Flavor	$\pm$ 1.2	$\pm$ 0.1	$\pm$ 0.5	$\pm$ 1.1
Trigger	$\pm$ 1.9	$\pm$ 0.2	$\pm$ 1.4	$\pm$ 2.3
Electron identification	$\pm$ 0.4	$\pm$ 0.3	$\pm$ 0.8	$\pm$ 0.1
Muon identification	$\pm$ 1.5	$\pm$ 0.8	$\pm$ 1.8	$\pm$ 0.7
Heavy-flavor fractions	$\pm$ 10.2	–	–	–
Cross section	$\pm$ 8.6	$\pm$ 6.0	$\pm$ 10.0	$\pm$ 7.0
Luminosity	$\pm$ 6.1	$\pm$ 6.1	$\pm$ 6.1	$\pm$ 6.1
	Z+lf	Z+hf	W+lf	W+hf
Jet energy scale	6.0/ -8.2	6.2/ -4.3	7.2/ -7.8	5.0/ -5.2
Jet resolution	5.5/ -2.0	1.9/ -0.8	3.4/ -2.4	2.4/ -2.5
Jet reco*ID	$\pm$ 0.6	$\pm$ 1.2	$\pm$ 1.3	$\pm$ 1.1
Direct taggability	$\pm$ 3.7	$\pm$ 4.2	$\pm$ 4.6	$\pm$ 3.8
MC b-tag Heavy Flavor	$\pm$ 0.7	$\pm$ 7.6	$\pm$ 2.0	$\pm$ 7.2
MC b-tag Light Flavor	14.2/-13.3	$\pm$ 0.5	10.3/ -9.9	$\pm$ 0.8
Trigger	$\pm$ 3.1	$\pm$ 2.2	$\pm$ 2.3	$\pm$ 2.2
Electron identification	–	–	$\pm$ 0.2	$\pm$ 0.3
Muon identification	$\pm$ 7.8	$\pm$ 1.1	–	$\pm$ 1.7
Heavy-flavor fractions	–	$\pm$ 20.0	–	$\pm$ 20.0
Cross section	$\pm$ 6.3	$\pm$ 6.3	$\pm$ 6.3	$\pm$ 6.3
Luminosity	$\pm$ 6.1	$\pm$ 6.1	$\pm$ 6.1	$\pm$ 6.1

Table 8.3: Relative systematic uncertainties (in %) on SM background expectations and on the ZH/WH signal ($m_H = 115\,$GeV) for the RunIIa double tag analysis. Shape-only systematic uncertainties are omitted. Shape dependent errors are in *italic* and the quoted numbers are just the integral values to give an order estimate. The normalization uncertainty on the multijet background is included in the cross section catagory for the total background.

	$\sum$ Bkgd	signal	Top	Diboson
Jet energy scale	± 4.2	± 1.9	∓ 1.5	± 5.5
Jet resolution	± 2.2	∓ 0.7	∓ 0.6	± 0.5
Jet reco*ID	± 0.5	± 0.7	∓ 0.8	± 1.1
Direct taggability	1.3/ 4.3	1.9/ -0.0	0.5/ -0.1	1.6/ 3.7
MC b-tag Heavy Flavor	± 3.1	± 1.2	± 3.9	± 4.2
MC b-tag Light Flavor	± 4.3	–	∓ 0.1	± 3.7
Trigger	± 3.3	± 3.5	± 3.5	± 3.5
Electron identification	± 0.2	± 0.2	± 0.5	± 0.3
Muon identification	± 1.3	± 1.0	± 1.9	± 1.1
Heavy-flavor fractions	± 8.0	–	–	–
Cross section	± 6.6	± 6.0	± 10.0	± 7.0
Luminosity	± 6.1	± 6.1	± 6.1	± 6.1
	Z+lf	Z+hf	W+lf	W+hf
Jet energy scale	± 6.7	± 5.1	± 7.7	± 6.2
Jet resolution	± 3.3	± 2.5	± 4.5	± 3.0
Jet reco*ID	± 1.1	± 0.6	± 1.1	± 1.0
Direct taggability	2.6/ 24.8	1.4/ 0.5	1.8/ 11.8	1.7/ 0.6
MC b-tag Heavy Flavor	± 0.2	± 4.1	± 2.2	± 3.9
MC b-tag Light Flavor	± 24.8	± 0.5	± 11.8	± 0.6
Trigger	± 3.5	± 3.5	± 3.5	± 3.5
Electron identification	–	–	± 0.1	± 0.3
Muon identification	± 1.1	± 0.4	± 1.1	± 1.9
Heavy-flavor fractions	–	± 20.0	–	± 20.0
Cross section	± 6.3	± 6.3	± 6.3	± 6.3
Luminosity	± 6.1	± 6.1	± 6.1	± 6.1

Table 8.4: Relative systematic uncertainties (in %) on SM background expectations and on the ZH/WH signal ($m_H = 115$ GeV) for the Run IIb single tag analysis. Shape-only systematic uncertainties are omitted and. Shape dependent errors are in *italic* and the quoted numbers are just the integral values to give an order estimate.

	$\sum$ Bkgd	signal	Top	Diboson
Jet energy scale	$\pm$ 3.3	$\pm$ 1.6	$\mp$ 0.5	$\pm$ 5.1
Jet resolution	$\pm$ 0.1	$\mp$ 1.6	$\mp$ 2.0	$\mp$ 1.6
*Jet reco*ID*	$\pm$ 0.6	$\pm$ 1.1	$\pm$ 0.1	$\pm$ 1.1
Direct taggability	6.2/ 0.6	8.3/ –	5.2/ 0.1	7.4/ 1.5
MC b-tag Heavy Flavor	$\pm$ 8.6	$\pm$ 9.9	$\pm$ 10.2	$\pm$ 8.0
MC b-tag Light Flavor	$\pm$ 0.6	–	$\pm$ 0.1	$\pm$ 1.5
Trigger	$\pm$ 3.3	$\pm$ 3.5	$\pm$ 3.5	$\pm$ 3.5
Electron identification	$\pm$ 0.5	$\pm$ 0.3	$\pm$ 0.8	$\pm$ 0.3
Muon identification	$\pm$ 1.2	$\pm$ 1.1	$\pm$ 1.8	$\pm$ 1.0
Heavy-flavor fractions	$\pm$ 8.4	–	–	–
Cross section	$\pm$ 7.8	$\pm$ 6.0	$\pm$ 10.0	$\pm$ 7.0
Luminosity	$\pm$ 6.1	$\pm$ 6.1	$\pm$ 6.1	$\pm$ 6.1
	Z+lf	Z+hf	W+lf	W+hf
Jet energy scale	$\pm$ 8.5	$\pm$ 7.1	$\pm$ 8.1	$\pm$ 5.9
Jet resolution	$\pm$ 7.7	$\pm$ 2.0	$\pm$ 5.6	$\pm$ 1.0
*Jet reco*ID*	$\pm$ 1.8	$\pm$ 1.2	$\pm$ 0.8	$\pm$ 0.7
Direct taggability	3.8/ 9.3	9.1/ 0.3	4.7/ 4.4	7.4/ 0.3
MC b-tag Heavy Flavor	$\pm$ 0.2	$\pm$ 9.5	$\pm$ 2.9	$\pm$ 8.9
MC b-tag Light Flavor	$\pm$ 9.3	$\pm$ 0.3	$\pm$ 4.4	$\pm$ 0.3
Trigger	$\pm$ 3.5	$\pm$ 3.5	$\pm$ 3.5	$\pm$ 3.5
Electron identification	–	–	$\pm$ 0.3	$\pm$ 0.6
Muon identification	$\pm$ 1.8	$\pm$ 0.4	$\pm$ 0.4	$\pm$ 1.2
Heavy-flavor fractions	–	$\pm$ 20.0	–	$\pm$ 20.0
Cross section	$\pm$ 6.3	$\pm$ 6.3	$\pm$ 6.3	$\pm$ 6.3
Luminosity	$\pm$ 6.1	$\pm$ 6.1	$\pm$ 6.1	$\pm$ 6.1

Table 8.5: Relative systematic uncertainties (in %) on SM background expectations and on the ZH/WH signal ($m_H = 115\,\text{GeV}$) for the Run IIb two asymmetric tags analysis. Shape-only systematic uncertainties are omitted. Shape dependent errors are in *italic* and the quoted numbers are just the integral values to give an order estimate.
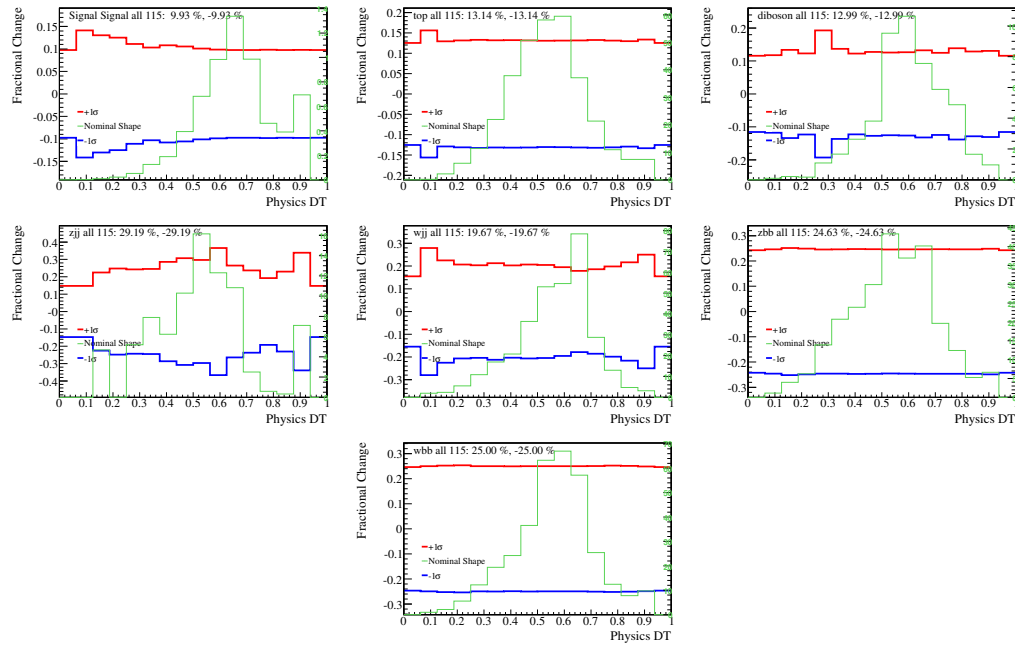
Figure 8.2: All systematic errors with respect to the nominal boosted decision tree discriminant in RunIIb for the one tag sample.
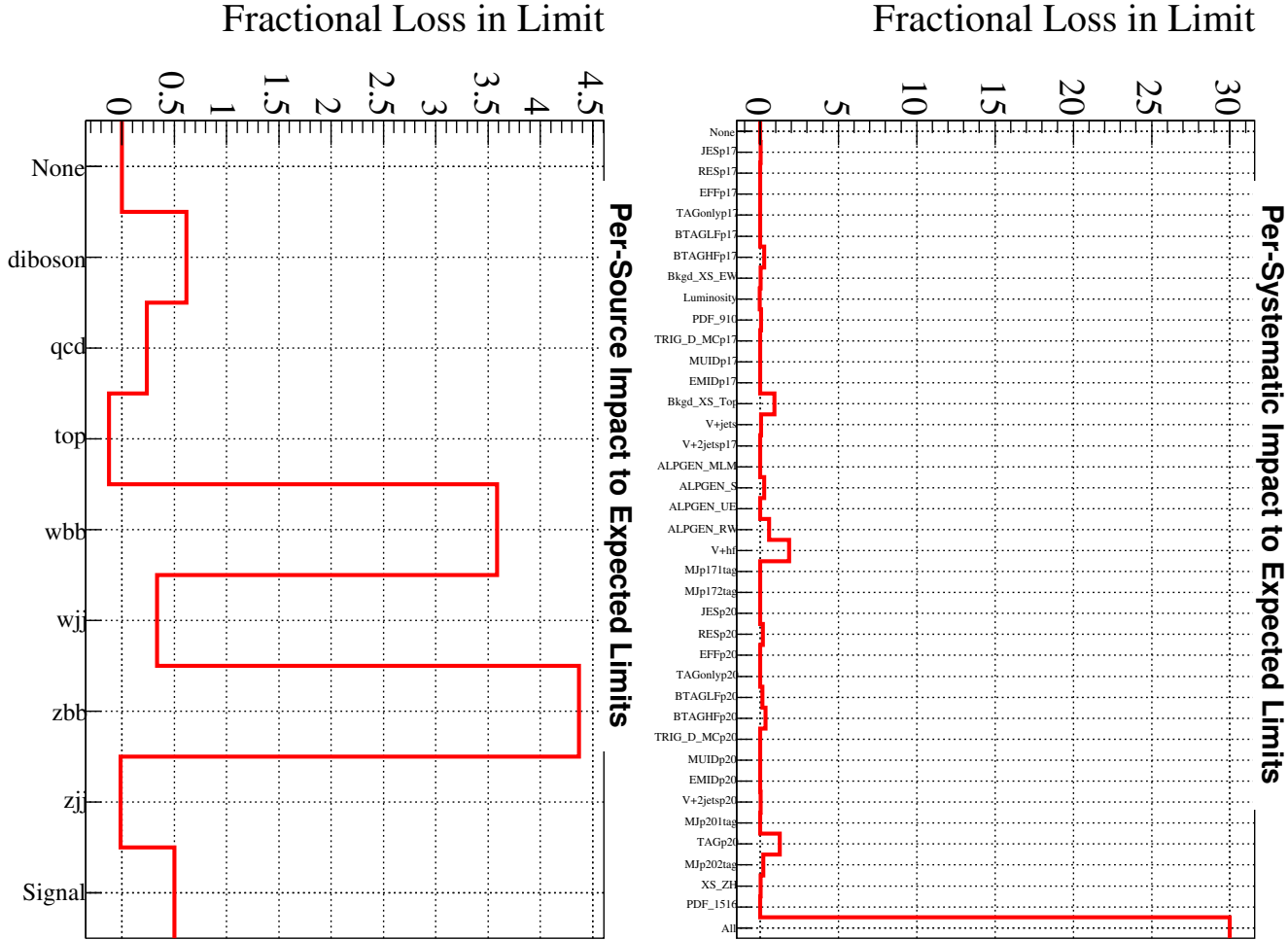
Figure 8.3: Showing the fractional loss in the final limit by removing one systematic (left) and background source (right)
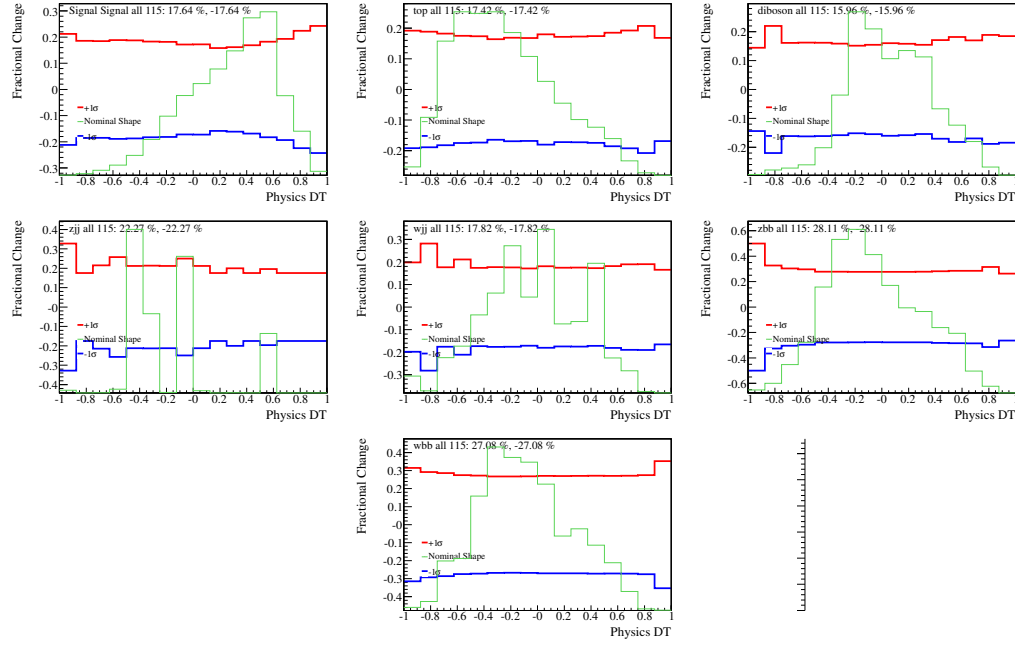
Figure 8.4: All systematic errors with respect to the nominal boosted decision tree discriminant in RunIIb for the two tag sample.
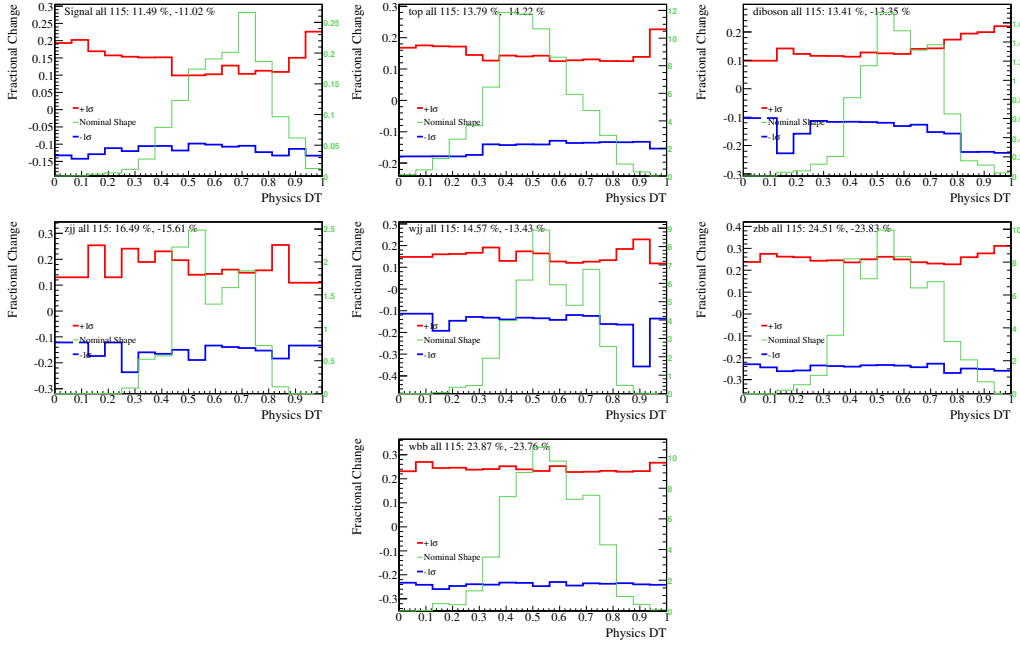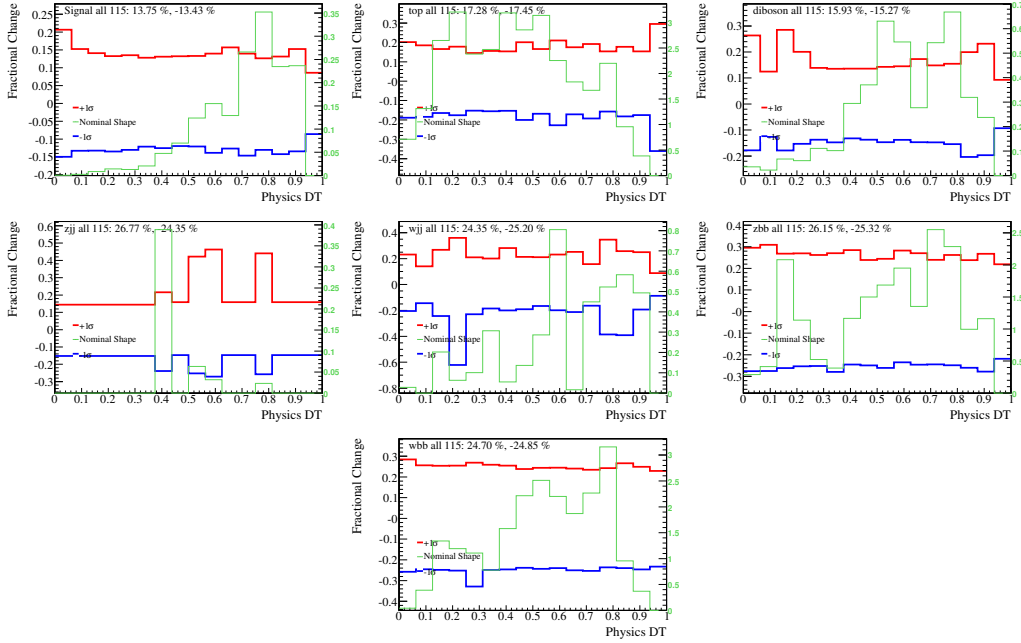
Figure 8.5: All systematic errors with respect to the nominal boosted decision tree discriminant in RunIIa for the one tag sample.

Figure 8.6: All systematic errors with respect to the nominal boosted decision tree discriminant in RunIIa for the two tag sample.

Chapter 9

UPPER LIMITS ON $ZH \to \nu\overline{\nu}b\overline{b}$ AND $WH \to \ell^{\pm}\nu b\overline{b}$ PRODUCTION

We use the COLLIE package [52] to derive expected and observed upper limits on combined $ZH \to \nu\overline{\nu}b\overline{b}$ and $WH \to \ell^{\pm}\nu b\overline{b}$ production, for Higgs-boson masses ranging from 100 to 150 GeV, with a 5 GeV increment. The inputs to the limit calculation are the physics-DT outputs, after requiring a multijet-DT output greater than 0.0. Limits are calculated for the Run IIa and Run IIb epochs separately, and for the full dataset, as well as for the single and double-tag samples separately, and for both samples combined. Systematic uncertainties are correlated across data taking epochs and across single and double-tag samples as detailed in Chapter 8.

9.1 Limit Setting Procedure

COLLIE stands for COnfidence Level LImit Evaluator. To interpret the presentation of final results of the search, it is best to define all parameters used as the lexicon of statistics in physics experiments is quite varied. We define here

- Null Hypothesis: A Null hypothesis is a model of a control or truth sample. For our purposes it is the background (Standard Model) model contributions in which there is no new physics. We refer to this as the background (b) only hypothesis.

- Test Hypothesis: This is the hypothesis that contains the new physics that is being searched for. It contains all of the standard model backgrounds plus the contributions from the various associated higgs production channels being considered. We refer to this as signal plus background ($s + b$) hypothesis.

- Confidence Level: A confidence level (CL) is a statement to the belief that a confidence range contains the true value of the parameter. For a typical Gaussian uncertainty of

a parameter, expressed as σ, a range of $-\sigma < P < +\sigma$ is believed to have the true value at 68% CL. Likewise, a range of $-2\sigma < P < +2\sigma$ is believed to have the value at 95% CL. A 95% CL is the typical hallmark for Higgs searches.

Essentially, we test whether our data is best represented by the null hypothesis or the test hypothesis. To do so we construct a test statistic that can reliably discern between the two hypotheses. For this analysis the test statistic is the Poisson Log Likelihood ratio. A Poisson distribution can be used to model events that happen randomly but at a definite average rate [53]. This describes our experiment in which only 0.0001% of events make it through our preselection cuts, but pass a constant rate nonetheless. We treat our two hypotheses as Poisson counting experiments and using the actual data events we can construct a likelihood ratio. A Poisson distribution is given as

$$P(\nu) = e^{-mu}\frac{\mu^{\nu}}{\nu!} \tag{9.1}$$

with

$$\bar{\nu} = \Sigma_i P(\nu) = \mu. \tag{9.2}$$

Here the Poisson distribution is characterized by μ, which in this case we treat as a hypothesis. To compare the to hypothesis, we take a ratio of the two Poission distributions representing the two hypotheses:

$$Q = \prod_{j=1}^{bins} \frac{P(d|s+b)}{P(d|b)} = \prod_{i=1}^{bins} \frac{e^{-(s_i+b_i)}(s_i+b_i)^{d_i}/d_i}{e^{-(b_i)}(+b_i)^{d_i}/d_i}. \tag{9.3}$$

Here, d is the actual data measurement. We mathematically compact the likelihood by taking the log of the ratio (LLR)

$$\Gamma = -2\ln(Q) = 2\sum_{i}^{bins}(s_i - d_i\ln(1 + \frac{s_i}{b_i})). \tag{9.4}$$

Now we have described the log-likelihood of a single counting experiment. In order to determine its significance we must rerun the experiment many times. Unfortunately, due to budgetary constraints and biological limitations, it is not possible to run the DØ experiment

a sufficient number of times to secure statistical significance. Using the properties of the Poisson distribution, we can take stochastic variations of the Poisson distribution parameters of our background and signal to simulate individual runs of the experiment.

However, our models are subject to a number of non-interesting parameters that are studied as background or signal, but effect the distribution of the interesting parameters. These are called *nuisance* parameters. In this analysis we call the nuisance parameters the systematic uncertainties. Collie takes as input these systematics varied by $\pm 1\sigma$, and then treats the distribution of the systematic as Gaussian. To generate a simulation of running the entire experiment, a *pseudoexperiment*, we take these uncertainties and randomly fluctuate them according to their Gaussian distribution. This prediction is further fluctuated by Poisson statistics to reproduce *pseudodata d*. The LLR is then evaluated for each of the hypotheses. The further the separation between the distributions of the LLR for the two hypotheses represents the sensitivity to our experiment. Figure 9.1 shows a sample distribution of the likelihoods for many pseudoexperiments.

The maximum of the null hypothesis yields the expected LLR for the background only hypothesis, and similarly for the Test hypothesis with the signal sample. From the symmetry of the LLR, we expect the means to be symmetric about zero, with Test hypotheses being negative and the null being positive. If we plot the LLR as a function of Higgs mass, and include the one and two sigma bands from the null hypothesis distributions we can get a very good feel of the power of this statistic. If the observed LLR lies more than $+2\sigma$ away from the expected background LLR, then there is significant reason to expect the background is not well modeled. signal.We can take the width between the means, then as an expected sensitivity of the llr to the signal.

In Figure 9.1 we take CL_{SB} to be the probability of the test hypothesis to be more background like than the data observation. CL_B is a measure of the NULL hypothesis to be, in effect, be more mackground like tha the data observation. We set the confidence level on the signal simulation by taking the ratio of these two

$$CL_S = \frac{CL_{SB}}{CL_B} \tag{9.5}$$

The confidence level is a measure of the overlap of the two hypotheses in the more background like phase space of pseudoexperiments. It is set as $1 - \alpha$ with $CL_S < \alpha$. Using CL_S in this manner protects agains large downward fluctuations in the data prediction as the ratio is less sensitive to absolute scale of the measurement. Otherwise this downward fluctuation could give a false exclusion. If a significant signal excess is observed, then $1 - CL_B$ can be used to set the one-sided gaussian Confidence level.

9.2 Results

In determining the results we are the DT disciminant as the final variable. We perform an evaluation of the confidence level for each mass of the Higgs boson using the same background but changing the simulated signal. Each BDT is trained for each tagging point at each mass so while the background events may be the same, the decision on whether they pass or fail a certain criterion may vary. We combine the discriminates of the two tagged samples in the two epochs, for a total of four, bin-by-bin.

The combined results based on the physics-DT outputs, as obtained with CLfit2 algorithm, are presented in Fig. 9.2

- in terms of expected and observed excluded cross sections, relative to the standard model expectation, and

- in terms of log-likelihood ratios for the signal+background and background-only hypotheses, and as observed in the data.

The results of the individual channels are given in Figures 10.3-10.6. The numerical results are given in Tables 9.1 and 9.2
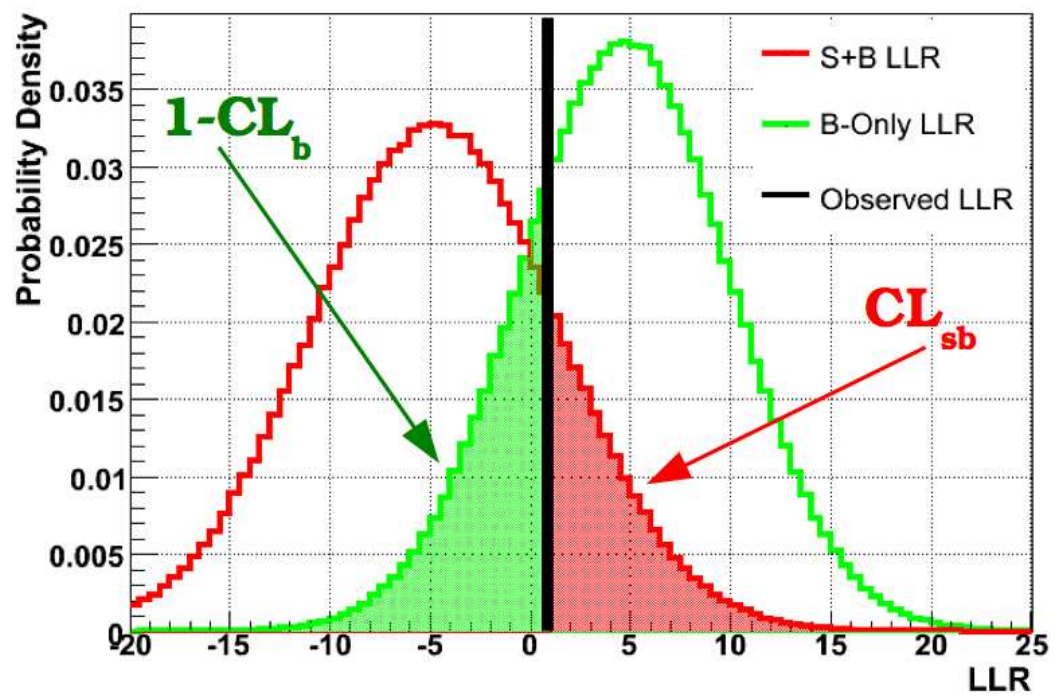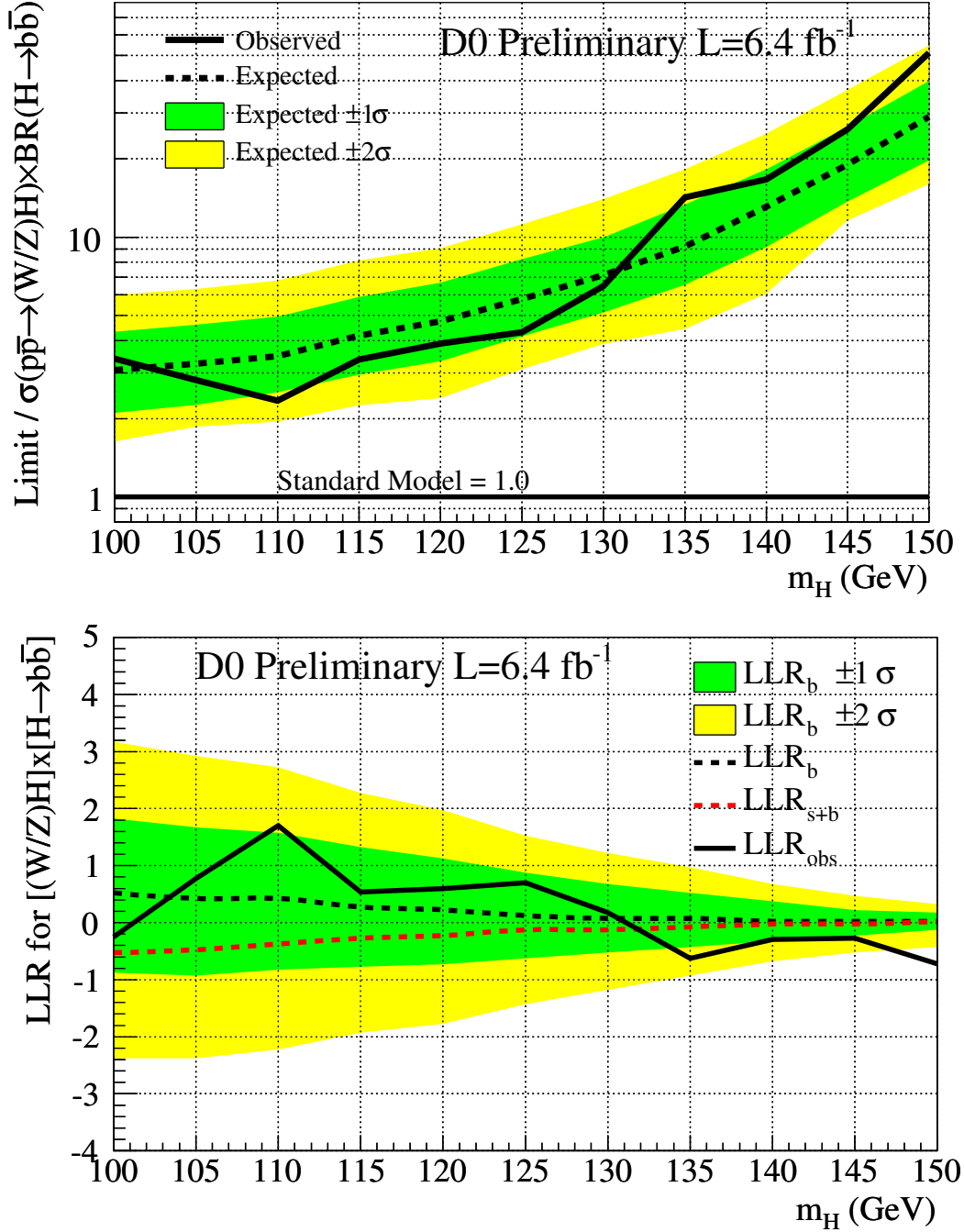
Figure 9.1: Cls as shown graphically

Figure 9.2: CLFit2 expected and observed 95% CL upper limits on the cross section ratios and log-likelihood ratios for the full Run II (a&b) single & double tag combination using boosted decision trees.
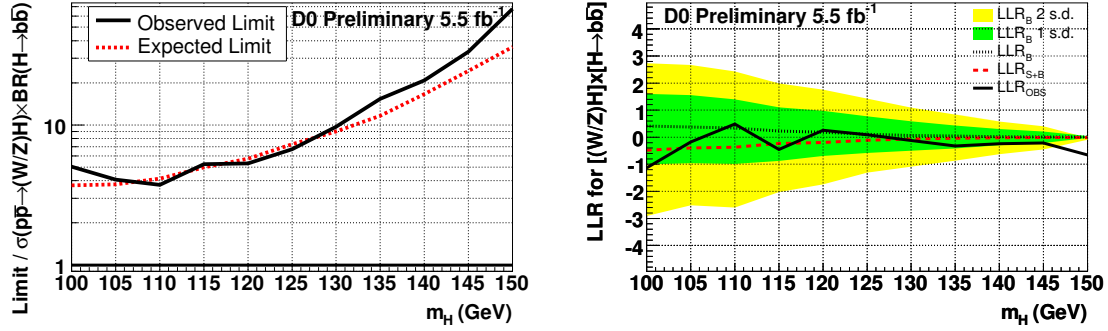
Figure 9.3: CLFit2 expected and observed 95% CL upper limits on the cross section ratios and log-likelihood ratios for the Run IIb $5.5\,\mathrm{fb}^{-1}$ double tag channel using boosted decision trees.
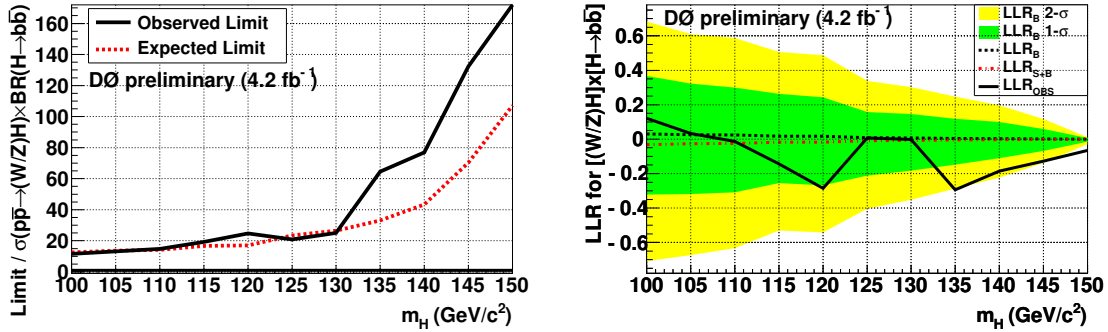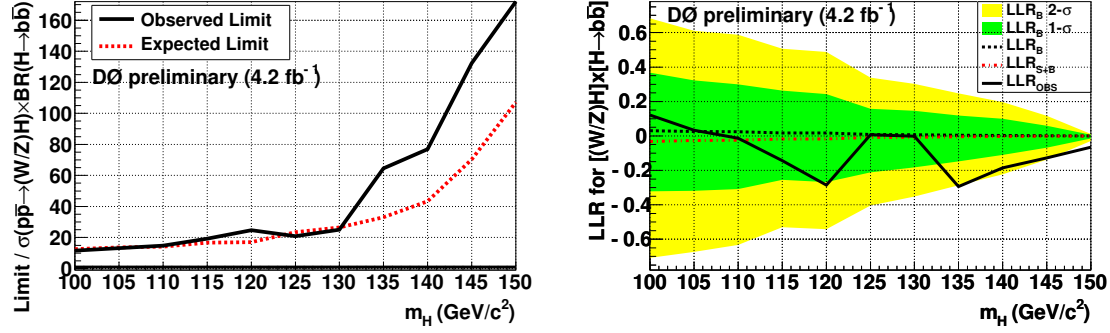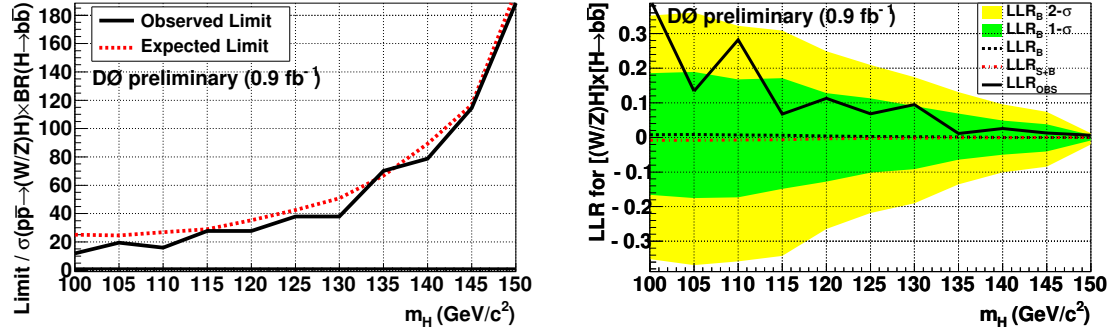

Figure 9.4: CLFit2 expected and observed 95% CL upper limits on the cross section ratios and log-likelihood ratios for the Run IIb $4.2\,\mathrm{fb}^{-1}$ publication single tag channel using boosted decision trees. *Selection taken from D0 note 5857.*

Figure 9.5: CLFit2 expected and observed 95% CL upper limits on the cross section ratios and log-likelihood ratios for the Run IIa $0.9\,\mathrm{fb}^{-1}$ publication double tag channel using boosted decision trees. *Selection taken from D0 note 5857.*

Figure 9.6: CLFit2 expected and observed 95% CL upper limits on the cross section ratios and log-likelihood ratios for the Run IIa $0.9\,\mathrm{fb}^{-1}$ publication single tag channel using boosted decision trees. *Selection taken from D0 note 5857.*

Final Limit From BDT

Tagging	Run2a		Run2b		Combined	
Point	Exp.	Obs.	Exp.	Obs.	Exp.	Obs.
100						
1 MT	26.930	12.506	12.354	12.045	11.346	8.108
1 L3 and 1 MT	9.108	6.954	3.703	5.034	3.461	4.176
Combined	8.047	4.319	3.548	4.767	3.208	3.349
105						
1 MT	25.861	18.517	13.485	13.523	12.004	10.544
1 L3 and 1 MT	10.138	5.967	3.763	4.080	3.515	3.118
Combined	8.901	4.820	3.673	4.022	3.363	2.815
110						
1 MT	27.792	15.724	14.730	13.777	12.877	9.600
1 L3 and 1 MT	10.940	6.198	4.140	3.740	3.756	2.826
Combined	9.578	4.103	3.963	3.532	3.641	2.340
115						
1 MT	29.890	26.869	18.001	20.494	15.562	16.435
1 L3 and 1 MT	11.913	4.824	4.976	5.255	4.475	3.591
Combined	10.360	4.615	4.871	5.403	4.266	3.475
120						
1 MT	36.329	26.854	18.043	28.486	16.165	22.478
1 L3 and 1 MT	13.493	7.274	5.736	5.316	5.141	3.767
Combined	11.924	5.766	5.443	6.004	4.850	3.981
125						
1 MT	42.891	31.368	24.217	26.244	20.731	20.142
1 L3 and 1 MT	15.535	9.052	7.295	6.710	6.380	5.058
Combined	13.842	6.821	6.931	6.916	5.962	4.170

Table 9.1: Ratio of the expected (observed) limit to the Standard Model prediction for different Higgs masses. Numbers are given for Run IIa and IIb, as well as for the combined result.

Final Limit from BDT

Tagging	Run2a		Run2b		Combined	
Point	Exp.	Obs.	Exp.	Obs.	Exp.	Obs.
130						
1 MT	51.536	36.048	27.595	29.106	24.242	21.668
1 L3 and 1 MT	18.510	14.903	8.978	9.719	7.835	7.717
Combined	16.822	10.339	8.608	9.465	7.436	6.797
135						
1 MT	70.134	70.289	33.402	69.338	30.063	59.079
1 L3 and 1 MT	25.056	22.567	11.651	15.388	10.246	12.540
Combined	22.686	17.012	10.924	19.231	9.673	14.355
140						
1 MT	91.013	70.317	43.362	87.109	38.443	68.438
1 L3 and 1 MT	34.680	26.048	16.600	20.824	14.748	15.853
Combined	31.364	17.213	15.214	25.459	13.754	16.966
145						
1 MT	122.682	117.879	68.382	133.918	59.643	105.759
1 L3 and 1 MT	49.152	39.305	24.353	33.300	20.464	25.024
Combined	43.242	26.606	23.123	38.660	19.513	26.247
150						
1 MT	201.030	188.472	101.860	192.225	90.380	156.577
1 L3 and 1 MT	76.488	55.488	36.020	67.611	30.315	48.632
Combined	67.855	41.744	34.018	72.402	29.316	49.460

Table 9.2: Ratio of the expected (observed) limit to the Standard Model prediction for different Higgs masses. Numbers are given for Run IIa and IIb, as well as for the combined result.

Chapter 10

CONCLUSIONS

A search for the Standard Model Higgs boson has been performed in $6.4\,\mathrm{fb}^{-1}$ of $p\bar{p}$ collisions at 1.96 TeV. The topology analyzed consists of a pair of acoplanar b jets with large $\not{E}_T$, as expected from $ZH \to \nu\bar{\nu}b\bar{b}$. The search is also sensitive to WH production, where the W decays leptonically and the charged lepton is undetected.

Boosted decision trees have been used to discriminate signal from background. Good agreement is observed between data and expected backgrounds, and, for a Higgs-boson mass of 115 GeV, a limit is set at 95% C.L. on the cross section multiplied by branching fraction of $(p\bar{p} \to (Z/W)H) \times (H \to b\bar{b})$ that observed larger than the value expected from the standard model.

Appendix A

RUN IIB SIGNAL SAMPLE PLOTS

Included here are the distributions of all variables used in the training of the BDTs. The double tag sample is described in the text. The single tag sample has gone through the same modeling verifications by the electroweak and control samples. However, only a data sample corresponding to 5.2 fb^{-1} is used. Also none of the calculated variables described in Section 6.4.6 are used in the training. The tree used do not make use of stochastic gradient boosting in the training, but instead use regular boosting.
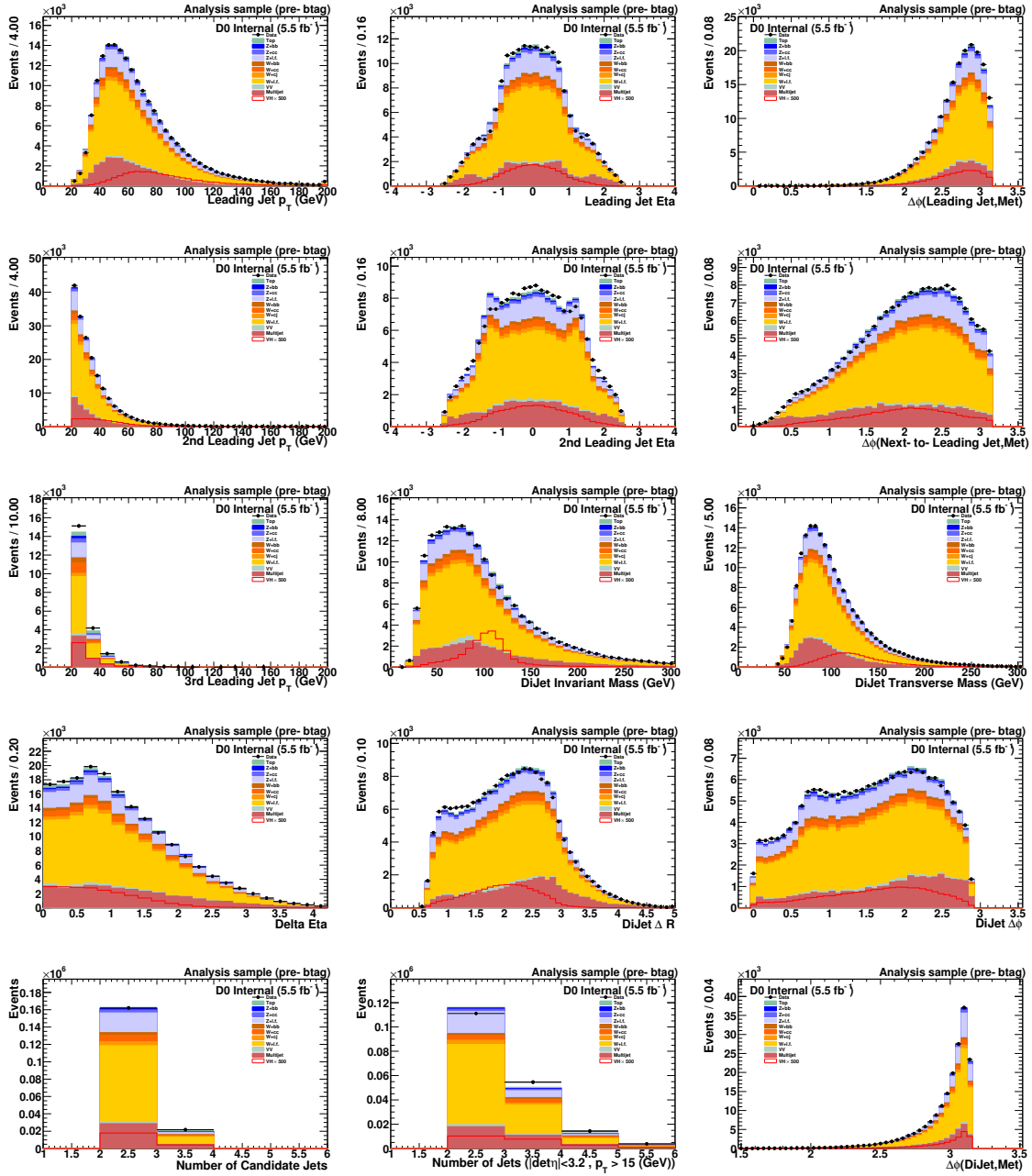
Figure A.1: Run IIb Signal sample before *b*-tagging
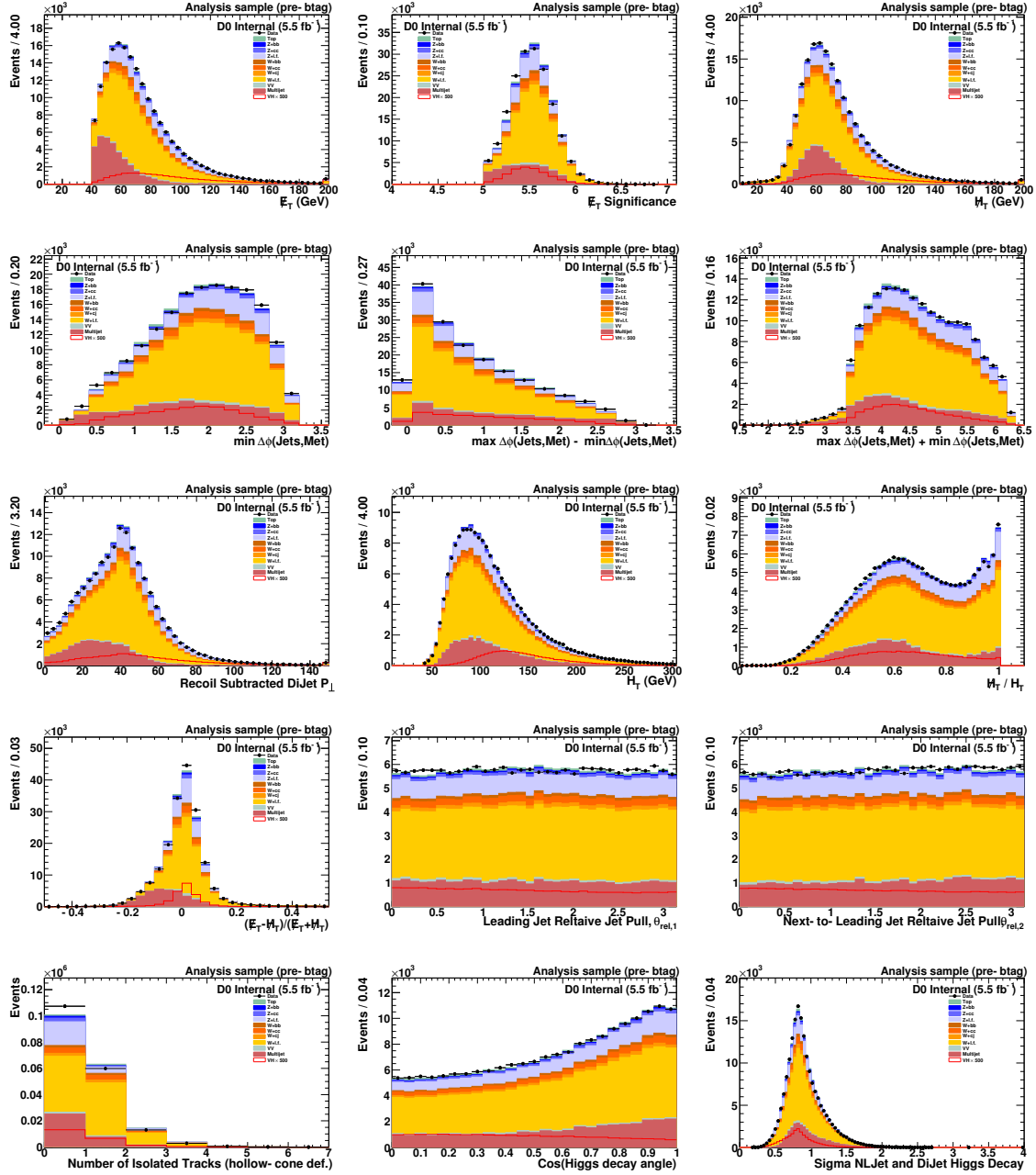
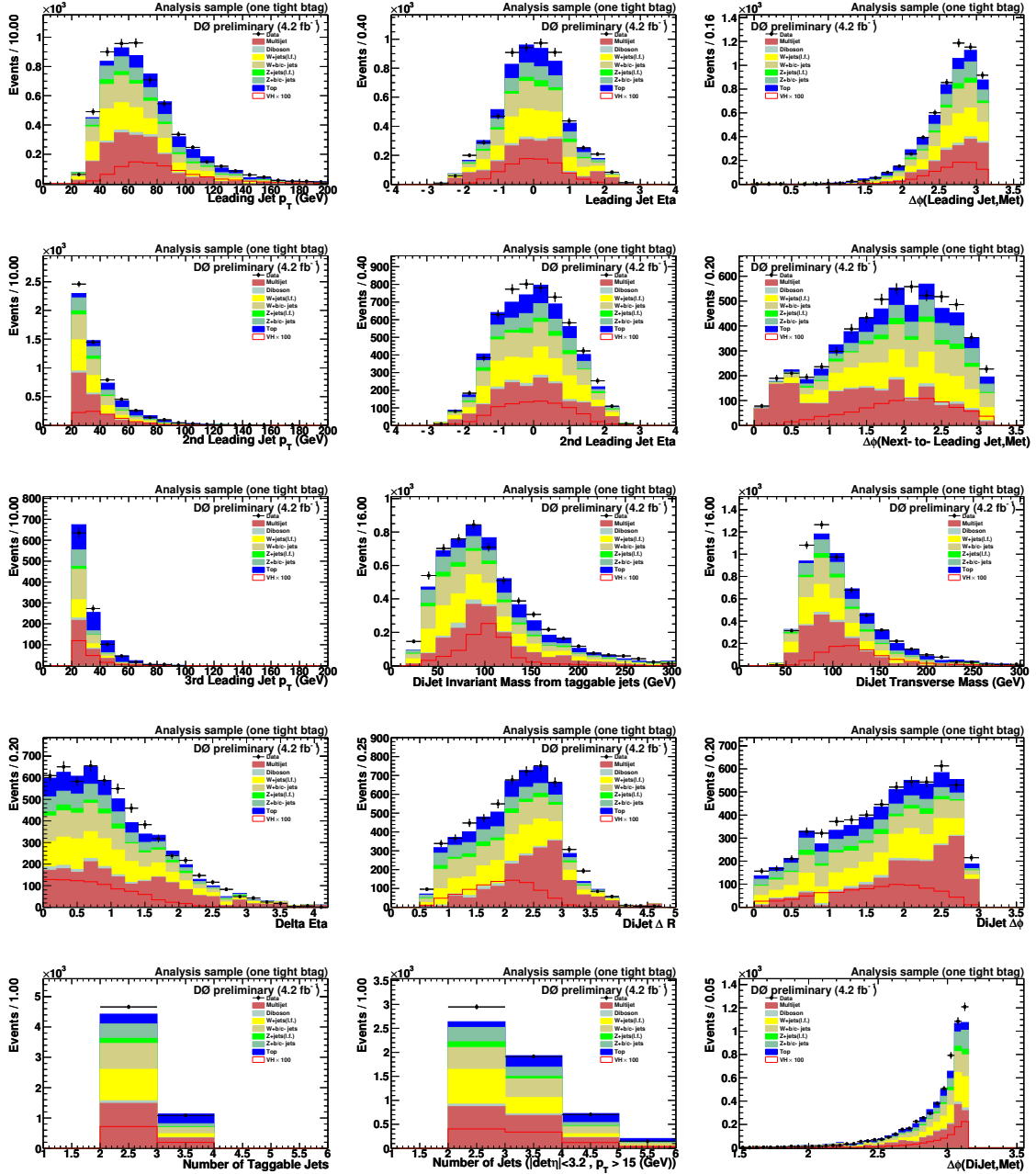Figure A.2: Run IIb Signal sample before *b*-tagging

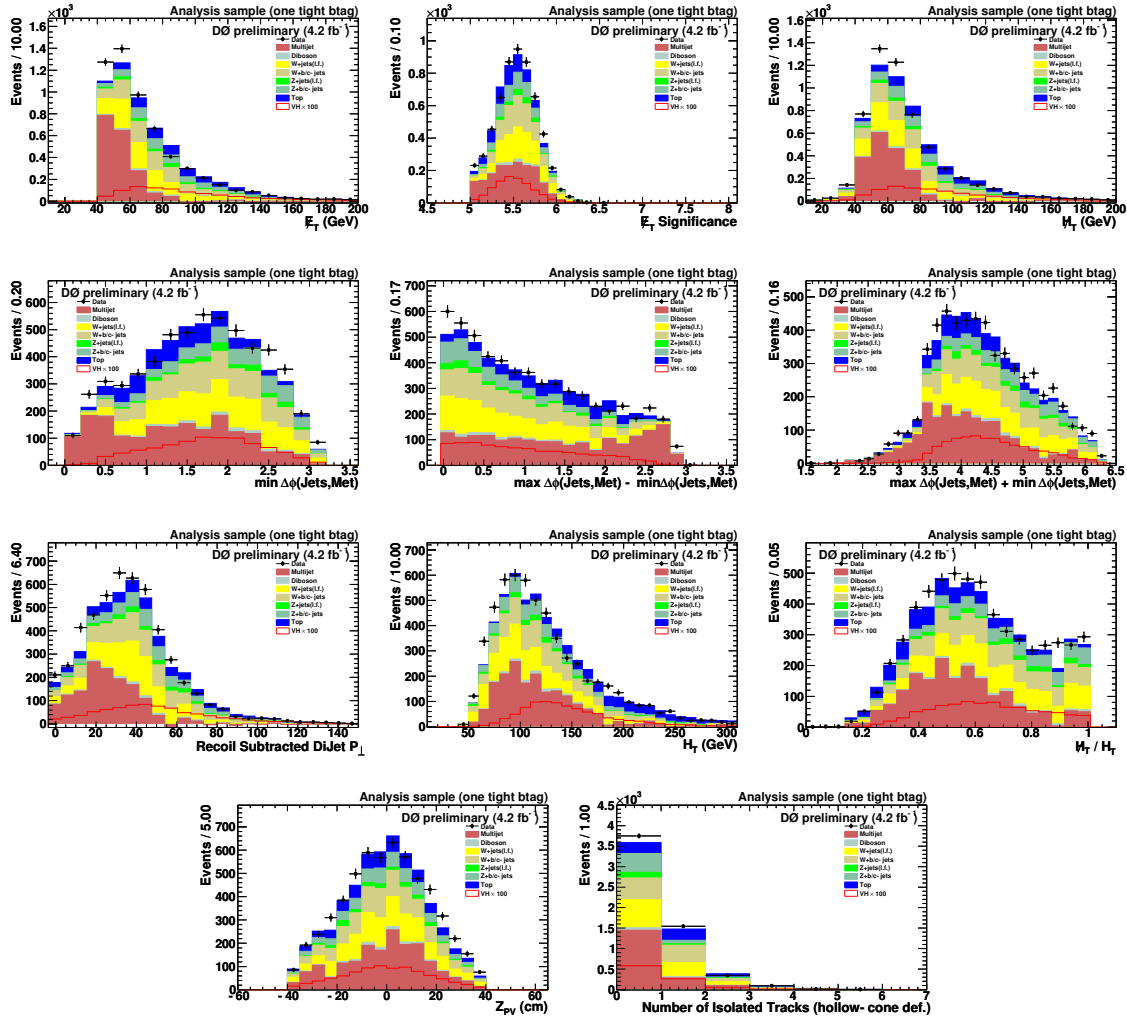Figure A.3: RunIIb Signal sample with one tight b-tag

Figure A.4: runIIb Signal sample with one tight b-tag

Figure A.5: Run IIb Signal sample with one tight and one loose b-tag

174

Figure A.6: RunIIb Signal sample with one tight and one loose b-tag

Appendix B

RUN IIA SIGNAL SAMPLE PLOTS

Included here are the distributions of all variables used in the training of the BDTs for RunIIa . The modeling is verified as described in the text with the control samples. In Run IIa the $\not{E}_T$ requirement in the first level of reconstruction (L1) is not present. This enhances the multijet contribution compared to Run IIb. In order to have the same final Decision Tree treatment in the two samples we apply two additional cuts:

- Uncorrected $\not{E}_T$ (without the CH part of the calorimeter) > 30 GeV

- $\not{E}_T(\text{GeV}) > -40 \times \min \Delta\phi(\not{E}_T, \text{jets}) + 80$ (MET triangle cut)

which were found to be closest to the trigger conditions. The effect of these two cuts is illustrated in Fig.B.1. The improvements due to these cuts were discussed in [54].

The Run IIa dataset corresponds to 0.9 fb^{-1}. Again, none of the calculated variables of Section 6.4.6 are used, and the decision trees are trained only using boosting.
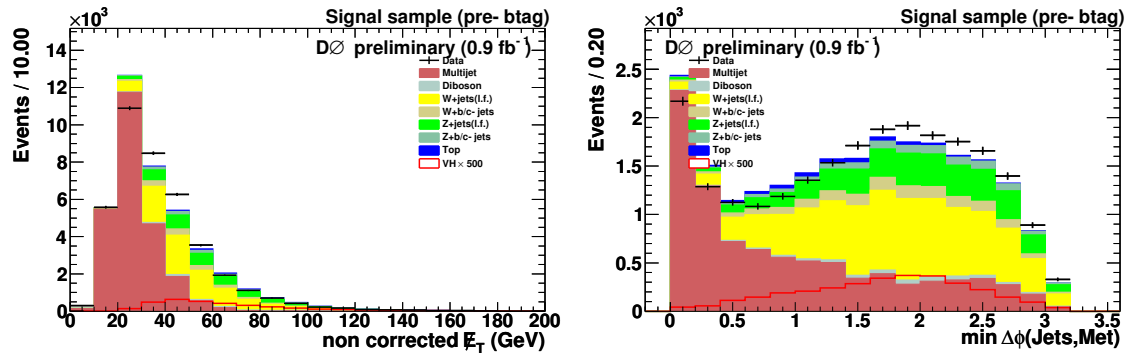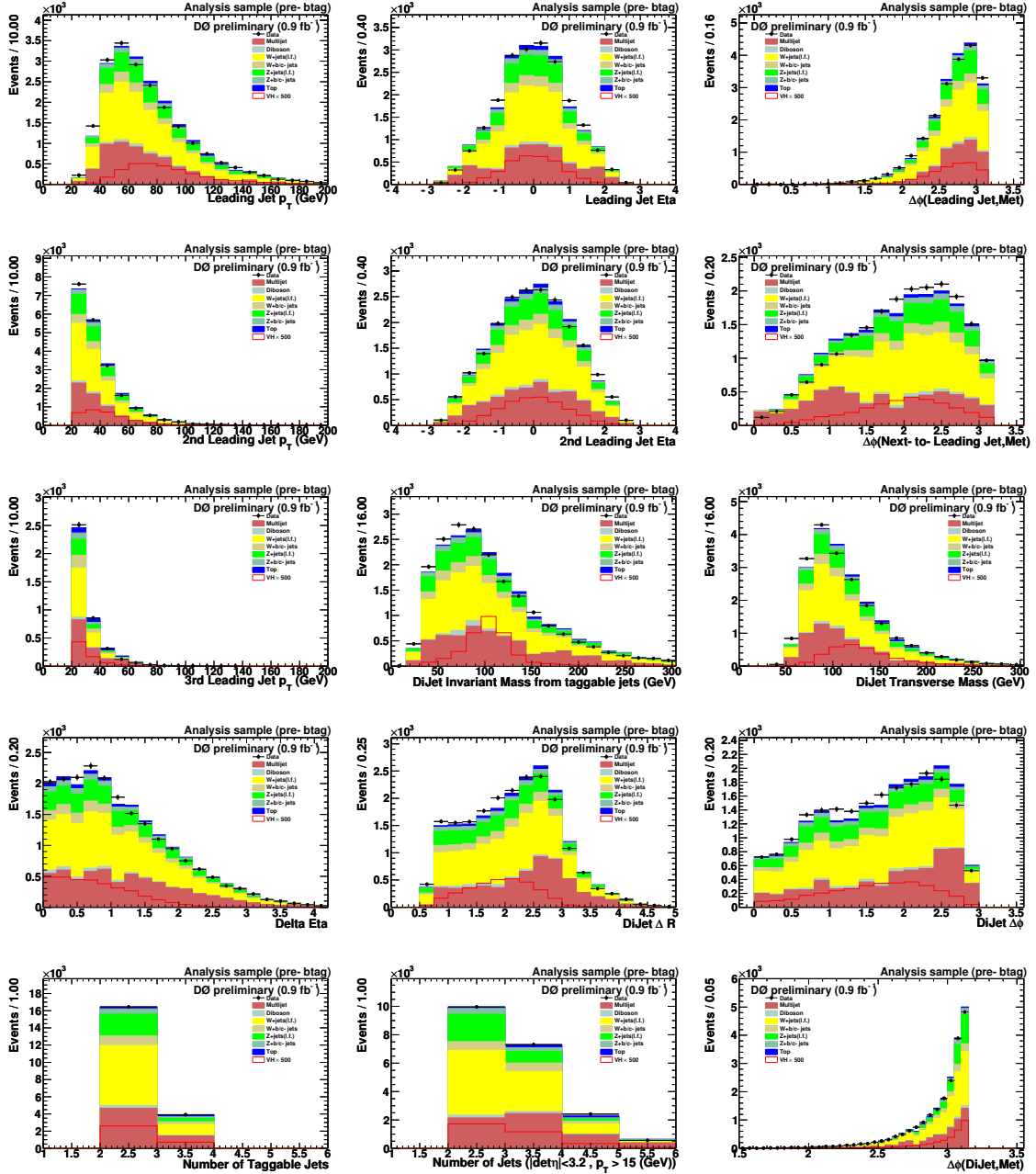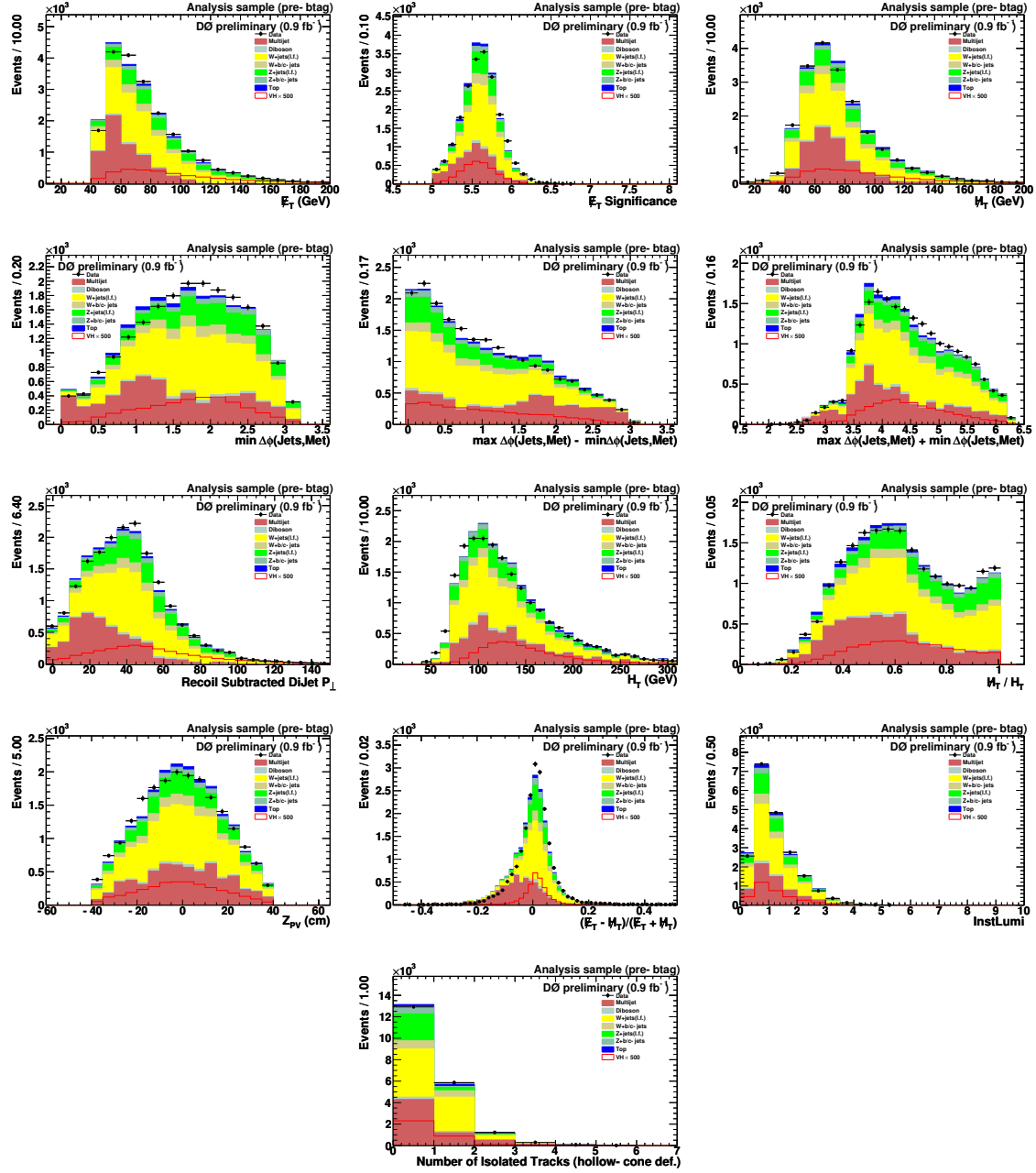
Figure B.1: The left plot is the uncorrected $\not{E}_T$ in Run IIa before the additional cuts were applied. The right plot is the $\min \Delta\phi(\not{E}_T, \text{jets})$ after the uncorrected $\not{E}_T$ cut was applied.

Figure B.2: RunIIa Signal sample before *b*-tagging

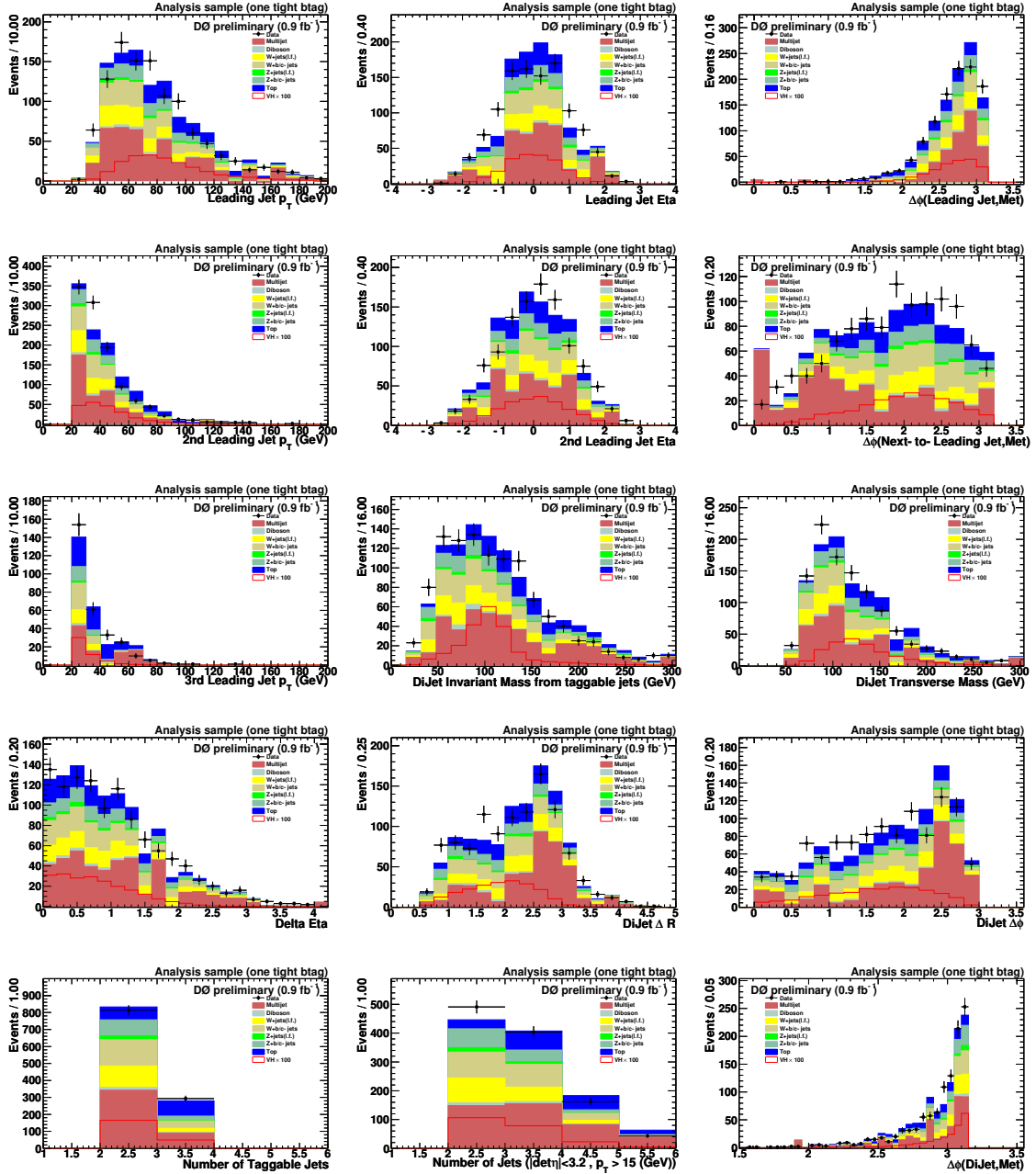Figure B.3: RunIIa Signal sample before *b*-tagging

Figure B.4: RunIIa Signal sample with one tight b-tag
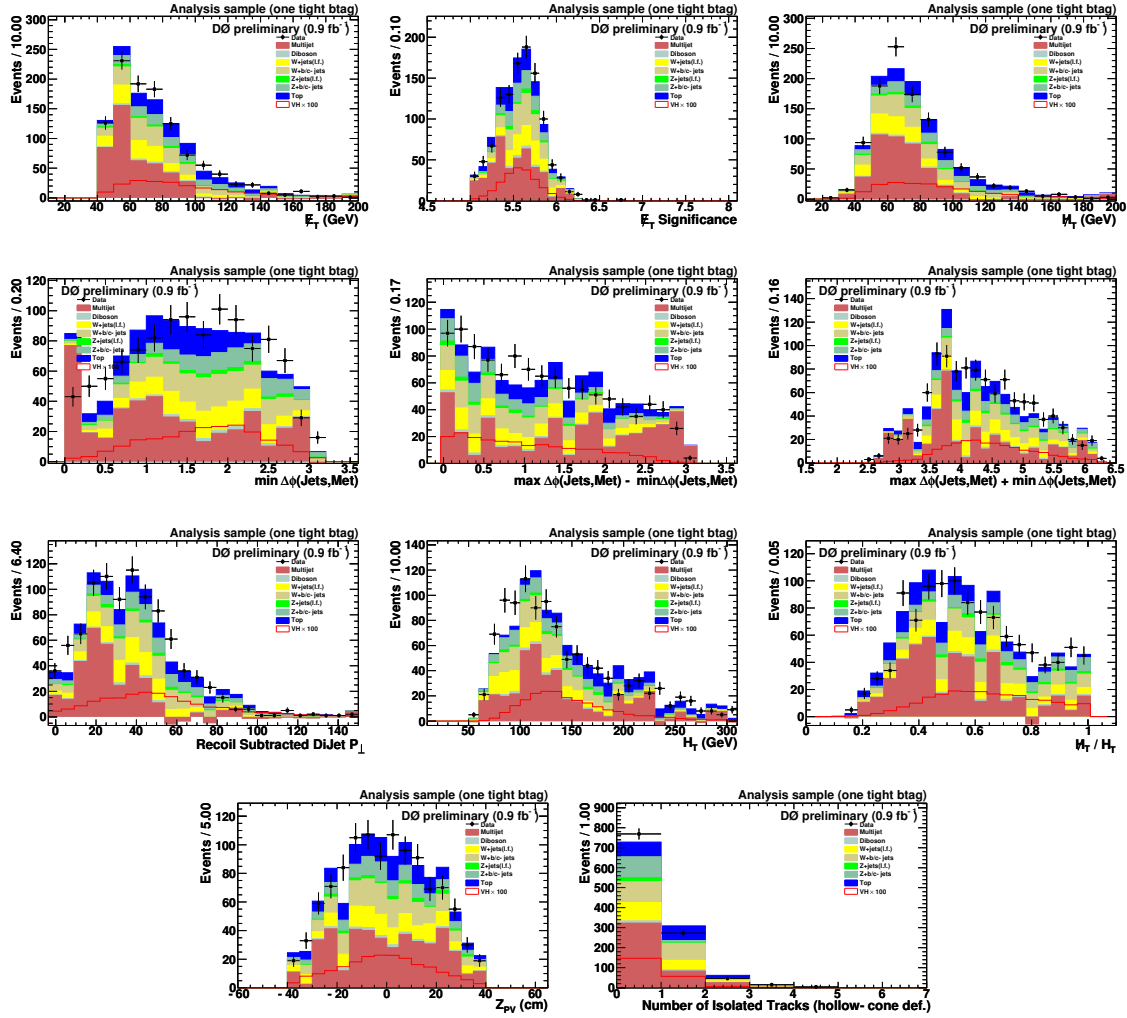
180

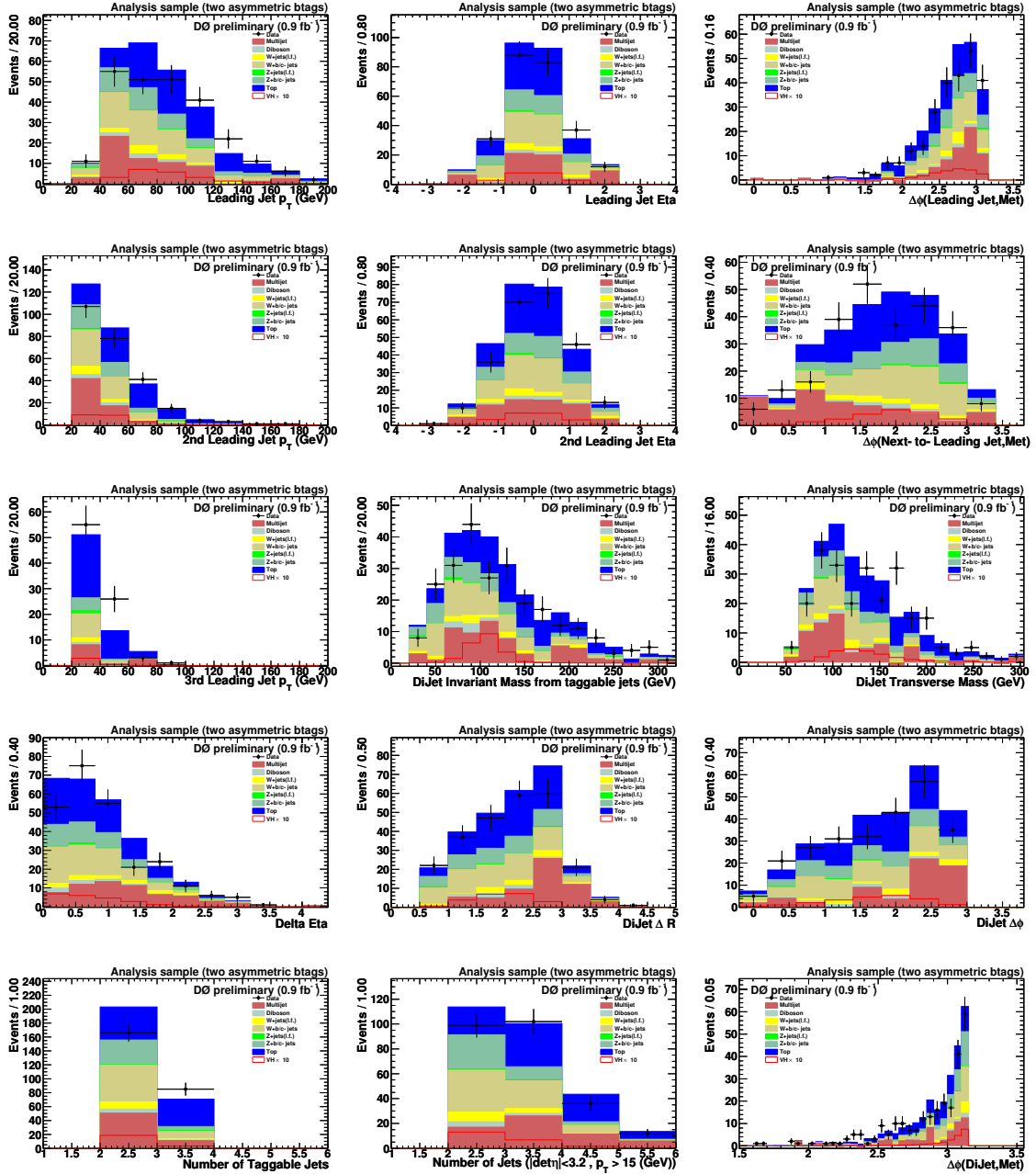Figure B.5: RunIIa Signal sample with one tight b-tag

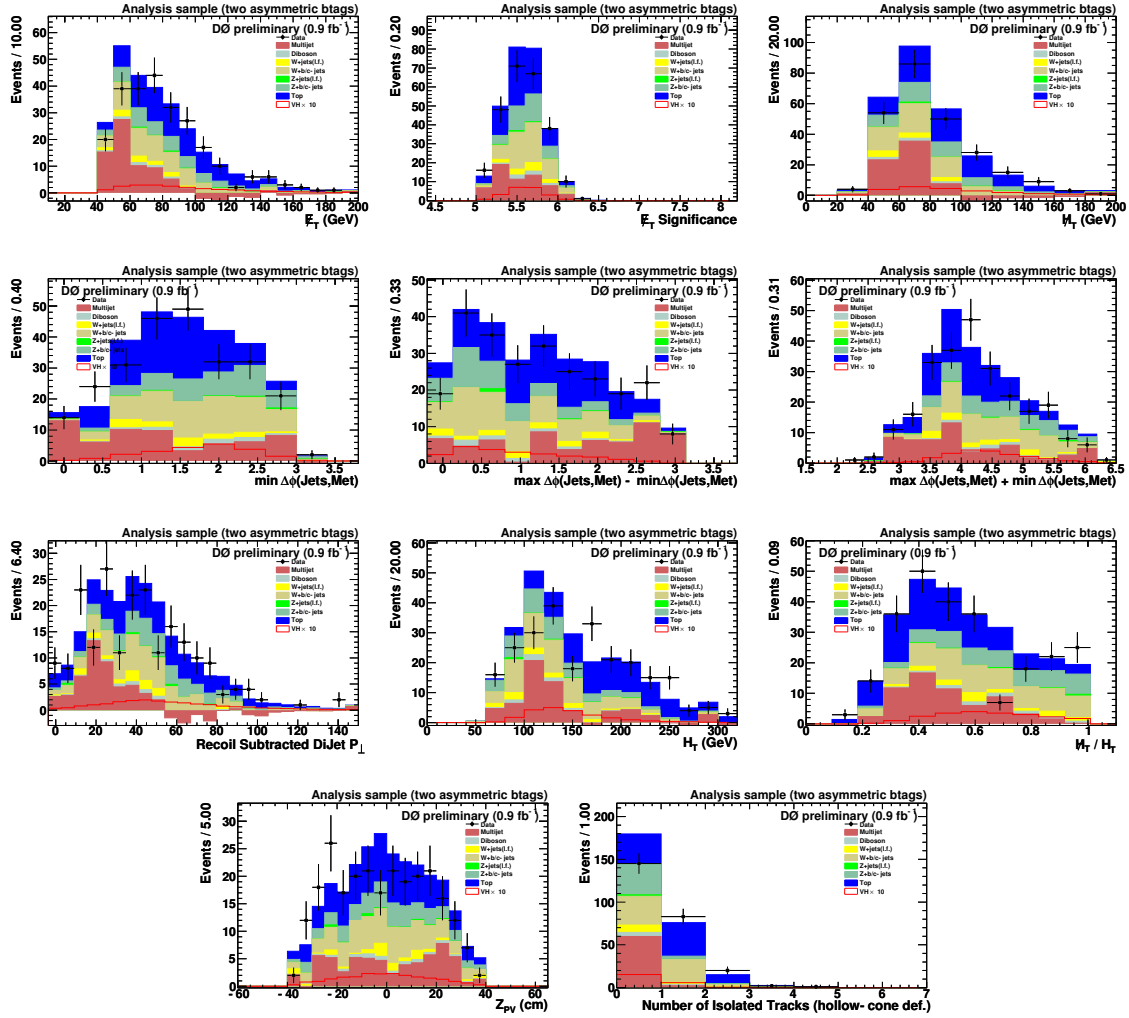Figure B.6: RunIIa Signal sample with one tight and one loose b-tag

182

Figure B.7: RunIIa Signal sample with one tight and one loose b-tag

Appendix C

JET SHAPE SYSTEMATICS

Systematic uncertainties related to jets[1] are estimated by shifting the correction factors by $\pm\ 1\sigma$ of their uncertainties and re-applying all preselection and selection cuts. In this process, statistical fluctuations are expected in the low statistics samples, e.g., the tagged samples. To mitigate this effect, we estimate the jet shape systematics from a high statistics sample, which we chose to be the 0-tag sample.

In order to prove the validity of this approach, we compared the shape distortions caused by jet systematics in Physics-DT outputs in the 0-tag and in the (1 or 2)-tag samples. In practice, we used plots of ratios of Physics-DT outputs between 0-tag and (1 or 2)-tag, both for the nominal correction and for the shifted correction. An example is given in Fig. C.1.

Since we had to do this for all jet systematics, all MC samples and all Physics-DT outputs for each mass point, we performed a KS test for each ratio-histogram pair, and we considered the distribution of KS probabilities shown in Fig. C.2. From this we concluded that all shape distortions are similar for 0-tag and for (1 or 2)-tag. For completeness, we looked in detail at the ratio plots for which a KS probability smaller than 0.2 was found, and concluded that only statistical fluctuations are responsible for the tail of the KS probability distribution.

---

[1]Energy scale, resolution, reconstruction and identification, vertex confirmation, taggability
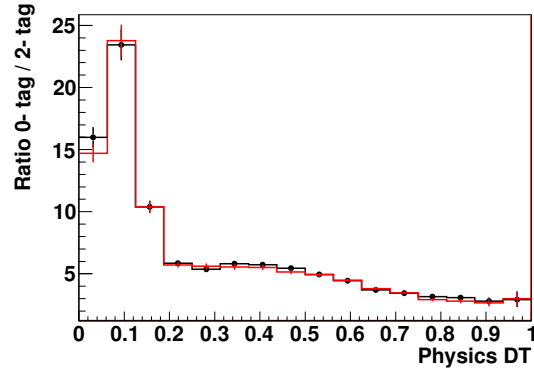
Figure C.1: r

atioRatio between 0-tag and 2-tag Physics DT in the p20 top MC sample for the nominal
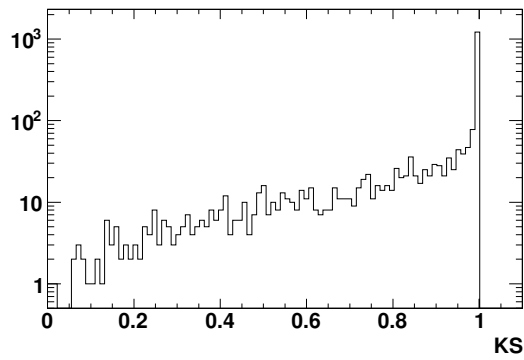JES correction (black points) and for the $+1\sigma$ shifted JES correction (red histogram).

Figure C.2: KS probability distribution for all jet systematics, all MC samples and all Physics DT
outputs.

Appendix D

ALPGEN ANGULAR REWEIGHTINGS

D0 currently has a set of data-driven corrections derived to reconcile the differences, observed in many analyses, between the kinematic distributions produced by ALPGEN and those in data [38]. Using the same technique we derive a similar correction in the $\Delta\eta$ distribution in the multijet free electroweak control sample. We calculate the $V + jets$ contribution in data by subtracting the top and diboson contributions from data. We then take the ratio of this data estimate to the $V + jets$ MC. The reweighting function is a third degree polynomial fit to this ratio and is applied to all signal and control sample $V + jets$ MC. Below are some distributions before and after reweighting.
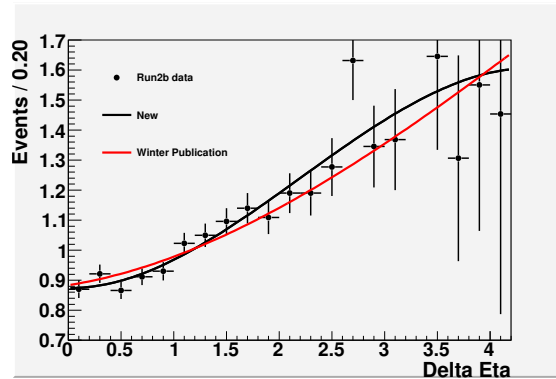

Figure D.1: Third degree polynomial fit to the ratio of $data - top_{MC} - diboson_{MC}$ to $V + jets_{MC}$. The red line represents the full RunII fit used in the Winter publication. The black line represents the RunIIb fit used in this note.

Figure D.2: $\Delta\eta$(left column row), ΔR(middle column), and dijet invariant mass (right column) distributions in the pretag electroweak control sample before (top row) and after (bottom) the reweighting function is applied on the full RunII dataset

Figure D.3: $\Delta\eta$(left column), ΔR(middle column), and dijet invariant mass (right column) distributions in the pretag signal sample after the multijet decision tree cut and before (top row) and after (bottom row) the reweighting function is applied on the full RunII dataset

BIBLIOGRAPHY

[1] The ALEPH, DELPHI, L3, OPAL, SLD Collaborations. *Precision Electroweak Measurements on the Z Resonance.* Phys. Rept. 427 (2006) 257-454

[2] R. Feynman, R. Leighton, M. Sands. *The Feynman Lectures on Physics* Vol. II. Addison-Wesley. Reading. 1977.

[3] D. Griffiths. *Introduction to Elementary Particles.* Second, Revised Edition. Weinheim: Wiley-VCH, 2010.

[4] P.Langacker. *The Standard Model and Beyond.* Boca Raton: Taylor & Francis, 2010.

[5] G. Kane. *Modern Elementary Particle Physics: The Fundamental Particles and Forces?* Cambridge: Perseus, 1993.

[6] D. Perkins. *Introduction to High Energy Physics.* Fourth Ediition. Cambridge University Press. Cambridge. 2000.

[7] S. Dawson. *Introduction to Electroweak Symmetry Breaking*, `arXiv:hep-ph/9901280v1`

[8] A. Djouadi, J. Kalinowski and M. Spira, Comput. Phys. Commun. **108**, 56 (1998) [arXiv:hep-ph/9704448].

[9] K. Nakamura *et al* (Particle Data Group), J. Phys. G **37**, 075021 (2010)

[10] C. Jessop. Class Lecture. Physics 617: *Introduction to Particle Physics.* University of Notre Dame. Spring 2006.

[11] B.Worthel, *Linac Rookie Book.* http://www-bdnew.fnal.gov/operations/rookie_books/LINAC_v2.pdf (2006).

[12] The DØ Collaboration. *The Upgraded DØ Detector.* Instrum. Methods in Phys. Sect A **565**, 463 (2006)

[13] S.N. Ahmed *et al. The DØ Silicon Microstrip Tracker.* Accepted for publication in Nucl. Instrum. Methods in Phys. Res. Sect. A. ArXiv.org:1005.0801

[14] C. Barnes, P. Jonnson, R. Beuselinck. *Vertexing for the L-3 Trigger* DØ note 4271

[15] M. Narain, F. Stichelbaut. *Vertex Reconstruction Using the Impact Parameters Technique* DØ note 3560

[16] http://www-d0.fnal.gov/phys_id/emid/d0_private/variables.html

[17] C. Blazey *etal. Run II Jet Physics.* arXive:hep-ex/0005012v2

[18] V. Abazoc *et al*, The DØ Collaboration. *b−Jet Identification in the DØ Experiment.* Nucl. Instrum. Methods in Phys. Res. Sect. A **620**, 490 (2010)

[19] K. DeVauhan, G. Golovanov, U. Heintz, S. Jabeen, A. Kupco, M. Padilla, V. Parihar, A. Tanasijczuk, *"Jet Energy Scale Determination for DØ Run IIb (final p20 version)"*, DØ Note 5801.

[20] D. Gilberg, D. O'Neil, Y. Coadou, H. Choi, B. Pass, M. Vetterli. *Measuring Jet Response Using the Missing E_T projection Fraction Method in $\gamma + jet$ events.* DØ Note 4571

[21] A. Goussiou, A. Juste, P. Mal. *DØ Jet Reconstruction Using Track+Calorimeter Information.* DØ Note 5306

[22] M. Voutilanen. *Jet p_T resolution for Run IIa final JES with dijet J4s jet corrections.* DØ note 5499

[23] J. BackusMayes. *Search for Associated Production of Z and Higgs Bosons in Proton-antiproton Collisions at 1.96 TeV* FERMILAB-THESIS-2010-52, Dec 2010.

[24] N. Huske. *The Higgs Boson in the Standard Model, Theoretical Constraints and a Direct Search in WH Channel at the Tevatron.* FERMILAB-THESIS-2010-38, Sep 2010.

[25] M. Sanders. http://www-d0.fnal.gov/m̃sanders/Higgs/CSTimesBr.html

[26] M. Carena *et al.*, *"Report of the Tevatron Higgs Working Group"*, `arXiv:hep-ph/0010338`; CDF and DØ Collaborations, *"Results of the Tevatron Higgs Sensitivity Study"*, FERMILAB-PUB-03/320-E (2003).

[27] V.M. Abazov *et al.* (DØ Collaboration), Phys. Rev. Lett. **104**, 071801 (2010).

[28] S. Calvet *et al.* "Search for the Standard Model Higgs boson in the $ZH \rightarrow \nu\nu b\bar{b}$ Channel in 5.2/fb", D0 Note 5857.

[29] S.Abachi *et al.* (DØ Collaboration). *Observation of the Top Quark* Phys. Rev. Lett. **74**, 2632 (1995).

[30] T. Sjöstrand, S. Mrenna and P. Skands, JHEP **0605**, 026 (2006); version 6.413 was used.

[31] J. Pumplin *et al.*, JHEP **0207**, 012 (2002); D. Stump *et al.*, JHEP **0310**, 046 (2003).

[32] M.L. Mangano *et al.*, JHEP **0307**, 001 (2003); version 2.11 was used.

[33] S. Höche *et al.*, *"Matching Parton Showers and Matrix Elements"*, in Proceedings of the Workshop on the Implications of HERA for LHC Physics, ed. A. De Roeck and H. Jung (CERN, Geneva, 2005), p288.

[34] E. Boos *et al.* (CompHEP Collaboration), Nucl. Instrum. Methods in Phys. Res. A **534**, 250 (2004).

[35] U. Langenfeld, S. Moch and P. Uwer, Phys. Rev. D **80**, 054009 (2009) N. Kidonakis, Phys. Rev. D **74**, 114012 (2006).

[36] T. Bolton M. Shamim, *"Generator Level Reweighting of Z boson p_T"*, DØ Note 5565.

[37] G. Hesketh, *"Generator Level Re-weighting of the Inclusive W p_T Distribution"*, DØ Note 5786.

[38] W. Fisher, J. Haley, D. Price, *"Studies of Alpgen parameters, corrections and associated uncertainties"*, DØ Note 5966.

[39] T. Guillemin, presentation at 2010 collaboration meeting, May 12, 2010
`http://www-d0.hef.kun.nl//askArchive.php?base=agenda&categ=a10849&id=a10849s1t13`
`/transparencies`

[40] C. Ochando, presentation in JES meeting, May 15, 2008
`http://www-d0.hef.kun.nl//askArchive.php?base=agenda&categ=a08924&id=a08924s1t3`
`/transparencies/ochando_jes_15may08_updated.pdf`

[41] A. Schwartzman, "Missing Et Significance Algorithm in RunII data", DØ Note 4254 (2003)

[42] S. Calvet, presentation in Vjets meeting, June 9, 2009
`http://www-d0.hef.kun.nl//askArchive.php?base=agenda&categ=a09897&id=a09897s1t9`
`/transparencies`

[43] V. M. Abazov *et al.* [DØ Collaboration], *Measurement of color flow in $t\bar{t}$ events from $p\bar{p}$ collisons at $\sqrt{s} = 1.96$ TeV*

[44] V. M. Abazov *et al.*, *"Observation of ZZ production in $p\bar{p}$ collisions at $\sqrt{s} = 1.96$ TeV"*, Phys. Rev. Lett. **101**, 171803 (2008)

[45] P. Verdier, Y. Tschudi, *"Search for T-odd quarks in Little Higgs models with T-parity and first generation scalar leptoquarks in events with two acoplanar jets and missing transverse energy"*, DØ note 5780 (2008)

[46] L. Breiman *et al.*, *"Classification and Regression Trees,"* Wadsworth (1984).

[47] Y. Freund, R. Schapire. A decision-theoretic generalization of on-line learning and an application to boosting. *Journal of Computer and System Sciences*, 55(1): 119-139, August 1997.

[48] T. Andeen *et. al.*, FERMILAB-TM-2365-E (2006)

[49] The CDF and DØ Collaborations. *Combined CDF and DØ Upper Limits on Standard-Model Higgs Production* arXiv:1007.4587[hep-ex].

[50] S. Muanza, Presentation in V+jets meeting, February 5, 2008
http://www-d0.hef.kun.nl//askArchive.php?base=agenda&categ=a0897&id=a0897s1t3/
transparencies/muanza_22jan08_v2.pdf

[51] J. Haley, presentation in V+jets workshop, September 28, 2009
http://www-d0.hef.kun.nl//askArchive.php?base=agenda&categ=a091522&id=a091522s6t3/
transparencies/HiggsSystematics_20090928_v3.pdf

[52] W. Fisher. *Collie: A Confidence Level Limit Evaluator*. Version 4.00. DØ Note 5595.

[53] J. Taylor. *An Introduction to Error Analysis*. Second Edition. University Science Books. Sansulito. 1997.

[54] K. Peters *et al.*, presentation in Higgs meeting, July 9th, 2009
http://www-d0.hef.kun.nl//askArchive.php?base=agenda&categ=a091096&id=a091096s1t4
/transparencies